ATLAS CONF Note

ATLAS-CONF-2021-044

31st July 2021

Journal: JHEP

Measurements of Higgs boson production cross-sections in the $H \to \tau^+\tau^-$ decay channel in pp collisions at $\sqrt{s} = 13$ TeV with the ATLAS detector

The ATLAS Collaboration

Measurements of the production cross-sections of the Standard Model (SM) Higgs boson (H) decaying into a pair of τ leptons are presented. The measurements use data collected with the ATLAS detector from pp collisions produced at the Large Hadron Collider at a centre-of-mass energy of $\sqrt{s} = 13$ TeV, corresponding to an integrated luminosity of 139 fb^{-1}. Leptonic ($\tau \to \ell\nu_\ell\,\nu_\tau$) and hadronic ($\tau \to$ hadrons ν_τ) decays of the τ lepton are considered. All measurements account for the branching ratio of $H \to \tau\tau$ and are performed with a requirement $|y_H| < 2.5$, where y_H is the true Higgs boson rapidity. The production cross-section of the $pp \to H \to \tau\tau$ process is measured to be 2.90 ± 0.21 (stat) $^{+0.37}_{-0.32}$(syst) pb. Inclusive cross-sections are determined separately for the four dominant production modes: 2.7 ± 0.4 (stat) $^{+0.9}_{-0.6}$(syst) pb for the gluon-gluon fusion, $0.196\ ^{+0.028}_{-0.027}$(stat) $^{+0.032}_{-0.025}$(syst) pb for the vector-boson fusion, 0.11 ± 0.06 (stat) ± 0.04 (syst) pb for the vector boson associated production, and $0.048\ ^{+0.033}_{-0.029}$(stat) $^{+0.036}_{-0.029}$(syst) pb for the top-quark pair associated production. Measurements in exclusive regions of the phase space, using the simplified template cross-section framework, are also performed. All results are in agreement with the SM predictions.

1 Introduction

A particle consistent with the Standard Model (SM) Higgs boson [1–6] was discovered in 2012 by the ATLAS and CMS Collaborations [7, 8] from the analysis of proton–proton (pp) collisions produced by the Large Hadron Collider (LHC) [9]. Since then, the analysis of data collected at centre-of-mass energies of 7 TeV, 8 TeV and 13 TeV in Runs[1] 1 and 2 of the LHC has led to the precise measurement of the Higgs boson mass, $m_H = 125.09$ GeV [10], and to the observation and measurement of the four main production modes (gluon-gluon fusion, vector-boson fusion, associated production with a weak gauge boson or with a pair of top quarks) and several decay channels of the Higgs boson predicted by the SM [11–25].

The decay into a $\tau^+\tau^-$ pair[2] has the largest branching fraction of all leptonic Higgs boson decays (6.3% [26, 27] for a mass of $m_H = 125.09$ GeV). Consequently, the large number of Higgs boson decays to $\tau\tau$ produced at the LHC ($\approx 400 \cdot 10^3$) offers a unique opportunity to study the Yukawa mechanism in detail. Measurements in this final state are however complicated at the experimental level, as the presence of two to four neutrinos[3] in the final state significantly degrades the resolution of the measured Higgs boson four momentum, rendering the separation between the signal and the large background from $Z \to \tau\tau$ events difficult. This effect can be mitigated through the dedicated study of the Higgs production modes where the event topology differs drastically from that of Z + jets events, the two most sensitive being the production of the Higgs boson through vector-boson fusion (VBF) as well as the production through gluon-gluon fusion (ggF) with a large momentum transfer.

The first evidence of the $\tau\tau$ decay of the Higgs boson was obtained by the ATLAS [28] and CMS [29] collaborations using data collected at centre-of-mass energies of 7 TeV and 8 TeV during Run 1 of the LHC. The combination [21] of these two results led to the first observation of the $\tau\tau$ decay of the Higgs boson. More recent works are documented in Refs. [30–32].

This paper presents measurements of the SM Higgs boson decaying into a di-τ pair with the ATLAS detector, using the full Run 2 LHC dataset. The $pp \to H \to \tau\tau$ process is measured inclusively, in the four dominant production modes simultaneously, and as a function of key properties of the event. This is achieved with an optimised categorisation of the collected events. Three di-τ final states are targeted: two hadronically-decaying τ leptons (τ_{had}) denoted $\tau_{\text{had}}\tau_{\text{had}}$, one leptonically decaying τ lepton (τ_{lep}) and one τ_{had} denoted $\tau_{\text{lep}}\tau_{\text{had}}$[4], and two τ_{lep} with different flavours denoted $\tau_e\tau_\mu$. The remaining final states, with two same-flavour light leptons ($\tau_e\ \tau_e$ and $\tau_\mu\ \tau_\mu$), are not considered due to large uncertainties in $Z \to ee$ and $Z \to \mu\mu$ contributions to the background expectation. The dominant background processes after the event selection are $Z \to \tau\tau$, $t\bar{t}$ and processes with at least one jet mis-reconstructed as a τ_{had}. Templates of the estimated invariant mass of the $\tau\tau$ pairs are built for each process in the signal regions (SR) defined by the event selection and categorisation. The templates are used as input to a binned maximum-likelihood fit which allows the yields and kinematics of both the signal and the background processes to be measured. Control regions (CR) enter the fit as event counts and help determine the normalisation of the main background sources as well as constrain their uncertainties.

This work uses 139 fb^{-1} of pp collision data collected at a centre-of-mass energy of 13 TeV, to be compared with 36 fb^{-1} for the previous $H \to \tau\tau$ cross-section measurements [22]. It introduces a new reconstructed event categorisation designed for the improved *stage 1.2* binning [33] of the simplified template cross-section

[1] Run 1 signifies the LHC data-taking period in the years 2010–2012 and Run 2 the one in 2015–2018.

[2] denoted $\tau\tau$ or di-τ for simplicity throughout the paper

[3] depending on the decay mode of the τ leptons

[4] The $\tau_{\text{lep}}\tau_{\text{had}}$ categories can be split into $\tau_e\tau_{\text{had}}$ and $\tau_\mu\tau_{\text{had}}$ where distinguishing the light lepton flavour is appropriate.

(STXS) framework [27]. The treatment of ggF events with large momentum is refined with three times more categories. Selected events are categorised with requirements on the transverse momentum of the reconstructed Higgs boson candidate ($p_{\mathrm{T}}(H)$) and on the potential additional hadronic jets. Two new categories targeting production modes where the Higgs boson is created in association with other objects are added based on requirements on the kinematics and tagged flavour of the jets in the event. The first targets the production of a Higgs boson in association with a pair of top quarks ($t\bar{t}H$), where both top quarks and both τ leptons decay hadronically, complementing the explorations in Ref. [34], and will be denoted as $\mathrm{tt}(0\ell)H \to \tau_{\mathrm{had}}\tau_{\mathrm{had}}$ throughout the rest of this paper[5]. The second targets the production of a Higgs boson in association with a vector boson V (W, Z). This new category, referred to as V(had)H, focuses on events with a hadronic decay of the V boson while the production of $Z(\to \ell\ell)H$ and $W(\to \ell\nu)H$ events is studied separately [35]. Finally, the selection of VBF events was also improved by multivariate techniques.

In addition to the new extended categorisation, several improvements to the analysis methodology have been implemented: the object selection has been improved, multivariate discriminants have been optimised to enhance the purity of the SRs in the targeted Higgs boson production modes have been introduced, the number of simulated background events has been significantly increased and the usage of the $Z \to \ell\ell$ control region has been refined. The latter relies on a new simplified implementation of the embedding technique [36, 37] which replaces the momenta of reconstructed electrons and muons from $Z \to \ell\ell$ data events by equivalent momenta of simulated τ lepton decay products.

This document is organised as follows. Section 2 describes the ATLAS detector. This is followed in Section 3 by a description of the dataset and Monte Carlo (MC) simulated samples employed by the measurement. Section 4.1 details the reconstruction of the physics objects. The event selection and categorisation is described in Section 4.2. In Section 5, the estimation of the background processes is discussed with an emphasis on the simplified embedding technique to model $Z \to \tau\tau$ processes in Section 5.1 and the data-driven estimates of the processes with at least one jet faking electrons, muons and τ_{had} in Section 5.2. Section 6 presents the systematic uncertainties affecting the measurement and their estimation. The details of the signal extraction fit are discussed in Section 7 and Section 8 presents the results of the measurement. Section 9 summarizes the conclusions of this work.

2 The ATLAS detector

The ATLAS detector [38] at the LHC covers nearly the entire solid angle around the collision point.[6] It consists of an inner tracking detector surrounded by a thin superconducting solenoid, electromagnetic and hadron calorimeters, and a muon spectrometer incorporating three large superconducting air-core toroidal magnets.

The inner-detector system (ID) is immersed in a 2 T axial magnetic field and provides charged-particle tracking in the range $|\eta| < 2.5$. The high-granularity silicon pixel detector covers the vertex region and typically provides four measurements per track, the first hit normally being in the insertable B-layer (IBL) installed before Run 2 [39, 40]. It is followed by the silicon microstrip tracker (SCT), which usually provides

[5] In this document, $\ell = e, \mu$. Therefore 0ℓ indicates the absence of electrons or muons reconstructed in the event.

[6] ATLAS uses a right-handed coordinate system with its origin at the nominal interaction point (IP) in the centre of the detector and the z-axis along the beam pipe. The x-axis points from the IP to the centre of the LHC ring, and the y-axis points upwards. Cylindrical coordinates (r, ϕ) are used in the transverse plane, ϕ being the azimuthal angle around the z-axis. The pseudorapidity is defined in terms of the polar angle θ as $\eta = -\ln\tan(\theta/2)$. Angular distance is measured in units of $\Delta R \equiv \sqrt{(\Delta\eta)^2 + (\Delta\phi)^2}$.

eight measurements per track. These silicon detectors are complemented by the transition radiation tracker (TRT), which enables radially extended track reconstruction up to $|\eta| = 2.0$. The TRT also provides electron identification information based on the fraction of hits (typically 30 in total) above a higher energy-deposit threshold corresponding to transition radiation.

The calorimeter system covers the pseudorapidity range $|\eta| < 4.9$. Within the region $|\eta| < 3.2$, electromagnetic calorimetry is provided by barrel and endcap high-granularity lead/liquid-argon (LAr) calorimeters, with an additional thin LAr presampler covering $|\eta| < 1.8$ to correct for energy loss in material upstream of the calorimeters. Hadron calorimetry is provided by the steel/scintillator-tile calorimeter, segmented into three barrel structures within $|\eta| < 1.7$, and two copper/LAr hadron endcap calorimeters. The solid angle coverage is completed with forward copper/LAr and tungsten/LAr calorimeter modules optimised for electromagnetic and hadronic energy measurements respectively.

The muon spectrometer (MS) comprises separate trigger and high-precision tracking chambers measuring the deflection of muons in a magnetic field generated by the superconducting air-core toroidal magnets. The field integral of the toroids ranges between 2.0 and 6.0 T m across most of the detector. A set of precision chambers covers the region $|\eta| < 2.7$ with three layers of monitored drift tubes, complemented by cathode-strip chambers in the forward region, where the background is highest. The muon trigger system covers the range $|\eta| < 2.4$ with resistive-plate chambers in the barrel, and thin-gap chambers in the endcap regions.

Interesting events are selected by the first-level trigger system implemented in custom hardware (L1), followed by selections made by algorithms implemented in software in the high-level trigger [41]. The first-level trigger accepts events from the 40 MHz bunch crossings at a rate below 100 kHz, which the high-level trigger further reduces in order to record events to disk at about 1 kHz.

An extensive software suite [42] is used for real and simulated data reconstruction and analysis, for operation and in the trigger and data acquisition systems of the experiment.

3 Data and simulated events samples

The data used in this analysis were collected using unprescaled single-lepton, dilepton or di-τ triggers [43–46] at a centre-of-mass energy of 13 TeV during the 2015–2018 LHC running periods. Events are selected for analysis only if they are of good quality and if all the relevant detector components are known to have been in good operating condition [47], which corresponds to a total integrated luminosity of $139.0 \pm 2.4\,\text{fb}^{-1}$ [48, 49].

MC simulated events are used to model most of the backgrounds from SM processes and the $H \to \tau\tau$ signal processes. A summary of all the generators used for the simulation of the signal and background processes is shown in Table 1. The same event generators as in Ref. [22] are used but the number of simulated events in all samples has been increased by at least four times which is the factor by which the integrated luminosity grew compared to the previous publication. In addition, the total number of simulated $Z \to \tau\tau$ events has been extended by a further factor of approximately four. This computing-costly process helps to densely populate the phase space where $Z \to \tau\tau$ events are produced in association with several jets.

All samples of simulated events were processed through the ATLAS detector simulation [50] based on GEANT4 [51]. The effects of multiple interactions in the same and nearby bunch crossings (pile-up) were

modelled by overlaying minimum-bias events, simulated using the soft QCD processes of Pythia 8.186 [52] with the A3 [53] set of tuned parameters and NNPDF2.3lo [54] parton distribution functions (PDF).

The decays and spin correlations for τ-leptons are handled by Sherpa for samples generated with it and by Pythia for the other MC event generators. The decays and spin correlations have been implemented in Pythia since 2014 and version 8.150 [55]. They have been thoroughly validated by comparing to Tauola [56].

Higgs boson simulation samples

The main Higgs boson production mode at the LHC is ggF with a total expected cross-section of 48.6 pb, followed by VBF (3.78 pb), associated VH (2.25 pb), and associated $t\bar{t}H$ (0.507 pb) productions. The tH process is also considered but with a cross-section of 0.092 pb its expected contribution is found to be negligible. For the ggF sample the PDF4LHC15nnlo PDF set [57] is used, while VBF and VH production samples use the PDF4LHC15nlo PDF set. $t\bar{t}H$ events are produced with the NNPDF3.0nlo [58] PDF set and tH events with the CT10 PDF [59] set. Parton shower (PS) and non-perturbative effects are modelled with Pythia 8.230 [60] with parameters set according to the AZNLO tune [61] except for $t\bar{t}H$ and tH events that rely on the A14 tune [62].

Higgs boson production via gluon-gluon fusion is simulated at next-to-next-to-leading-order (NNLO) accuracy in QCD using Powheg Box v2 [63–67]. The simulation achieves NNLO accuracy for arbitrary inclusive $gg \to H$ observables by reweighting the Higgs boson rapidity spectrum in Hj-MiNLO [68–70] to that of HNNLO [71]. The gluon-gluon fusion prediction from the MC simulated samples is normalised to the next-to-next-to-next-to-leading order (N^3LO) cross-section in QCD plus electroweak corrections at next-to-leading order (NLO) [27, 72–81].

Higgs boson production via vector-boson fusion is generated with Powheg Box v2. The prediction is accurate to NLO. It is tuned to match calculations with effects due to finite heavy-quark masses and soft-gluon resummations up to next-to-next-to-leading logarithms (NNLL). The prediction from the MC simulated samples is normalised to an approximate-NNLO QCD cross section with NLO electroweak corrections [82–84].

Higgs boson production in association with a vector boson is simulated using Powheg Box v2. The prediction is accurate to next-to-leading order for the VH plus one jet production. The loop-induced $gg \to ZH$ process is generated separately at leading order in QCD. The prediction from the MC simulated sample is normalised to cross sections calculated at NNLO in QCD with NLO electroweak corrections for $pp \to VH$ and at NLO and next-to-leading-logarithm accuracy in QCD for $gg \to ZH$ [85–91].

The production of $t\bar{t}H$ events is modelled using the Powheg Box v2 generator at NLO. The decays of bottom and charm hadrons are performed by EvtGen v1.6.0 [92]. The cross-section used to normalise the $t\bar{t}H$ process is calculated at NLO in QCD and electroweak couplings [27, 93–96]. The production of tH events was modelled using the MadGraph5_aMC@NLO 2.6.2 [97] generator at NLO. The prediction from the MC simulated samples is normalised to cross-sections calculated at NLO in QCD [98, 99].

The normalisation of all Higgs boson samples accounts for the decay branching ratio calculated with HDECAY [26, 100, 101] and Prophecy4f [102–104]. The $H \to \tau\tau$ branching ratio is assumed to follow the SM expectations and a Higgs boson mass of 125.09 GeV is assumed in the calculation of the expected cross-sections throughout this measurement.

Background processes simulation samples

The QCD production of V + jets is simulated with the Sherpa v2.2.1 [105] generator using NLO matrix elements for up to two partons, and LO matrix elements for up to four partons calculated with the Comix [106] and OpenLoops [107–109] libraries. They are matched with the Sherpa parton shower [110] using the MEPS@NLO prescription [111–114] using the set of tuned parameters developed by the Sherpa authors. The NNPDF3.0nnlo set of PDFs [58] is used and the samples are normalised to a NNLO prediction [115].

Vector-boson-fusion production of $\ell\ell jj$, $\ell\nu jj$ and $\nu\nu jj$ final states is generated using Sherpa v2.2.1 using LO matrix elements with up to two additional parton emissions. The matrix elements are merged with the Sherpa parton shower following the MEPS@LO prescription and using the set of tuned parameters developed by the Sherpa authors. Similarly to the QCD V + jets processes, the NNPDF3.0nnlo set of PDFs is employed. The samples are produced using the VBF approximation, which avoids the overlap with semi-leptonic diboson topologies by requiring a t-channel colour-singlet exchange. They are normalised using the Sherpa cross-section predictions.

QCD and Electroweak predictions of the V + jets event are grouped in the analysis and collectively referred to as V + jets in the rest of the paper.

The production of $t\bar{t}$ events is modelled using the Powheg Box v2 generator at NLO with the NNPDF3.0nlo PDF set and the h_{damp} parameter[7] set to 1.5 m_{top} [116]. The events are interfaced to Pythia 8.230 to model the parton shower, hadronisation, and underlying event, with parameters set according to the A14 tune and using the NNPDF2.3lo set of PDFs. The decays of bottom and charm hadrons are performed by EvtGen as for the $t\bar{t}H$ sample. The $t\bar{t}$ sample is normalised to the cross-section prediction at NNLO in QCD including the resummation of NNLL soft-gluon terms calculated using Top++ 2.0 [117–123].

Single-top s-channel (t-channel) production is modelled using the Powheg Box v2 [63–66] generator at NLO in QCD in the five-flavour (four-flavour) scheme with the NNPDF3.0nlo set of PDFs [58]. The events are interfaced with Pythia 8.230 [60] using the A14 tune [62] and the NNPDF2.3lo PDF set. The sample is normalised to the theory prediction calculated at NLO in QCD with Hathor 2.1 [124, 125].

Diboson pair-production processes (VV) are simulated with the Sherpa v2.2.1 or v2.2.2 generator depending on the process, including off-shell effects and Higgs-boson contributions, where appropriate. Fully leptonic final states and semi-leptonic final states, where one boson decays leptonically and the other hadronically, are generated using matrix elements at NLO accuracy in QCD for up to one additional parton and at LO accuracy for up to three additional parton emissions. Samples for the loop-induced processes $gg \to VV$ are generated using LO-accurate matrix elements for up to one additional parton emission for both cases of fully leptonic and semi-leptonic final states. The matrix element calculations are matched and merged with the Sherpa parton shower based on Catani-Seymour dipole factorisation [106, 110] using the MEPS@NLO prescription. The virtual QCD correction are provided by the OpenLoops library. The NNPDF3.0nnlo set of PDFs is used [58], along with the dedicated set of tuned parton-shower parameters developed by the Sherpa authors. The samples are normalised to a NLO prediction [126].

The background originating from $H \to WW^*$ decays is modelled using the same simulation strategy than the $H \to \tau\tau$ signal.

[7] The h_{damp} parameter is a resummation damping factor and one of the parameters that controls the matching of Powheg matrix elements to the parton shower and thus effectively regulates the high-p_T radiation against which the $t\bar{t}$ system recoils.

Table 1: Overview of the MC generators used for the main signal and background samples. The last column, labeled Order, specifies the order of the cross-section calculation used for the normalisation of the simulated samples.

Process	Generator		PDF set		Tune	Order
	ME	PS	ME	PS		
Higgs boson						
ggF	Powheg Box v2	Pythia 8	PDF4LHC15nnlo	CTEQ6L1	AZNLO	N^{3}LO QCD + NLO EW
VBF	Powheg Box v2	Pythia 8	PDF4LHC15nlo	CTEQ6L1	AZNLO	NNLO QCD + NLO EW
VH	Powheg Box v2	Pythia 8	PDF4LHC15nlo	CTEQ6L1	AZNLO	NNLO QCD + NLO EW
$t\bar{t}H$	Powheg Box v2	Pythia 8	NNPDF3.0nnlo	NNPDF2.3lo	A14	NLO QCD + NLO EW
tH	MadGraph5_aMC@NLO	Pythia 8	CT10	NNPDF2.3lo	A14	NLO
Background						
V + jets (QCD/EWK)	Sherpa v2.2.1		NNPDF3.0nnlo		Sherpa	NNLO for QCD, LO for EWK
$t\bar{t}$	Powheg Box v2	Pythia 8	NNPDF3.0nnlo	NNPDF2.3lo	A14	NNLO + NNLL
Single top	Powheg Box v2	Pythia 8	NNPDF3.0nnlo	NNPDF2.3lo	A14	NLO
Diboson	Sherpa v2.2.1		NNPDF3.0nnlo		Sherpa	NLO

4 Object and event selection

The topology of $H \to \tau\tau$ events requires the reconstruction of electrons, muons, visible products of hadronically decaying τ leptons ($\tau_{\text{had-vis}}$), jets (along with their b-tagging properties) and missing transverse energy. The number of reconstructed electrons, muons and $\tau_{\text{had-vis}}$ in each event is used to define the different channels of the analysis. Requirements on the number of additional jets in the event are used in the signal region categorisation and to suppress backgrounds.

4.1 Object reconstruction

Tracks measured in the ID are used to reconstruct interaction vertices [127], of which the one with the highest sum of squared transverse momenta of the associated tracks is selected as the primary vertex of the hard interaction.

Electrons are reconstructed from topological clusters of energy deposits in the electromagnetic calorimeter which are matched to a track reconstructed in the ID [128]. They are required to satisfy the 'Loose' identification criteria, to have $p_{\text{T}} > 15$ GeV and to be in the fiducial volume of the ID and the high granularity electromagnetic calorimeters, $|\eta_{\text{cluster}}| < 2.47$. The transition region between the barrel and endcap calorimeters ($1.37 < |\eta_{\text{cluster}}| < 1.52$) is excluded except for the $Z \to \ell\ell$ control region where they are kept to facilitate the unfolding step of the embedding procedure. In the $\tau_e\tau_\mu$ and $\tau_e\tau_{\text{had}}$ channels, the selected electron is further required to pass the 'Medium' identification, which has an associated efficiency of 80 to 90%, and 'Loose' isolation criteria [128] in the signal regions and most control regions, which has an efficiency of 90% for 15 GeV candidates, increasing to more than 98% for 30 GeV candidates. However in specific control regions used to estimate backgrounds with jets mis-identified as electrons or $\tau_{\text{had-vis}}$, the selected electron is required to fail the 'Loose' isolation criteria. In the $\tau_e\tau_{\text{had}}$ channel, the requirement on the electron transverse momentum is further tightened by 1 GeV above the nominal trigger p_{T} threshold for electrons matched to the single-electron trigger to ensure operation at the triggers plateau efficiency. Similarly, in the $\tau_e\tau_\mu$ channel, the requirement is tightened if the event is triggered by the single-electron trigger or the electron-muon one. Table 2 summarises the exact requirements used depending on the data-taking period.

Table 2: Transverse momentum thresholds applied to the selected electrons, muons and $\tau_{\text{had-vis}}$ depending on the trigger signature and the data-taking period. The p_{T} threshold of the ATLAS lowest unprescaled triggers during the Run 2 data taking are reported in Refs. [129–132]. The electron and muon trigger menu evolution throughout the Run 2 data taking are discussed in Refs. [43, 44].

Trigger signature	Data period	p_{T} threshold used in event selection
Single electron	2015	p_{T} (e) > 25 GeV
	2016-2018	p_{T} (e) > 27 GeV
Single muon	2015	p_{T} (μ) > 21 GeV
	2016-2018	p_{T} (μ) > 27.3 GeV
Electron-muon	2015-2018	p_{T} (e) > 18, p_{T} (μ) > 14.7 GeV
Ditau	2015-2018	p_{T} (leading $\tau_{\text{had-vis}}$) > 40 GeV p_{T} (sub-leading $\tau_{\text{had-vis}}$) > 30 GeV

Muons are reconstructed from signals in the MS matched with tracks inside the ID. They are required to satisfy the 'Loose' identification criteria [133], corresponding to an efficiency above 97% for all muon candidates considered in this analysis, and to have $p_{\text{T}} > 10$ GeV and $|\eta| < 2.47$. In the $\tau_e\tau_\mu$ and $\tau_\mu\tau_{\text{had}}$ channels, the selected muon in the signal regions is further required to satisfy a 'Tight' isolation criterion [133] based on track information. This requirement has an efficiency ranging from about 85% for 10 GeV muons increasing gradually to 99% for muons with transverse momentum above 50 GeV. However, in specific control regions used to estimate the jet-faking-muon and jet-faking-$\tau_{\text{had-vis}}$ backgrounds for the $\tau_e\tau_\mu$ and $\tau_\mu\tau_{\text{had}}$ channels, reconstructed muons are required to fail this 'Tight' isolation criterion. In the $\tau_\mu\tau_{\text{had}}$ channel, the requirement on the muon transverse momentum is further tightened to select events in which the single-muon trigger operates with very high efficiency. Similarly, in the $\tau_e\tau_\mu$ channel, the requirement is further tightened if the event is triggered by the single-muon trigger or the electron-muon one. Table 2 summarises the cut values used depending on the data-taking period.

Decays of τ_{had} are composed of a neutrino and a set of visible decay products, most frequently one or three charged pions and up to two neutral pions and denoted $\tau_{\text{had-vis}}$. The reconstruction of the $\tau_{\text{had-vis}}$ is seeded by jets reconstructed using the anti-k_t algorithm [134], using calibrated topological clusters [135] as inputs, with a distance parameter of $R = 0.4$ [136]. The jets form $\tau_{\text{had-vis}}$ candidates and are additionally required to have $p_{\text{T}} > 10$ GeV and $|\eta| < 2.5$. Reconstructed tracks are associated to $\tau_{\text{had-vis}}$ candidates. A multivariate discriminant is used to assess whether these tracks are likely to be produced by the charged τ_{had} decay products, and is used to reject tracks originating from other interactions, nearby jets, photon conversions or misreconstructed tracks. $\tau_{\text{had-vis}}$ objects are required to have one or three associated tracks selected by this discriminant. Their charge (q) is defined as the sum of the measured charges of these associated tracks and must have $|q| = 1$. $\tau_{\text{had-vis}}$ objects must also satisfy the requirements $p_{\text{T}} > 20$ GeV and $|\eta| < 2.47$, excluding the region $1.37 < |\eta| < 1.52$. These requirements have an efficiency of about 85% (70%) for the majority of hadronic tau decays with one (three) associated tracks measured in simulated $Z \to \tau\tau$ events. The $\tau_{\text{had-vis}}$ energy scale is determined by combining information from the associated tracks, calorimeter clusters and reconstructed neutral pions [137] using a multivariate regression technique [136] trained in MC samples.

To separate the $\tau_{\text{had-vis}}$ candidates caused by hadronic τ decays from those caused by jets initiated by quarks or gluons, a recurrent neural network (RNN) identification algorithm [138] is constructed employing information from reconstructed charged-particle tracks and clusters of energy in the calorimeter associated to $\tau_{\text{had-vis}}$ candidates as well as high-level discriminating variables. A separate boosted decision tree discriminant ('eBDT') is also constructed to reject backgrounds arising from electrons faking $\tau_{\text{had-vis}}$ (mainly from $Z \to ee$ events in the $\tau_e\tau_{\text{had}}$ channel in this analysis). This discriminant is built using information from the calorimeter and the tracking detector. Transition radiation information from the TRT system plays a key role in the performance of this discriminant. In addition, a very loose requirement on the RNN score (corresponding to a percent level efficiency loss for signal $\tau_{\text{had-vis}}$) is applied, as well as a dedicated muon veto criterion, designed to reject muons misreconstructed as $\tau_{\text{had-vis}}$ (typically due to large calorimeter energy deposits).

In the $\tau_{\text{had}}\tau_{\text{had}}$ channel, the reconstructed $\tau_{\text{had-vis}}$ objects are required to match the two $\tau_{\text{had-vis}}$ candidates of the ditau trigger, thus defining the two selected $\tau_{\text{had-vis}}$ of the event. In the $\tau_{\text{lep}}\tau_{\text{had}}$ channel, the $\tau_{\text{had-vis}}$ candidate with the highest transverse momentum satisfying a very loose requirement on the RNN score is the only one kept, the other ones are considered as jets. This minimum requirement is much lower than the final RNN selection, and leads to a small loss of signal events where a quark- or gluon-initiated jet is taken as the $\tau_{\text{had-vis}}$ candidate, quantified to be at the level of 2.5 (4)% for the ggF (VBF) production process. However, this strategy simplifies the treatment of the jet-faking-$\tau_{\text{had-vis}}$ background. Picking a minimum requirement aimed at recovering the majority of this signal efficiency loss would sacrifice 30-40% of the statistical power in the reverse-identified region, and would consequently worsen the precision of the jet-faking-$\tau_{\text{had-vis}}$ background estimate (see Section 5.2).

The $\tau_{\text{had-vis}}$ objects are further required to fulfil the 'Medium' identification criteria in the signal regions of the $\tau_{\text{lep}}\tau_{\text{had}}$ and $\tau_{\text{had}}\tau_{\text{had}}$ channels, which corresponds to an efficiency of 75% (60%) for candidates with 1(3) associated track(s). However in specific regions used to estimate the jet-faking-$\tau_{\text{had-vis}}$ background for the $\tau_{\text{lep}}\tau_{\text{had}}$ and $\tau_{\text{had}}\tau_{\text{had}}$ channels, reconstructed $\tau_{\text{had-vis}}$ objects are instead required to fail the 'Medium' identification criteria. In the $\tau_e\tau_{\text{had}}$ channel, for events where the $\tau_{\text{had-vis}}$ object has only one associated charged track, the $\tau_{\text{had-vis}}$ object is required to pass the 'Medium' working point of the eBDT algorithm, which corresponds to a 85% efficiency for candidates which already satisfy the identification requirement. The transverse momentum requirement for the $\tau_{\text{had-vis}}$ objects in the $\tau_{\text{had}}\tau_{\text{had}}$ final state is tightened to select events recorded with the $\tau_{\text{had-vis}}$ trigger operating at its plateau efficiency, as shown in Table 2. In the $\tau_{\text{lep}}\tau_{\text{had}}$ final state, the $\tau_{\text{had-vis}}$ transverse momentum cut is also tightened to $p_{\text{T}} > 30\,\text{GeV}$ to improve background rejection.

Jets are reconstructed using a particle flow algorithm [139] from noise-suppressed positive-energy topological clusters in the calorimeter using the anti-k_t algorithm with a radius parameter $R = 0.4$. Cleaning criteria are used to identify jets arising from non-collision backgrounds or noise in the calorimeters [140], and events containing such jets are removed. A jet vertex tagger [141] is used to remove jets with $p_{\text{T}} < 60\,\text{GeV}$ and $|\eta| < 2.5$ that are identified as not being associated with the primary vertex of the hard interaction. Similarly, pile-up jets in the forward region are suppressed with a 'forward JVT' [142] algorithm, exploiting jet shapes and topological jet correlations in pile-up interactions, which is applied to all jets with $p_{\text{T}} < 60\,\text{GeV}$ and $|\eta| > 2.5$. Only jets with $p_{\text{T}} > 20\,\text{GeV}$ are considered.

Jets with $p_{\text{T}} > 20\,\text{GeV}$ and $|\eta| < 2.5$ containing b-hadrons are identified using the DL1r b-tagging algorithm [143, 144]. In the $\tau_e\tau_\mu$ and $\tau_{\text{lep}}\tau_{\text{had}}$ channels, the fixed 85% efficiency working point is used while the 70% efficiency working point is used in the $\tau_{\text{had}}\tau_{\text{had}}$ channel (the target efficiencies being measured in simulated $t\bar{t}$ events). As the algorithm is used to veto b-tagged jets, the 70% efficiency working point offers a looser veto criterion which improves the sensitivity in the $\tau_{\text{had}}\tau_{\text{had}}$ channel where the backgrounds

from $t\bar{t}$ events are less significant. The rejection factors of b-tag jets initiated by c-quarks and light partons are 9.4 (2.6) and 390 (29) respectively for the 70% (85%) working point.

An overlap removal procedure is applied to avoid any double-counting between leptons, $\tau_{\text{had-vis}}$ objects, and jets.

The missing transverse momentum, $\vec{E}_{\text{T}}^{\text{miss}}$, is reconstructed as the negative vector sum of the transverse momenta of leptons, $\tau_{\text{had-vis}}$ and jets, and a 'soft-term'. The soft-term is calculated as the vectorial sum of the p_{T} of tracks matched to the primary vertex but not associated with a reconstructed lepton, $\tau_{\text{had-vis}}$ or jet [145]. The magnitude of $\vec{E}_{\text{T}}^{\text{miss}}$ is referred to as the missing transverse momentum, $E_{\text{T}}^{\text{miss}}$.

4.2 Event Selection

Events are selected if the contain a $H \to \tau\tau$ candidate in one of the final state under study ($\tau_e\tau_\mu$, $\tau_{\text{lep}}\tau_{\text{had}}$, $\tau_{\text{had}}\tau_{\text{had}}$).

The Higgs boson candidate is formed by the vector sum of the visible τ lepton decays and $\vec{E}_{\text{T}}^{\text{miss}}$. Its invariant mass ($m_{\tau\tau}^{\text{MMC}}$) is calculated using an advanced likelihood-based technique, the MMC [146], which relies on information about the τ lepton candidate momenta, the presence of additional jets, $\vec{E}_{\text{T}}^{\text{miss}}$ and the type of τ lepton decay. The addition of information about the number of reconstructed charged and neutral pions [137] in hadronic decays of the τ leptons and new parametrizations for the likelihood function derived using $Z \to \tau\tau$ MC events are improvements with respect to Ref. [22] and lead to a 1% absolute improvement of the resolution.

For each channel a series of selection criteria is applied in order to enhance the sensitivity to the SM Higgs boson signal and ensure a robust estimate of the invariant mass of the reconstructed $\tau^+\tau^-$ system. These are summarized in Table 3.

In the $\tau_e\tau_\mu$ channel, events must have a single reconstructed electron and a single reconstructed muon satisfying the criteria discussed in Section 4.1. In order to reject events coming from W+jets, Z+jets and Top[8] processes, the charges of the two reconstructed leptons must be of opposite sign, the collinear mass[9] ($m_{\tau\tau}^{\text{coll}}$) must be greater than $m_Z - 25$ GeV, and the invariant mass of the $e\mu$ system ($m_{e\mu}$) must be between 30 GeV and 100 GeV. To further reduce backgrounds from Top processes, an explicit requirement is placed to reject events with a b-tagged jet. In addition, angular requirements are placed on $\Delta R_{e\mu}$ and $|\Delta\eta_{e\mu}|$. Finally, a $p_{\text{T}} > 40$ GeV requirement is applied to the leading jet in the event to suppress backgrounds, as the signal final states considered include at least one high-p_{T} jet.

In the $\tau_{\text{lep}}\tau_{\text{had}}$ channel, events must have a single reconstructed light lepton and a single reconstructed $\tau_{\text{had-vis}}$ satisfying the criteria discussed in Section 4.1. In order to reject events coming from W+jets and Top processes, the charges of the reconstructed light lepton and the reconstructed $\tau_{\text{had-vis}}$ must be of opposite sign. The transverse mass of the lepton+$\tau_{\text{had-vis}}$ system (m_{T}) is required to be smaller than 70 GeV in order to efficiently suppress W+jets processes. To further reduce backgrounds from Top processes, an explicit requirement is placed to reject events with a b-tagged jet. In addition, angular requirements are placed on $\Delta R_{\ell\tau_{\text{had-vis}}}$ and $|\Delta\eta_{\ell\tau_{\text{had-vis}}}|$. The requirement on the leading jet in the event is the same as for the $\tau_e\tau_\mu$ channel.

[8] In the following, processes identified as 'Top' include single and pair production of top quarks.

[9] The di-τ mass reconstructed in the collinear approximation assumes that the neutrinos of the tau lepton decay propagate in the same direction as the visible decay products and that the missing transverse momentum is caused solely by those neutrinos [147].

In the $\tau_{\text{had}}\tau_{\text{had}}$ channel, events must have exactly two reconstructed $\tau_{\text{had-vis}}$ objects satisfying the criteria discussed in Section 4.1. In order to maintain low thresholds on the p_{T} of the $\tau_{\text{had-vis}}$, additional criteria were added throughout the Run 2 data-taking to the lowest unprescaled ditau trigger on the angular separation of the two $\tau_{\text{had-vis}}$ and on the presence of an additional jet in the event. The additional criteria were placed on the regions-of-interest (ROI) defining the hadronic tau candidates at the L1 trigger. In order to ensure that the core part of the ROIs of the two reconstructed $\tau_{\text{had-vis}}$ do not overlap, the criterion $\Delta R_{\tau_{\text{had-vis}}\tau_{\text{had-vis}}} > 0.6$ is applied. The extra jet trigger criterion mentioned above translates into a requirement on the presence of at least one jet with $|\eta| < 3.2$ and p_{T} greater than 70 GeV. Similarly to the $\tau_e\tau_\mu$ and $\tau_{\text{lep}}\tau_{\text{had}}$ channels, the charges of the two reconstructed $\tau_{\text{had-vis}}$ must be of opposite sign in order to reject events coming from W+jets and Top processes. Events with b-tagged jets are rejected, except for the $\text{tt}(0\ell)H \to \tau_{\text{had}}\tau_{\text{had}}$ signal region (see next Section 4.3).

Finally, criteria on $E_{\text{T}}^{\text{miss}}$ and on the momentum fraction carried by the visible decays of the τ leptons (defined as x_1, x_2 for leading and sub-leading reconstructed visible τ leptons respectively, with the $\vec{E}_{\text{T}}^{\text{miss}}$ components decomposed in the collinear approximation) are applied to improve the invariant mass estimation in the three channels.

Assuming SM predictions, 2922 $H \to \tau\tau$ events (331, 1408, 1183 in the $\tau_e\tau_\mu$, $\tau_{\text{lep}}\tau_{\text{had}}$ and $\tau_{\text{had}}\tau_{\text{had}}$ channels respectively) are expected to be reconstructed and satisfy the event selection from the $\approx 400 \cdot 10^3$ $H \to \tau\tau$ events that were produced with $|y_H| < 2.5$. In data 204 442 events are selected.

Table 3: Summary of the event selection for all sub-channels. The electron and muon p_{T} thresholds correspond to the 2016-2018 dataset. In the $\tau_e\tau_\mu$ channel, events recorded with the electron trigger must satisfy p_{T} (e) > 27 GeV and p_{T} (μ) > 10 GeV, events recorded with the muon trigger must satisfy p_{T} (e) > 15 GeV and p_{T} (μ) > 27.3 GeV and events recorded with the electron-muon trigger must satisfy p_{T} (e) > 18 GeV and p_{T} (μ) > 14.7 GeV. Thresholds for the 2015 dataset are given in Tab. 2. The b-veto requirement in the $\tau_{\mathrm{had}}\tau_{\mathrm{had}}$ channel is not applied in the tt(0ℓ)$H \rightarrow \tau_{\mathrm{had}}\tau_{\mathrm{had}}$ category. The quantities x_1 and x_2 are the momentum fraction carried by the visible decay products of the τ leptons in the collinear approximation, as described in the text.

	$\tau_e\tau_\mu$	$\tau_{\mathrm{lep}}\tau_{\mathrm{had}}$		$\tau_{\mathrm{had}}\tau_{\mathrm{had}}$
		$\tau_e\tau_{\mathrm{had}}$	$\tau_\mu\tau_{\mathrm{had}}$	
N(e)	1	1	0	0
N(μ)	1	0	1	0
N($\tau_{\text{had-vis}}$)	0	1	1	2
e p_{T} cut [GeV]	27, 15, 18	27		
μ p_{T} cut [GeV]	10, 27.3, 14.7		27.3	
$\tau_{\text{had-vis}}$ p_{T} cut [GeV]		30		40, 30
Identification	e/μ: Medium	$e/\mu/\tau_{\text{had-vis}}$: Medium		$\tau_{\text{had-vis}}$: Medium
Isolation	e: Loose μ: Tight	e: Loose	μ: Tight	
Charge	Opposite charge	Opposite charge		Opposite charge
Kinematics	$m_{\tau\tau}^{\mathrm{coll}} > m_Z - 25\,\mathrm{GeV}$ $30\,\mathrm{GeV} < m_{e\mu} < 100\,\mathrm{GeV}$	$m_{\mathrm{T}} < 70\,\mathrm{GeV}$		
b-veto	# of b-jets = 0	# of b-jets = 0		# of b-jets = 0 ($\geq$ 1 or 2 in ttH categories)
$E_{\mathrm{T}}^{\mathrm{miss}}$	$E_{\mathrm{T}}^{\mathrm{miss}} > 20\,\mathrm{GeV}$	$E_{\mathrm{T}}^{\mathrm{miss}} > 20\,\mathrm{GeV}$		$E_{\mathrm{T}}^{\mathrm{miss}} > 20\,\mathrm{GeV}$
Leading jet	$p_{\mathrm{T}} > 40\,\mathrm{GeV}$	$p_{\mathrm{T}} > 40\,\mathrm{GeV}$		$p_{\mathrm{T}} > 70\,\mathrm{GeV}$, $\lvert\eta\rvert < 3.2$
Angular	$\Delta R_{e\mu} < 2.0$ $\lvert\Delta\eta_{e\mu}\rvert < 1.5$	$\Delta R_{\ell\tau_{\text{had-vis}}} < 2.5$ $\lvert\Delta\eta_{\ell\tau_{\text{had-vis}}}\rvert < 1.5$		$0.6 < \Delta R_{\tau_{\text{had-vis}}\tau_{\text{had-vis}}} < 2.5$ $\lvert\Delta\eta_{\tau_{\text{had-vis}}\tau_{\text{had-vis}}}\rvert < 1.5$
Coll. app. x_1/x_2	$0.1 < x_1 < 1.0$ $0.1 < x_2 < 1.0$	$0.1 < x_1 < 1.4$ $0.1 < x_2 < 1.2$		$0.1 < x_1 < 1.4$ $0.1 < x_2 < 1.4$

4.3 Event Categorisation

The categorisation of selected events targets the four dominant Higgs boson production modes (see Section 1), uses their unique and characteristic signatures and is designed to match closely the production bins within the *stage 1.2* of the STXS framework. Bins of the full *stage 1.2* scheme are merged to match the available sensitivity of the selected $H \to \tau\tau$ events. Both the STXS bins and the event categories are illustrated in Fig. 1.

Requirements on the reconstructed transverse Higgs boson momentum, $p_{\mathrm{T}}(H)$, and on properties of additional jets are described in the following. Events in the VBF, V(had)H and tt(0ℓ)$H \to \tau_{\mathrm{had}}\tau_{\mathrm{had}}$ categories are further split with BDT taggers into two sub-categories, the first (suffixed _1) with enhanced signal fractions and the second (suffixed _0) containing the remaining events. All taggers are designed inclusively for all di-τ decay modes and the variables are chosen to avoid any potential bias in the $m_{\tau\tau}^{\mathrm{MMC}}$ distribution. For each tagger, this is verified by comparing templates of the $m_{\tau\tau}^{\mathrm{MMC}}$ distribution for signal and background processes between the relevant sub-categories. The taggers are described in the following and their input variables are listed in Table 4.

tt(0ℓ)$H \to \tau_{\mathrm{had}}\tau_{\mathrm{had}}$ categorisation

The event selection in the tt(0ℓ)$H \to \tau_{\mathrm{had}}\tau_{\mathrm{had}}$ category requires the presence of either six jets with p_{T} greater than 20 GeV including at least one b-tagged jet or 5 jets including at least two b-tagged jets. The events satisfying these criteria are not considered by the analysis reported in Ref. [34].

The signal enhancing split in this category is using two BDTs that treat $t\bar{t}H$ events as signal, and $Z \to \tau\tau$ and $t\bar{t}$ events as the backgrounds to optimize against, respectively. A variety of two-dimensional combinations of requirements on the two BDT scores were studied, using the expected counting experiment statistical significance[10], including an estimate of the systematic uncertainties on the background normalizations, as an estimator for their performance; none was found to outperform a simple rectangular requirement in the plan formed by the two BDT scores., which was ultimately selected. Of all Higgs boson events selected in the ttH_0 (ttH_1) categories 74% (92%) are due to the $t\bar{t}H$ process.

All other event categories in the $\tau_{\mathrm{had}}\tau_{\mathrm{had}}$ channel require that no b-tagged jets with $p_{\mathrm{T}} > 20$ GeV and $|\eta| < 2.5$ are present.

VBF categorisation

The VBF categories are designed to select Higgs bosons produced from the fusion of two vector bosons emitted by two quarks of the colliding protons. The scattering quarks give rise to two high-p_{T} jets with a large rapidity gap and therefore large invariant mass m_{jj}. This signature allows VBF events to be experimentally distinguished from the other Higgs production modes and $Z \to \tau\tau$ events.

To match the STXS $qq \to H$ particle-level $p_{\mathrm{T}}^{\mathrm{jet}}$ requirement and m_{jj} binning, events selected in the VBF categories must have $m_{jj} > 350$ GeV and p_{T} of the sub-leading jet greater than 30 GeV. Additional selection criteria are applied to enhance the VBF Higgs production mode over the $Z \to \tau\tau$ background. The product of the pseudorapidities of the two leading jets ($\eta(j_0) \times \eta(j_1)$) is required to be negative (i.e.

[10] 'Poisson-Binomial model' in [148]

Table 4: Variables used in the four multivariate taggers employed in the analysis. For each tagger, the presence of a • indicates whether the variable is used or not. The symbol τ stands for any reconstructed τ lepton candidate (electron, muon or $\tau_{\text{had-vis}}$) as appropriate in each channel. The symbols $\tau\tau$ and jj indicate the vectorial sums of the momenta of two τ lepton candidates and of the two leading jets, respectively. The Higgs boson candidate H is formed by the vector sum of the τ lepton candidates and $\vec{E}_{\text{T}}^{\text{miss}}$. The W candidate is built as the pair of non-b-tagged jets in the event with invariant mass closest to m_W. The top-quark candidate is built as the system of the W candidate and a b-tagged jet in the event with invariant mass closest to m_t.

	Variable	VBF	V(had)H	ttH vs $t\bar{t}$	ttH vs $Z \to \tau\tau$
Jet properties	Invariant mass of 2 leading jets	•	•		
	$p_{\text{T}}(jj)$	•	•		
	Product of η of 2 leading jets	•			
	Sub-leading jet p_{T}	•			
	Leading jet η				•
	Sub-leading jet η				•
	Scalar sum of all jets p_{T}			•	•
	Scalar sum of all b-tagged jets p_{T}				•
	Best W-candidate dijet invariant mass			•	•
	Best t-quark-candidate three-jet invariant mass			•	•
Angular distances	$\Delta\phi$(jet 0, jet 1)	•			
	$\lvert\Delta\eta$(jet 0, jet 1)$\rvert$	•	•		
	ΔR(jet 0, jet 1)		•		
	$\Delta R(\tau\tau, jj)$		•		
	$\Delta R(\tau,\ \tau)$		•	•	
	Smallest ΔR (any 2 jets)			•	
	$\lvert\Delta\eta(\tau, \tau)\rvert$			•	•
τ prop.	$p_{\text{T}}(\tau\tau)$			•	
	Sub-leading τ p_{T}				•
	Sub-leading τ η				•
H cand.	$p_{\text{T}}(Hjj)$	•	•		
	$p_{\text{T}}(H)/p_{\text{T}}(jj)$		•		
$\vec{E}_{\text{T}}^{\text{miss}}$	Missing transverse energy $E_{\text{T}}^{\text{miss}}$		•	•	•
	Smallest $\Delta\phi$ $(\tau, \vec{E}_{\text{T}}^{\text{miss}})$				•

jets must be in opposite hemispheres of the detector). The absolute difference in pseudorapidity ($|\Delta\eta_{jj}|$) is required to be greater than 3. Finally the visible decay products of the τ leptons are required to be reconstructed in the rapidity gap of the VBF jets.

The VBF tagger is optimized treating both ggF $H \to \tau\tau$ and $Z \to \tau\tau$ events as backgrounds and relies solely on observables based on the kinematics of the two leading jets (see Table 4). While the expected contribution from ggF $H \to \tau\tau$ events is small, the considerably larger theoretical uncertainty associated with its cross-section prediction can significantly enlarge the systematic uncertainty on the VBF production cross-section measurement.

The BDT score requirement used to define the categories was optimised to give the smallest uncertainty on the VBF cross-section, and provides a selection where the fraction of VBF events among all Higgs boson events is about 94% (63%) in the VBF_1 (VBF_0) region.

V(had)H categorisation

To match the STXS $qq \to V(\to qq)H$ particle-level $p_{\mathrm{T}}^{\mathrm{jet}}$ requirement and m_{jj} binning, events selected in the V(had) categories must satisfy 60 GeV $< m_{jj} <$ 120 GeV and p_{T} of the sub-leading jet greater than 30 GeV.

The V(had)H tagger was trained treating all Higgs events produced by processes other than VH as background. The BDT score requirement used to define the two categories was optimized to give the smallest uncertainty on the V(had)H cross-section, and provides a selection where the expected fraction of V(had)H among all Higgs boson events is 66% (24%) in the VH_1 (VH_0) category.

Boost categorisation

Events failing the criteria of the VBF, V(had)H and ttH categories but with high-p_{T} Higgs candidates are considered for the boost categories targeting ggF events with large Higgs boson transverse momentum. The reconstructed Higgs boson transverse momentum, $p_{\mathrm{T}}(H)$, is determined from the Higgs boson candidate defined by the vectorial sum of the momenta of the visible decay products of the τ leptons and $\vec{E}_{\mathrm{T}}^{\mathrm{miss}}$. Events in the boost category must satisfy $p_{\mathrm{T}}(H) > 100$ GeV. To match the STXS $gg \to H$ particle-level requirements, events are further categorised based on $p_{\mathrm{T}}(H)$ and on the total number of jets with p_{T} greater than 30 GeV ($\mathrm{N}_{\mathrm{jets}}(p_{\mathrm{T}} > 30\,\mathrm{GeV})$). Table 5 describes this categorisation. Events with $p_{\mathrm{T}}(H) < 200$ GeV are split into 1-jet and ≥2-jet categories, while for $p_{\mathrm{T}}(H) > 200$ GeV events with at least 1 jet are considered without further splitting on the jet multiplicity of the event.

Table 5: Definition of the six categories in the boosted phase space.

$\mathrm{N}_{\mathrm{jets}}(p_{\mathrm{T}} > 30\,\mathrm{GeV})$	$p_{\mathrm{T}}(H)$ bins in GeV			
	[100, 120]	[120, 200]	[200, 300]	[300, ∞[
Exactly 1	boost_0_1J	boost_1_1J	boost_2	boost_3
At least 2	boost_0_ge2J	boost_1_ge2J		

The three analysis channels are therefore split in six kinematic categories in the boost phase space for a total of eighteen categories in the fit performed for the cross-sections measurement.

Summary

Nine bins of the STXS framework are targeted in the measurement presented in this paper and are illustrated in Fig. 1. The expected signal yields for each of these bins is presented on Fig. 2(a) while Fig. 2(b) illustrates the relative population of these nine bins in each reconstructed category described in this section. As illustrated in Fig. 2, ggF events produced with $p_{\mathrm{T}}(H) < 200\,\mathrm{GeV}$ and two additional jets forming a system with $m_{jj} > 350\,\mathrm{GeV}$ are mainly reconstructed in the VBF_0 category (61%) and in the boost_1_ge2J category (36%). They are difficult to select in a single category but through the simultaneous usage of all the categories, their production rate can be measured. In contrast, the reconstructed ggF event candidates satisfying $60\,\mathrm{GeV} < p_{\mathrm{T}}(H) < 120\,\mathrm{GeV}$ are further split depending if they are produced with a single jet (boost_0_1J) or if they are produced with two jets forming a system with $m_{jj} < 350\,\mathrm{GeV}$ (boost_0_ge2J). However the categorisation does not provide enough sensitivity to measure these two contributions individually and they are therefore merged together.

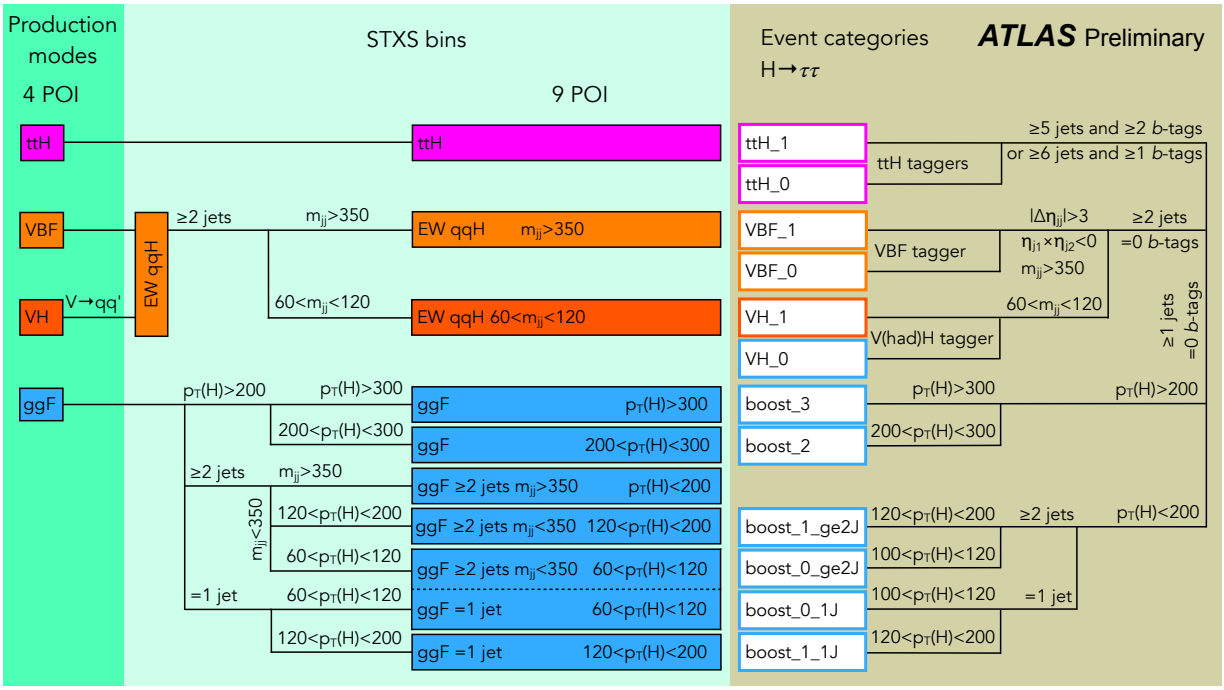

Figure 1: Sketch of the event categorisation and the STXS bins targeted. The dominant STXS bin contributing to each event category is indicated by the colour of the category box or the STXS bin adjacent to it. The background colours on the left side indicate which parameters of interest (POI) are estimated in the fit. The requirements on $p_{\mathrm{T}}(H)$ and m_{jj} are given in units of GeV.

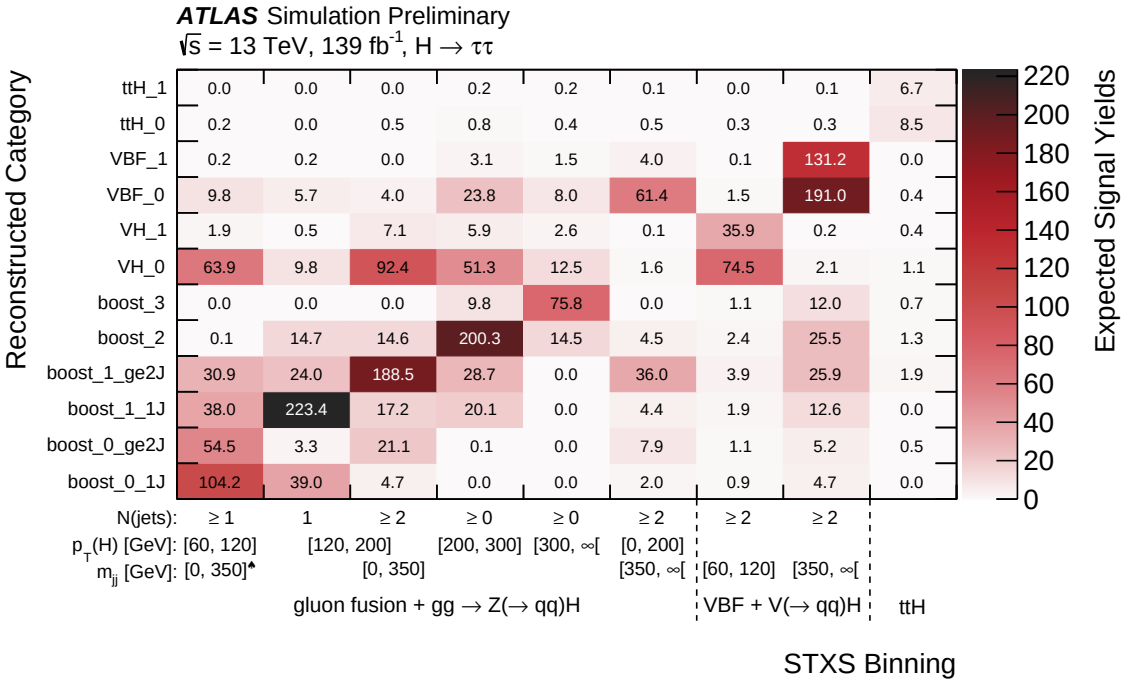

(a)

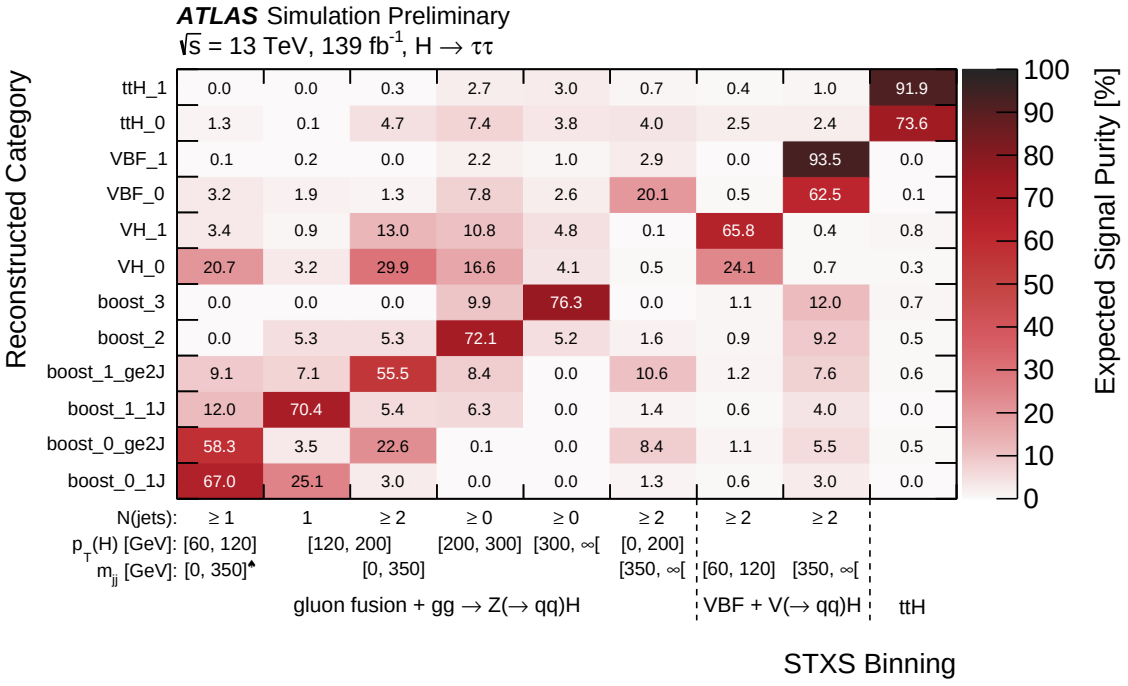

(b)

Figure 2: (a) Expected $H \to \tau\tau$ signal yield in each of the reconstructed event category of the analysis (y-axis) for each of the nine measured STXS bins (x-axis). (b) Relative contribution of each of the nine measured STXS bins to the total $H \to \tau\tau$ signal expectation in each reconstructed event category. The spades symbol (♠) indicates that the criteria on m_{jj} only apply to events with at least two reconstructed jets. Yields are summed over the three di-τ decay channels ($\tau_e\tau_\mu$, $\tau_{\text{lep}}\tau_{\text{had}}$, $\tau_{\text{had}}\tau_{\text{had}}$).

5 Background modelling

The expectations from SM processes other than the $H \to \tau\tau$ signal in the phase space of the analysis are evaluated using a mixture of simulations and data-driven techniques. Processes with $\tau_{\text{had-vis}}$, prompt light leptons or light leptons from τ-lepton decays are estimated through simulations. Among these, $Z(\to \tau\tau)$ + jets and Top processes are dominant, and dedicated control regions are employed to validate the simulations of both processes and to constrain their normalisation in the signal regions. For the $Z(\to \tau\tau)$ + jets background, a control region enriched in $Z(\to \ell\ell)$ + jets events is defined as described in Section 5.1. In the $\tau_e\tau_\mu$ and $\tau_{\text{lep}}\tau_{\text{had}}$ channels, control regions enriched in top-induced processes are defined by replacing the b-jet veto from the event selection (see Table 3) by requiring at least one b-tagged jet.

Using these control regions, the yield predictions and the modelling of the $m_{\tau\tau}^{\text{MMC}}$ observable from the simulations are checked in each event category (see 4.3). A very good agreement with the data is observed.

Smaller background contributions are due to diboson, $Z(\to \ell\ell)$ + jets and $H \to WW^*$ processes. They are normalised to their theoretical expectations. Contributions from light- and heavy-flavour jets misidentified as electrons, muons or $\tau_{\text{had-vis}}$, as well as non-prompt electrons or muons, collectively referred to as Misidentified τ background, are estimated using data-driven techniques. Their estimation is detailed in Section 5.2.

Figure 3 illustrates the measured composition of the selected events in each category of the analysis.

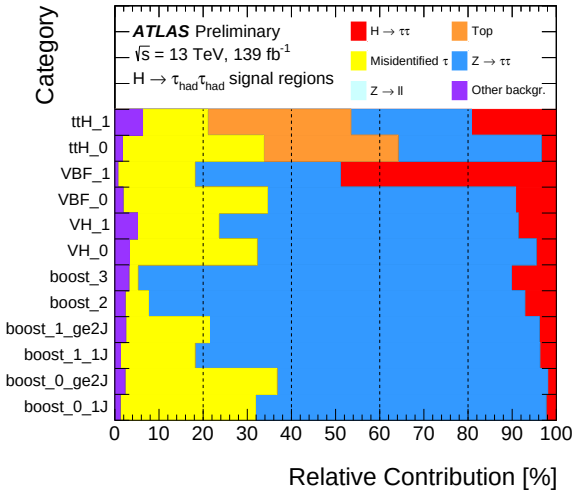

(a) $\tau_{\text{had}}\tau_{\text{had}}$

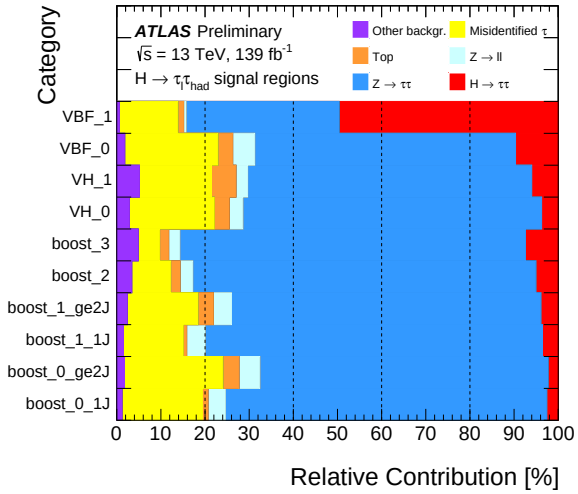

(b) $\tau_{\text{lep}}\tau_{\text{had}}$

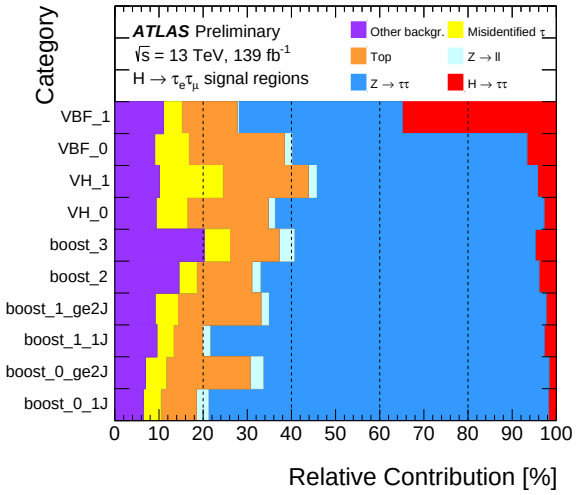

(c) $\tau_e\tau_\mu$

Figure 3: Relative contribution of each process to the total measured yields in each category of the analysis for the (a) $\tau_{\text{had}}\tau_{\text{had}}$, (b) $\tau_{\text{lep}}\tau_{\text{had}}$ and (c) $\tau_e\tau_\mu$ channels, within 100 GeV$< m_{\tau\tau}^{\text{MMC}} <$ 150 GeV. Other backgr. include diboson, $t\bar{t}+V$ and $H \to WW^*$ processes.

5.1 $Z \to \tau\tau$ background modelling using $Z \to \ell\ell$ events

Events from the $Z(\to \tau\tau)$ + jets process form the dominant source of background in this measurement. They account for 79 % of the background across all signal regions, and up to 90 % of the background in the most boosted regime investigated in the analysis. They are estimated using MC simulations validated with data.

In order to mimic as well as possible the Z boson kinematics and the associated production of jets in $Z(\to \tau\tau)$ + jets events selected in the signal regions, the selected $Z(\to \ell\ell)$ + jets events are modified through a simplified implementation of the embedding procedure. While the original method presented in Refs. [36, 37] relied on substituting the detector signatures of the objects before re-reconstructing the event, the simplified embedding consists of a rescaling of the transverse momentum of each reconstructed lepton through parameterizations, followed by a re-computation of all the relevant kinematic quantities in the analysis. The method used entails a significant reduction of complexity.

Embedding techniques are of particular interest to this analysis, where no study of the $Z(\to \tau\tau)$ + jets background can be performed in data without looking at the signal regions. In this context, the simplified embedding can be applied to data events passing the $Z(\to \ell\ell)$ + jets selection, thus obtaining a $Z \to \tau\tau$ control region that is orthogonal to the signal region. This control region can also be used to measure the $Z \to \tau\tau$ normalization in a phase space relevant to this measurement.

The $Z(\to \ell\ell)$ + jets events are selected using the single lepton triggers and are required to have exactly two electrons or two muons with opposite charge. The selected electrons and muons must satisfy the identification and isolation criteria defined in Table 3. Additionally the invariant mass of the dilepton system is required to be above 80 GeV. The selected sample contains about $9.3 \cdot 10^6$ data events and 99% of them are expected to come from $Z(\to \ell\ell)$ + jets processes. A small contribution from diboson and Top processes with two electrons or two muons in the final state is also expected and the embedding procedure is also applied to them. Contributions from processes with jets mis-identified as leptons were verified to be negligible. Selected events in data and simulation are then randomly split in three subsets to provide statistically-independent control regions for the $\tau_e\tau_\mu$, $\tau_{\text{lep}}\tau_{\text{had}}$ and $\tau_{\text{had}}\tau_{\text{had}}$ signal regions respectively.

Weights derived in simulations are applied to each event to remove the kinematic biases and normalization effects introduced by the electron and muon trigger, reconstruction, identification, and isolation algorithms. The four-vectors of the reconstructed electrons and muons are used to pair each lepton in the $Z(\to \ell\ell)$ + jets event with a scaling term, which parametrizes the effects of τ lepton decay kinematics and of the energy calibration algorithms for τ leptons with similar four-vectors. The scaling term is derived in a two dimensional term defined by the transverse momentum and the pseudorapidity of the τ lepton before it decays. The original four-vectors of the electrons and muons are scaled using this term so that they match those of the visible reconstructed decay products of either leptonically- or hadronically-decaying τ leptons. The $Z(\to \ell\ell)$ + jets event yields are then re-weighted to account for the expected efficiencies of the reconstruction, identification and calibration steps for the visible τ decay products.

The per-lepton weights assume collinearity of the τ lepton and its decay products and cannot take into account any correlation between the Z boson decay products. All event variables used in the signal region definitions are re-calculated using the kinematics of the new final state physics objects, and a weight is applied to each event to account for the expected trigger efficiency associated with these objects. The implementation of the new embedding procedure is validated by comparing $Z \to \ell\ell$ simulated events, with this procedure applied, to $Z \to \tau\tau$ simulations, where both kinematic and spin-correlation effects are modelled correctly. A good agreement between the distributions of the two samples, is shown in Fig. 4

for two illustrative cases and indicates that the assumptions made have negligible impact on the relevant observables.

Distributions for this control region, and a comparison to the embedding of all the simulated background processes, are shown in Fig. 5. The observed discrepancies are consistent with the results reported in dedicated measurements of the Z + jets processes [149, 150].

All uncertainties on the reconstructed physics objects used in embedding are propagated through the full procedure, including those associated with the parameterizations. Dedicated uncertainties affecting each control region are assigned to account for the differences in modelling observed between the $Z \to \tau\tau$ and embedded $Z \to \ell\ell$ MC predictions, which are expected to come from approximations associated with the simplified embedding procedure. These uncertainties are derived by studying the change in the data-to-simulation normalization factors as events are migrated between different control regions to cover the observed acceptance mismodeling. They are found to be at the 1% level.

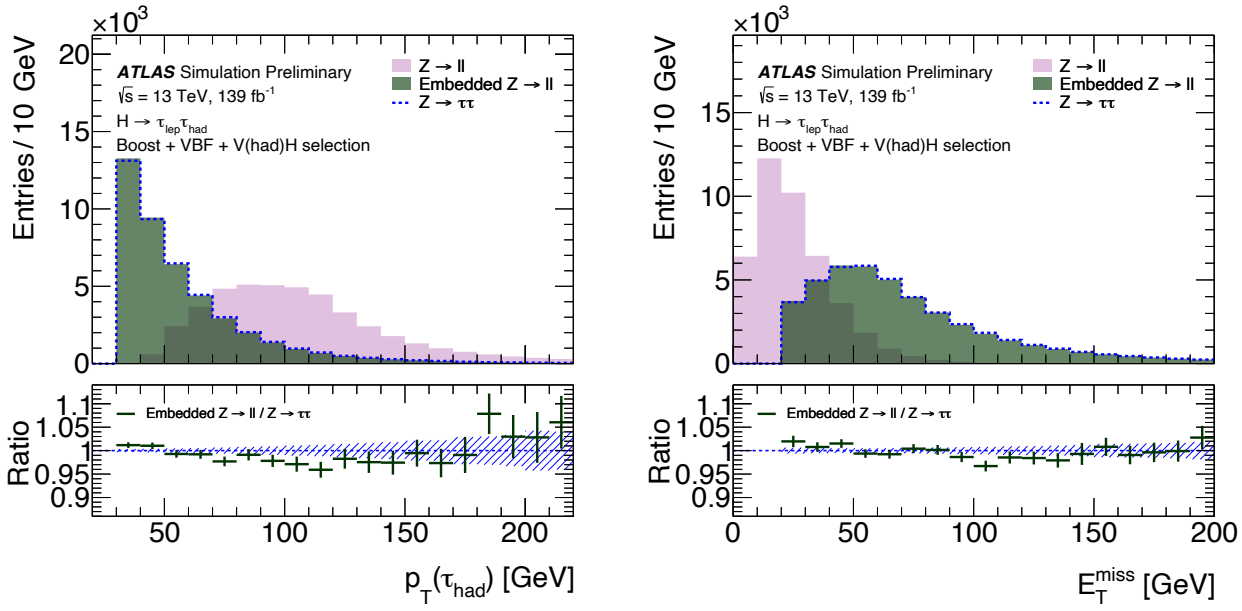

(a) p_{T} (τ_{had})

(b) $E_{\mathrm{T}}^{\mathrm{miss}}$

Figure 4: Comparison of kinematic quantities for $Z \to \ell\ell$ simulated events in the $\tau_{\mathrm{lep}}\tau_{\mathrm{had}}$ channel before (light purple histogram) and after (dark green histogram) the embedding procedure, in the Boost, VBF and V(had)H phase spaces combined. The distribution for $Z \to \tau\tau$ simulated events (dashed blue line) is also shown. (a) p_{T} distribution of the reconstructed lepton reconstructed with the highest p_{T} in the event. A scaling term is applied to the variable in the embedding procedure as described in the text. (b) $E_{\mathrm{T}}^{\mathrm{miss}}$ distribution. The bottom panels display the ratio between embedded $Z \to \ell\ell$ events and $Z \to \tau\tau$ events, with statistical uncertainties included.

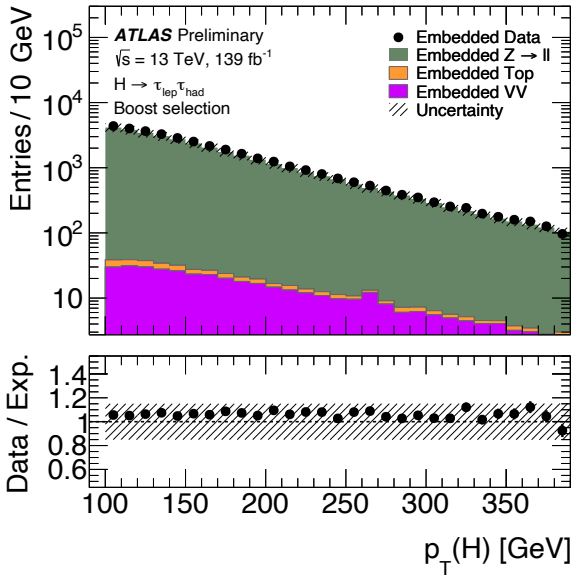

(a) $p_{\mathrm{T}}(H)$ with Boost sel.

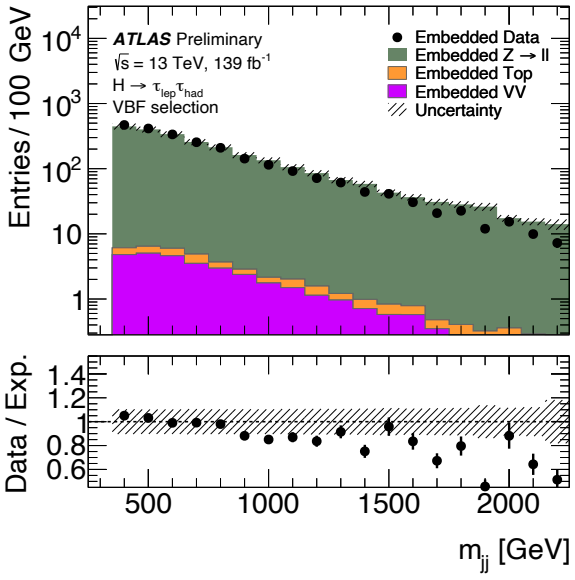

(b) m_{jj} with VBF sel.

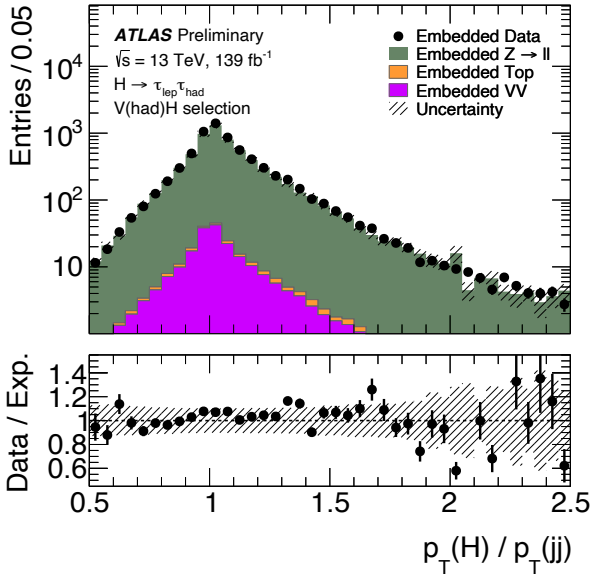

(c) $p_{\mathrm{T}}(H)/p_{\mathrm{T}}(jj)$ with V(had)H sel.

Figure 5: Comparison of MC simulation prediction with data after the embedding procedure is applied to mimic the $\tau_{\mathrm{lep}}\tau_{\mathrm{had}}$ event selection: (a) $p_{\mathrm{T}}(H)$ in the Boost phase space, (b) m_{jj} in the VBF phase space and (c) $p_{\mathrm{T}}(H)/p_{\mathrm{T}}(jj)$ in the V(had)H phase space. The bottom panels represent the agreement between the embedded data and the embedded simulation samples. The uncertainty is the quadratic sum of the statistical uncertainty on the simulated events and the systematic uncertainties on the simulation. Only the acceptance uncertainties in each category are considered. The shape variations, translating to potential bin-by-bin changes, were estimated to be minor and are not displayed.

5.2 Data driven estimate of Misidentified τ processes

Processes with at least one jet mis-identified as an electron, muon or τ_{had} are collectively referred to as misidentified τ background. They account for a fraction of the total background ranging from 5 to 25% with smaller importance in more boosted categories. They are evaluated in a similar fashion in the three channels of the analysis. First, data events are selected using the same criteria as for the SRs with the exception of the criteria on the electron or muon identification and isolation requirements and the $\tau_{\text{had-vis}}$ identification criteria. These criteria are loosened or inverted depending on the specific methodology used in each channel. Then, transfer factors are computed in dedicated control regions. These factors are used to correct for the kinematic and normalization differences between the events with altered isolation or identification criteria and the SRs.

In the $\tau_e\tau_\mu$ channel, the misidentified τ background is estimated using the matrix-method technique [151]. Data events are selected by removing from the nominal selection the lepton isolation criteria, and loosening the identification criteria for electrons. The expected number of fake leptons in the SR are computed from a system of equations relating the efficiencies for real (ϵ_r) and fake leptons (ϵ_f) to the observed event yields. The efficiencies are estimated separately for electrons and muons and are parameterised as a function of the p_{T} and η of the leptons. The real lepton efficiencies ϵ_r are estimated using simulations while the fake lepton efficiencies ϵ_f are measured using data events selected with two leptons of the same charge. For the latter the contribution from events with real leptons is subtracted using MC simulations; they account for approximately 35% of the 1333 selected events.

Dedicated uncertainties on these predictions are estimated and account for: statistical uncertainties on the derived efficiencies ($\sim$ 10%), dependencies of ϵ_f on the number of jets and b-tagged jets in the final state ($\sim$ 35%), the dependency of ϵ_r on whether they are measured in $t\bar{t}$, $Z(\rightarrow \ell\ell)$ + jets or $Z(\rightarrow \tau\tau)$ + jets events ($\sim$ 15%), and the uncertainty associated with the normalization of the contribution from real leptons during the measurement of ϵ_f ($\sim$ 15%).

In the $\tau_{\text{lep}}\tau_{\text{had}}$ channel, the misidentified τ background refers to events with a jet mis-identified as a $\tau_{\text{had-vis}}$. Contributions with a real τ_{had} and a jet mis-identified as an electron or a muon are estimated from simulations to be negligible. The misidentified τ background is evaluated using the fake-factor technique [152]. Data events are selected if they satisfy a very loose requirement on the $\tau_{\text{had-vis}}$ identification score but fail the 'Medium' working point criteria (reverse-identified). All other criteria of the nominal selection of the $\tau_{\text{lep}}\tau_{\text{had}}$ channel are applied. Residual contributions from processes with real $\tau_{\text{had-vis}}$ satisfying this requirement are evaluated using simulations and subtracted accordingly. They account for approximately 18% of the 136500 selected events.

The distribution of the misidentified τ background component in the SR is obtained by multiplying the contribution of the data events selected by the reverse-identified criterion with a fake factor defined as the ratio of misidentified $\tau_{\text{had-vis}}$ that either pass or fail the 'Medium' working point of the $\tau_{\text{had-vis}}$ identification algorithm. These fake factors are parameterised as a function of the p_{T} and track multiplicity of the $\tau_{\text{had-vis}}$. Two sets of fake factors are derived in separate regions and then combined for the final estimate. The first set is derived in a region enriched in W+jets processes obtained by inverting the SR criteria on m_{T} (see Table 3). The second set is derived in a control region enriched in QCD multijet processes obtained by reverting the isolation criteria on the selected electron or muon. An estimate of the fraction of events expected to originate from QCD multijets is used to determine the relative weighting of both sets of fake factors; it is parameterized as a function of the p_{T} and η of the $\tau_{\text{had-vis}}$ candidate. This estimate is achieved by scaling the number of events in the second control region by the ratio of events where the light lepton

fails or passes the isolation criteria, measured in another QCD enriched region where the τ_{lep} and τ_{had} have the same charge.

Uncertainties in the fake factors are estimated, and account for statistical uncertainties in the fake factors and their relative weighting ($\sim$ 15%), for uncertainties associated with the subtraction of the residual contributions from processes with real τ_{had} ($\sim$ 10%), and for uncertainties in the flavour composition ($\sim$ 10%), taken from comparisons between the estimates and backgrounds observed in a dedicated validation region.

In the $\tau_{\text{had}}\tau_{\text{had}}$ channel, the misidentified τ background is also determined using a fake-factor approach. The method slightly differs from the $\tau_{\text{lep}}\tau_{\text{had}}$ channel: the fake-factors are parameterised to simultaneously account for processes with one or two jets misidentified as $\tau_{\text{had-vis}}$. Additionally the reconstructed $\tau_{\text{had-vis}}$ candidates are matched to their high-level-trigger counterparts. The fake factors are estimated in the W+jets enriched region defined for the $\tau_{\text{lep}}\tau_{\text{had}}$ channel, but with the addition of the trigger-matching requirement in the $\tau_{\text{had-vis}}$ definition.

Two sets of fake factors are computed in control regions defined with two $\tau_{\text{had-vis}}$. The first alternate set is derived by inverting the criteria on the $\Delta\eta(\tau_{\text{had-vis}}, \tau_{\text{had-vis}})$ variable with respect to the signal region. The second is derived by requiring the charge of the two $\tau_{\text{had-vis}}$ to have the same sign. The comparison of these two alternate sets with the nominal fake factors is used to estimate the uncertainty in the composition of the misidentified τ background ($\sim$ 15%). Two additional uncertainties on the misidentified τ bacground estimate in the $\tau_{\text{had}}\tau_{\text{had}}$ channel are considered: the statistical uncertainty in the fake factor calculation ($\sim$ 15%), uncertainties related to the choice of the parametrisation of the fake factors ($\sim$ 5%).

In the $\tau_e\tau_\mu$ and $\tau_{\text{lep}}\tau_{\text{had}}$ channel, the analysis employs control regions enriched in top processes. Heavy-flavour jets misidentified as electrons, muons or $\tau_{\text{had-vis}}$ represent a sizeable fraction of the expected contributions. To estimate these contributions, the data-driven estimate described above is repeated while replacing the b-jet veto with a b-tagged jet requirement to mimic the control region selection.

Figure 6 illustrates the modelling of the misidentified τ background in validation regions for each channel. The agreement between the observed data and the prediction is good in all cases.

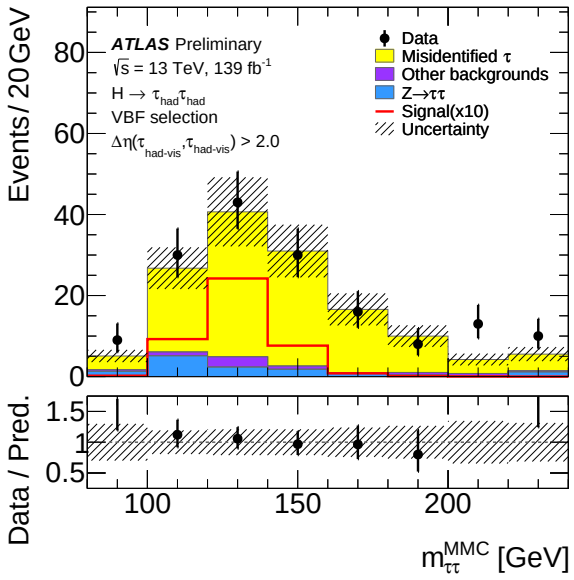

(a) $\tau_{\text{had}}\tau_{\text{had}}$

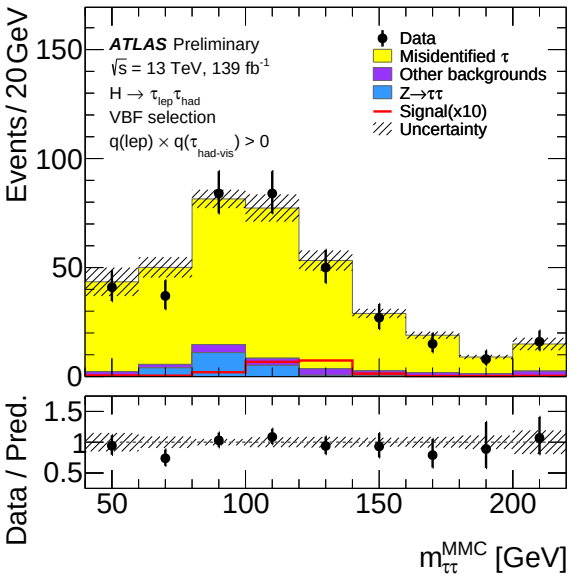

(b) $\tau_{\text{lep}}\tau_{\text{had}}$

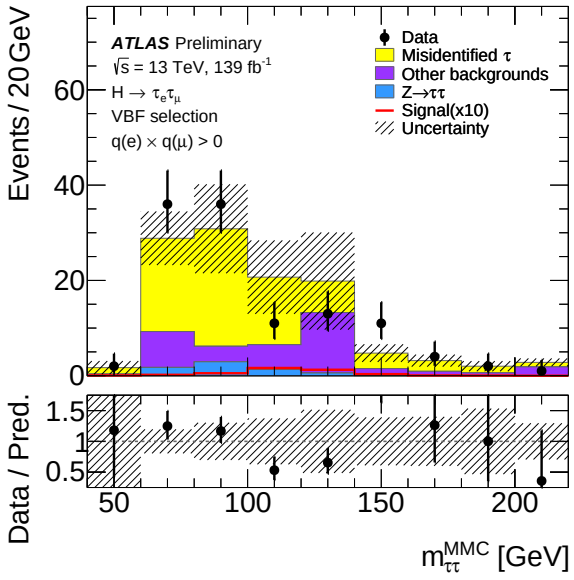

(c) $\tau_e\tau_\mu$

Figure 6: Validation of the data-driven estimate of the processes (a) with jets misidentified as $\tau_{\text{had-vis}}$ in events with $\Delta\eta(\tau_{\text{had-vis}}, \tau_{\text{had-vis}})$>2.0 in the $\tau_{\text{had}}\tau_{\text{had}}$ final state, (b) with light leptons and $\tau_{\text{had-vis}}$ of the same charge in the $\tau_{\text{lep}}\tau_{\text{had}}$ channel, and (c) with jets misidentified as electrons or muons in $\tau_e\tau_\mu$ events with same charge leptons. The hashed band represents the statistical uncertainty due to the limited size of the simulated samples and the systematic uncertainty of the data-driven estimate.

6 Systematic uncertainties

Systematic uncertainties affect the yields in the various signal and control regions as well as the shape of the main fit observable ($m_{\tau\tau}^{\text{MMC}}$). They can be categorised in three main groups: the experimental uncertainties, the theoretical uncertainties for the backgrounds and the theoretical uncertainties for the signal. They are detailed in the following sections. Their impact on the measured $pp \to H \to \tau\tau$ cross-section is summarised in Table 6. Systematic uncertainty sources are parameterised in the statistical analysis using nuisance parameters with gaussian priors (see Section 7). Figure 7 lists the ten nuisance parameters with the highest impact on the measured $pp \to H \to \tau\tau$ cross-section by decreasing order.

Table 6: Summary of the different sources of uncertainty in decreasing order of their impact on $\sigma(pp \to H \to \tau\tau)$. Their observed and expected fractional impacts, both computed by the fit, are given, relative to the $\sigma(pp \to H \to \tau\tau)$ value. Experimental uncertainties in reconstructed objects combine efficiency and energy/momentum scale and resolution uncertainties. Background sample size includes the bin-by-bin statistical uncertainties in the simulated backgrounds as well as statistical uncertainties in misidentified τ backgrounds, which are estimated using data.

Source of uncertainty	Impact on $\Delta\sigma / \sigma(pp \to H \to \tau\tau)$ [%]	
	Observed	Expected
Theoretical uncertainty in signal	8.1	8.6
Jet and $\vec{E}_{\text{T}}^{\text{miss}}$	4.2	4.1
Background sample size	3.7	3.4
Hadronic τ decays	2.0	2.1
Misidentified τ	1.9	1.8
Luminosity	1.7	1.8
Theoretical uncertainty in Top processes	1.4	1.2
Theoretical uncertainty in Z+jets processes	1.1	1.1
Flavor tagging	0.5	0.5
Electrons and muons	0.4	0.3
Total systematic uncertainty	11.1	11.0
Data sample size	6.6	6.3
Total	12.8	12.5

6.1 Experimental uncertainties

In addition to the object misidentification rate already discussed in Section 5.2, experimental systematic uncertainties include those on the trigger, reconstruction, identification and isolation efficiencies of the final-state particle candidates, and their energy scale and resolution. These uncertainties affect the shape of the $m_{\tau\tau}^{\text{MMC}}$ distribution, the background yields and the signal cross section through their effects on the acceptance and the migration between different categories.

The dominant uncertainties on the measurement of the total cross section are related to the jet energy scale and resolution, to the $\tau_{\text{had-vis}}$ candidate identification and energy scale, and to the object misidentification rates, as shown in Table 6. The uncertainties related to the reconstruction and identification of electrons and muons and the jet b-tagging efficiency have only a minor impact on the measurement.

The jet energy scale uncertainty for central jets ($|\eta|$<1.2) varies from 1% for a wide range of jet p_{T} (250 GeV $< p_{\mathrm{T}} <$ 2000 GeV), to 5% for very low p_{T} jets (20 GeV) and 3.5% for very high-p_{T} jets ($>$ 2.5 TeV). The jet energy resolution uncertainty ranges from (24 ± 1.5)% for jets with p_{T} of 20 GeV to (6 ± 0.5)% for those with p_{T} of 300 GeV [153].

The uncertainties on the $\tau_{\text{had-vis}}$ identification efficiency are in the range of 2 to 6%, while the trigger efficiency and the eBDT efficiency uncertainties are of the order of 1 to 1.5% and 1 to 2%, respectively. All these uncertainties are parameterised as a function of the $\tau_{\text{had-vis}}$ p_{T} and number of associated tracks (identification and trigger efficiency) or τ decay mode (eBDT efficiency). As this analysis is highly sensitive to the $\tau_{\text{had-vis}}$ reconstruction efficiency uncertainty due to the introduction of the high-statistics $Z \to \ell\ell$ control regions, it is left as a free parameter in the fit and measured in-situ; the associated uncertainty is found to be at the 2% level. For the $\tau_{\text{had-vis}}$ energy scale, the total uncertainty is in the range of 1 to 4%, arising from a combination of measurements: a direct measurement with $Z \to \tau\tau \to \mu\tau_{\text{had-vis}} + 3\,\nu$ events, measurements of the calorimeter response to single particles, and comparisons between simulations using different detector geometries or GEANT4 physics lists. This uncertainty is also parameterised as a function of the $\tau_{\text{had-vis}}$ p_{T} and number of associated tracks [136].

All of the above uncertainties on the different hard objects are propagated through the $\vec{E}_{\mathrm{T}}^{\mathrm{miss}}$ calculation. Additional uncertainties associated with the scale and resolution of the soft term of the $\vec{E}_{\mathrm{T}}^{\mathrm{miss}}$ [145] are also considered.

The luminosity uncertainty has been considered only for the samples whose normalisations have not been determined in data (diboson, $t\bar{t} + V$, $Z \to \ell\ell$, non-$H \to \tau\tau$ Higgs). The size of this uncertainty in the combined 2015-2018 dataset is 1.7% [154, 155].

6.2 Background theoretical uncertainties

Theoretical uncertainties are considered for the two main background contributions to this analysis: Z + jets and $t\bar{t}$. The normalisation of these backgrounds is determined in the fit to the data in the signal and control regions (see Section 7). The theoretical uncertainties on Z + jets and $t\bar{t}$ are therefore parameterised to account for the migration across the analysis regions and to account for their impact on the $m_{\tau\tau}^{\mathrm{MMC}}$ templates in each region.

For Z + jets, uncertainties have been considered for renormalisation (μ_{r}), factorisation (μ_{f}) and resummation scale (μ_{qsf}) variations, for the jet-to-parton matching scheme ($CKKW$), for variations in the choice of α_S value, and for the choice of PDFs. Uncertainties from missing higher orders were evaluated [156] using seven variations of the QCD μ_{r} and μ_{f} scales in the matrix elements by factors of 0.5 and 2, avoiding variations in opposite directions. Uncertainties in the nominal PDF set were evaluated using one hundred replica variations. The effect of the uncertainty in the strong coupling constant α_{s} was assessed by variations of ± 0.001. The resummation scale variations uncertainties have been estimated using truth-level parameterisations derived from samples with μ_{qsf} varied by 2 and 1/2 with respect to the nominal. Similarly, the jet-to-parton matching uncertainties have been estimated using truth-level parameterisations derived from samples with $CKKW$ parameter set to 15 GeV and 30 GeV, compared to the nominal value of 20 GeV.

For $t\bar{t}$, uncertainties have been considered for the choice of the matrix element and parton shower generators, the initial and final state radiation model (ISR and FSR respectively), and the PDFs. The uncertainty due to ISR was estimated by simultaneously varying the h_{damp} parameter and the μ_{r} and μ_{f} scales, and

propagating the α_s uncertainties through the Var3c parameter of the A14 tune as described in Ref. [157]. The impact of FSR was evaluated by varying the μ_r scale for emissions from the parton shower up or down by a factor two. The impact of using a different matrix element was evaluated by comparing the nominal $t\bar{t}$ sample with another event sample produced using MadGraph5_aMC@NLO 2.6.0 instead of Powheg Box v2 and keeping the same parton shower model. The impact of using a different parton shower and hadronisation model was evaluated by comparing the nominal $t\bar{t}$ sample with another event sample which instead of Pythia 8 was interfaced with Herwig 7.04 [158, 159], using the H7UE set of tuned parameters [159] and the MMHT2014lo PDF set [160].

The NNPDF3.0lo replicas were used to evaluate the PDF uncertainties for the nominal PDF. For both Z+jets and $t\bar{t}$, the central value of the PDF was additionally compared with the central values of the CT14nnlo [161] and MMHT2014nnlo [160] PDF sets.

Due to the large acceptance of Z+jets in the most sensitive regions of the analysis, compared to the contribution from $t\bar{t}$ background events, Z+jets theoretical uncertainties have a larger impact on this measurement. This represents a sub-leading contribution, compared to signal theoretical uncertainties and experimental uncertainties.

For renormalisation and factorisation scale variations and PDF uncertainties, the impact on the extrapolation factor between each SR and its corresponding $Z \to \ell\ell$ control region, and on the shape of the $m_{\tau\tau}^{\text{MMC}}$ distribution, are treated as uncorrelated across the different categories.

6.3 Signal theoretical uncertainties

Signal theoretical uncertainties are the dominant source of uncertainty for this analysis. For each signal process, several sources of uncertainties are considered, including the uncertainty in the inclusive cross-section (evaluated only for the total cross-section measurement) and the migration uncertainties among the STXS bins. These uncertainties can affect signal acceptance in the various SRs as well as the $m_{\tau\tau}^{\text{MMC}}$ shape. For all production modes, uncertainties are estimated for PDF and α_s, for parton shower and hadronisation model, and missing higher orders in the matrix element calculation. PDF and α_s uncertainties were estimated using the PDF4LHC15nlo set of eigenvectors. The impact of using a different parton shower and hadronisation model is evaluated by comparing the nominal sample with another event sample which instead of Pythia 8 is interfaced with Herwig 7 [158, 159]. The effects on the signal expectations are treated uncorrelated between each production mode and the comparison leads to the largest uncertainty on the $pp \to H \to \tau\tau$ cross-section measurement (see Fig. 7). Uncertainties from missing higher orders are calculated following the methodology outlined in Refs. [27, 162] and are determined as follows.

For the ggF process, fourteen main sources of uncertainties have been considered: four uncertainties related to jet multiplicity due to missing high-order corrections, estimated using the approach described in Refs. [27, 163]; three uncertainties which parameterize the modelling uncertainties on the Higgs boson p_T and the 0-jet bin, one which encapsulates the treatment of the top-quark mass in the loop corrections; two uncertainties account for modelling of ggF events in the VBF phase space (derived from the study of the selection of exactly two or at least three jets), derived using the method described in Ref. [164]; finally, three sources taking into account di-jet mass migrations across the STXS bin boundaries. An additional shape uncertainty was considered for ggF events in the VBF and VH enriched categories to take into account uncertainties related to missing higher order calculations for events with large jet multiplicities. The fiducial requirements for the VH and particularly for the VBF categories can enhance the sensitivity to

this effect. This uncertainty has been estimated through a comparison of the nominal POWHEG prediction with MADGRAPH5_AMC@NLO samples using FxFx prescriptions [165] to merge the jet multiplicities.

For the VBF and VH processes, ten uncertainties related to the STXS categorisation have been considered: one related to the inclusive cross-section, one related to the two jet requirement, one related to the Higgs boson p_{T} cut at 200 GeV, one related to the balance of the Higgs boson and the di-jet system in events with two or three jets, and six uncertainties taking into account di-jet mass migrations across the STXS bin boundaries.

For the $t\bar{t}H$ process, six other uncertainties are included: one related to the inclusive cross-section, and five migration uncertainties related to Higgs boson p_{T} boundaries in the STXS scheme.

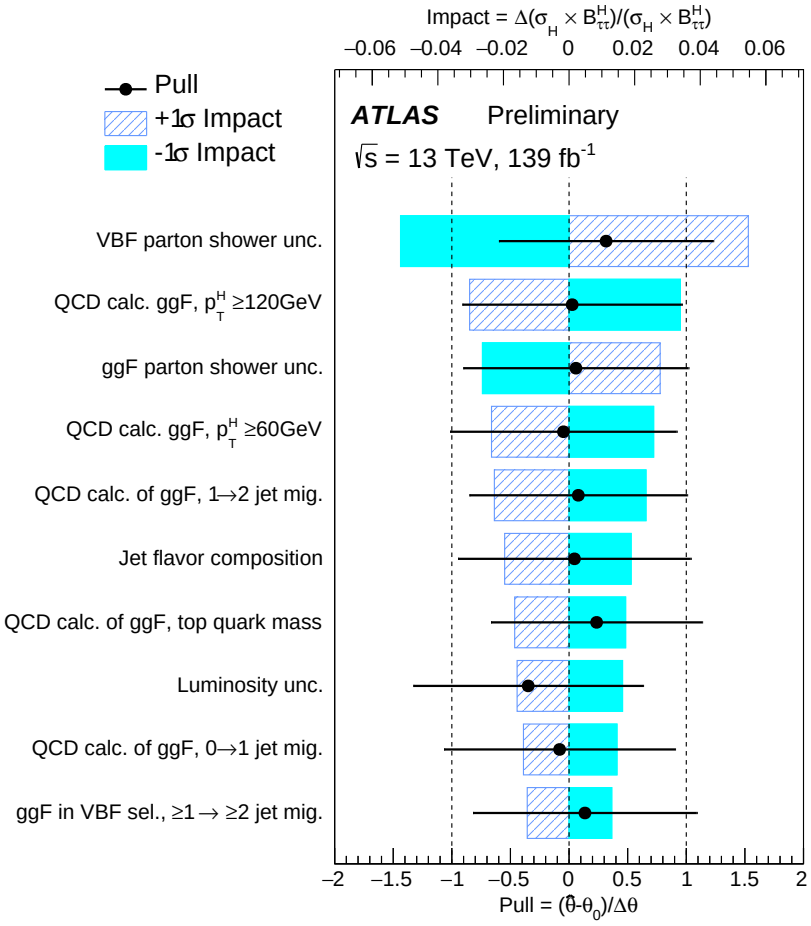

Figure 7: Fractional impact of nuisance parameters in the $pp \to H \to \tau\tau$ cross-section measurement. The ten nuisance parameters with the largest impact are shown in decreasing order. For each nuisance parameter, the dashed (light blue) band shows the fractional impact of a change of one positive (negative) standard deviation. The deviation of each nuisance parameter from their original value is indicated by the black dot and the additional constraint provided by the statistical analysis by the black line.

7 Statistical analysis

A statistical analysis of the collected data is performed to measure the $H \to \tau\tau$ cross-sections. The procedure relies on a likelihood function constructed as the product of Poisson probability terms over the bins of the input distributions, with parameters of interest (POIs) estimated by maximising the likelihood. The likelihood function comprises 32 signal regions and 36 control regions. In each signal region, Poisson terms describe the expected event counts in each bin of the $m_{\tau\tau}^{\text{MMC}}$ distribution while in each control region a single Poisson term describes the total expected event yield in that region. Figure 8 illustrates the usage of the signal and control regions in the construction of the likelihood function.

The normalisation of the $Z \to \tau\tau$ background is left as a freely-floating parameter in the fit in several regions. Each signal region in the boost, VBF and V(had)H categories is paired to an associated embedded $Z \to \ell\ell$ control region and both share a common $Z \to \tau\tau$ normalisation factor. Additionally, a common $Z \to \tau\tau$ normalisation factor is shared between the ttH_0 and ttH_1 signal regions. In total, 31 floating normalisation factors are defined to control the yields of the $Z \to \tau\tau$ background in the signal regions. The normalisation of the Top processes is also allowed to float freely with six normalisation factors defined for boost, VBF, and V(had)H signal regions in the $\tau_e\tau_\mu$ and $\tau_{\text{lep}}\tau_{\text{had}}$ channels separately and one for the ttH categories in the $\tau_{\text{had}}\tau_{\text{had}}$ channel. The other backgrounds are normalised to their expected cross-section at the luminosity of the recorded data.

In the signal regions, a smoothing procedure is applied to remove potentially large local fluctuations in the $m_{\tau\tau}^{\text{MMC}}$ caused by the limited size of the MC samples used to build the templates.

The uncertainties affecting the model (see Section 6) are constrained by Gaussian probability terms and are treated as nuisance parameters.

The discriminant $m_{\tau\tau}^{\text{MMC}}$ distributions in each SR are binned in a way that maximise the significance of each targeted signal production mode taking into account the full uncertainties. Effectively, this leads to a fine binning near the resonant $Z \to \tau\tau$ peak with coarser binning further away from it.

Three different measurements are performed. They include the branching ratio of $H \to \tau\tau$ and are performed with true Higgs boson rapidity $|y_H| < 2.5$. They differ by the definition of the POIs (see also Fig. 1):

1. *Total Cross-section*: a single POI, corresponding to the total Higgs boson cross-section, is estimated by the fit. In the likelihood function, the signal yields in each category are parameterised as the product of the total cross-section, the luminosity and the efficiency (including the acceptance of the ATLAS detector) of the selection for a SM Higgs boson with a mass of 125.09 GeV. In this measurement, the relative contributions to the total cross-section from the various production modes are fixed to the SM predictions.

2. *Cross-sections per production mode*: 4 POIs, corresponding to the cross sections of the four dominant production modes (ggF, VBF, VH, $t\bar{t}H$) of the Higgs boson, are estimated by the fit. In this configuration, the event yields in the likelihood function are the sum of those from each individual production mode, parameterised as a function of the POI in a similar way as for the first measurement.

3. *Reduced Simplified Template Cross-Sections*: nine POIs, corresponding to the cross sections of merged bins of the STXS *stage 1.2* framework shown in Fig. 2, to which this analysis is sensitive, are determined by the fit. The cross sections for $t\bar{t}H$ production and for VBF + $qq \to V(\to qq)H$

production are measured. The latter is measured with particle-level dijet mass between 60 GeV and 120 GeV and above 350 GeV. In addition, the cross section of ggF production is measured in six bins of the phase space. One of them is a combination of two bins in the *stage 1.2* prescription: events with one jet and intermediate $p_{\mathrm{T}}(H)$ (60 to 120 GeV) are measured together with events with two or more jets, low m_{jj} (< 350 GeV) and the same intermediate $p_{\mathrm{T}}(H)$.

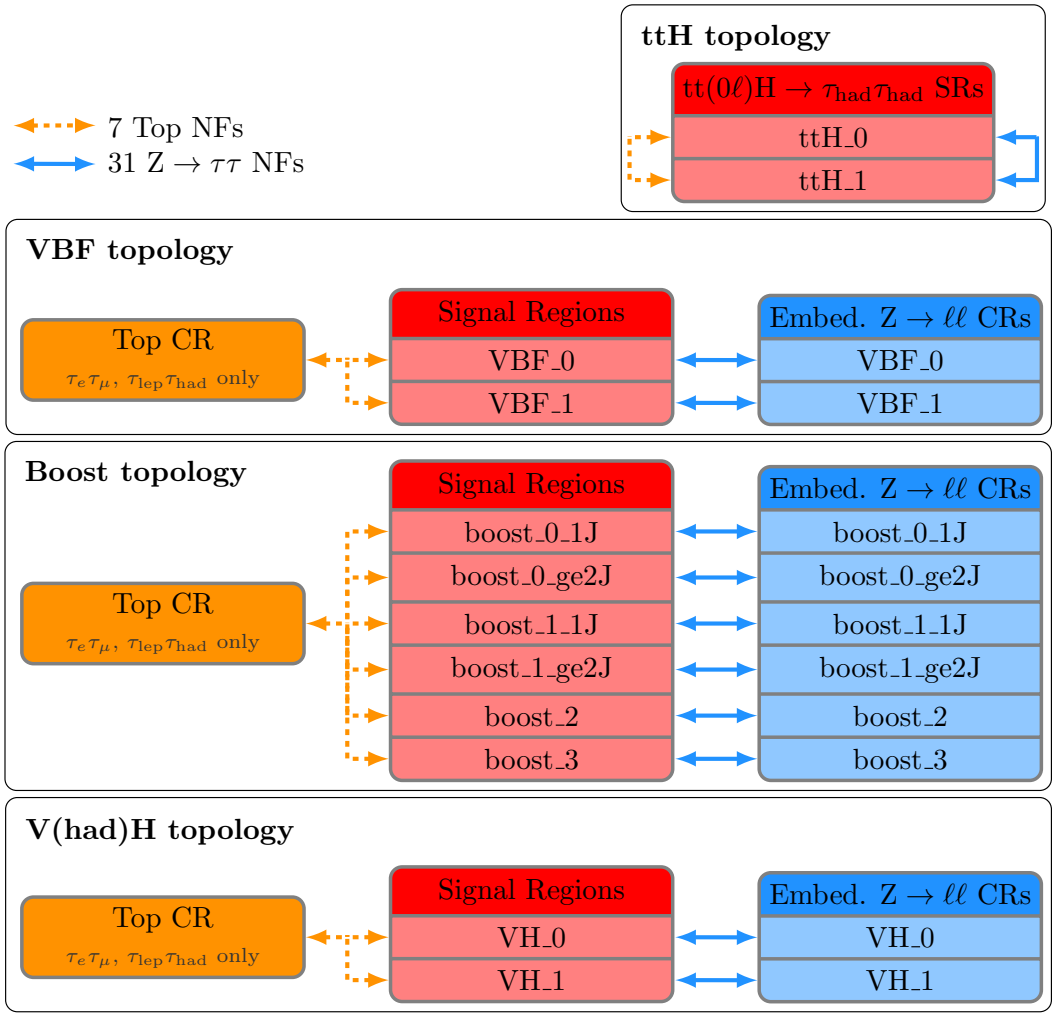

Figure 8: Graphical representation of the regions considered in the likelihood function and the normalisation factors (NFs) defined in the analysis. The four unfilled black boxes represent the four main topologies targeted in this measurement. Within each unfilled black box, the dark filled colored boxes represent from left to right, the Top control regions, the signal regions and the $Z \to \ell\ell$ control regions. When applicable the sub-categories are represented with a light filled color. Each blue solid arrowed-line represents a normalisation factor that applies to the $Z(\to \tau\tau)$ + jets process in the signal regions and to the $Z(\to \ell\ell)$ + jets process in the $Z \to \ell\ell$ control regions. Each orange dashed arrowed-line represents a normalisation factor that applies to the Top process in the signal regions and to the Top process in the Top control regions. The arrow ends of each line indicate which regions each normalisation factor connects to each other. In the likelihood function, there are signal regions and $Z \to \ell\ell$ control region for each final state in the VBF, Boost and V(had)H topolopies. Therefore the ten signal regions and $Z \to \ell\ell$ control regions are repeated three times. The Top control regions are only used in the $\tau_e\tau_\mu$ and $\tau_{\mathrm{lep}}\tau_{\mathrm{had}}$ final states. Additionally only one Top control region is considered by topology.

8 Results

The results of the statistical analysis (see Section 7) performed for the total cross-section measurement are presented in Figs. 9 to 12. The observed event yields and predictions as computed by the fit in the signal regions of the analysis are reported in Tables 7 to 12. An excellent agreement is observed between the data and the expectations. All measurements include the branching ratio of $H \rightarrow \tau\tau$ and are performed with true Higgs boson rapidity $|y_H| < 2.5$.

The total $pp \rightarrow H \rightarrow \tau\tau$ cross-section is measured to be $2.90 \pm 0.21\,(\text{stat})\,^{+0.37}_{-0.32}\,(\text{syst})$ pb in agreement with the SM predictions. The result of the measurement is compatible with the SM value of 3.15 ± 0.09 pb with a p-value of 52%.

The measurement is also performed in the $\tau_{\text{had}}\tau_{\text{had}}$, $\tau_{\text{lep}}\tau_{\text{had}}$ and $\tau_e\tau_\mu$ final states separately and in the boost, VBF, V(had)H and tt$(0\ell)H \rightarrow \tau_{\text{had}}\tau_{\text{had}}$ categories. The results are illustrated in Fig. 13. The compatibility of the measurement is 27% across τ lepton decay modes and 81% across kinematic categories.

The same dataset is subsequently used to measure the production cross-section for the Higgs boson in the four dominant production mechanisms. The results are illustrated in Fig. 14 (a) and reported in Table 13 with a breakdown of the uncertainties. They are all consistent with the SM predictions, with an overall compatibility of 88 %. The measurement establishes the observation of the VBF production of the Higgs boson in the di-τ decay channel with an observed (expected) significance of 5.3 (6.2) σ.

The VBF production cross-section is determined with the highest precision. It is measured with a value of $0.196\,^{+0.028}_{-0.027}\,(\text{stat})\,^{+0.032}_{-0.025}\,(\text{syst})$ pb. The second most precisely measured cross-section is that of ggF, $2.7 \pm 0.4\,(\text{stat})\,^{+0.9}_{-0.6}\,(\text{syst})$ pb, corresponding to an observed (expected) significance of 3.9 (4.6) σ. The VH and $t\bar{t}H$ production modes are determined with a lower precision. The measured VH cross-section is $0.11 \pm 0.06\ (\text{stat}) \pm 0.04\,(\text{syst})$ pb while the $t\bar{t}H$ one is $0.048\,^{+0.033}_{-0.029}\,(\text{stat})\,^{+0.036}_{-0.029}\,(\text{syst})$ pb. Figure 14(b) illustrates the observed correlation between the measured cross-section parameters in the fit. The ggF cross-section exhibits an anti-correlation of 24% and 29% with the VBF and VH cross-sections respectively. This is caused by a significant contribution of ggF events to the VBF_0, VH_0 and VH_1 categories as illustrated by Fig. 2. The simultaneous measurement of the cross-sections of the four dominant production mode is compatible with the SM expectations with a p-value of 88%.

Finally the $pp \rightarrow H \rightarrow \tau\tau$ cross-sections are measured as a function of $p_{\text{T}}(H)$, $\text{N}_{\text{jets}}(p_{\text{T}} > 30\,\text{GeV})$ and m_{jj} in a reduced set of the bins of the *stage 1.2* of the STXS framework. The results, illustrated in Fig. 15(a), are reported in Table 14. They are in very good agreement with the SM expectations. The gluon-gluon fusion + $gg \rightarrow Z(\rightarrow qq)H$ production mode is measured in four $p_{\text{T}}(H)$ intervals starting at 60 GeV. For $p_{\text{T}}(H)$ values between 120 GeV and 200 GeV, the measurements are further split based on the number of jets in the event. The best precision is obtained in the $p_{\text{T}}(H)$ interval between 200 GeV and 300 GeV and in the $p_{\text{T}}(H)$ regime above 300 GeV. The cross-sections are determined with an uncertainty of 37% and 42% respectively.

The EW production mode includes the VBF and the $qq \rightarrow V(\rightarrow qq)H$ processes and is measured in m_{jj} intervals. In the interval with m_{jj} between 60 GeV and 120 GeV, the measurement reaches a precision of 63%. The EW production mode for events with m_{jj} greater than 120 GeV is measured with a precision of 26% and is the most precise cross-section determined within the simplified template cross-section framework in this paper. It exhibits an anti-correlation of approximately 40% to the cross-section for gluongluon fusion events produced in the same interval ($m_{jj} > 350$ GeV) as illustrated on Fig. 15 (b).

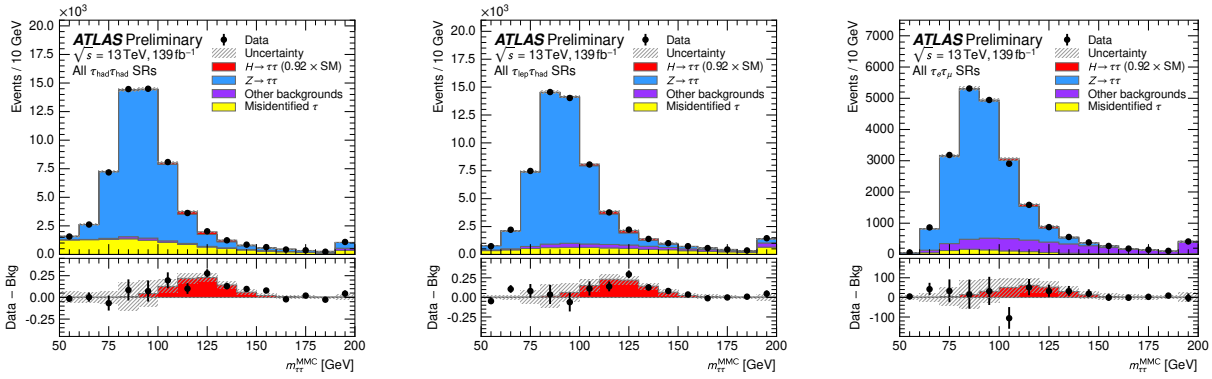

(a) $\tau_{\text{had}}\tau_{\text{had}}$ (b) $\tau_{\text{lep}}\tau_{\text{had}}$ (c) $\tau_e\tau_\mu$

Figure 9: Distribution of the reconstructed di-τ invariant mass ($m_{\tau\tau}^{\text{MMC}}$) for all events in the (a) $\tau_{\text{had}}\tau_{\text{had}}$, (b) $\tau_{\text{lep}}\tau_{\text{had}}$ and (c) $\tau_e\tau_\mu$ signal regions. The bottom panel shows the differences between observed data events and expected background events (black points). The observed Higgs-boson signal, corresponding to $(\sigma \times B)/(\sigma \times B)_{\text{SM}} = 0.92$, is shown with a filled red histogram. Entries with values above the x-axis range are shown in the last bin of each distributions. The prediction for each sample is determined from the likelihood fit performed to measure the total $pp \to H \to \tau\tau$ cross-section.

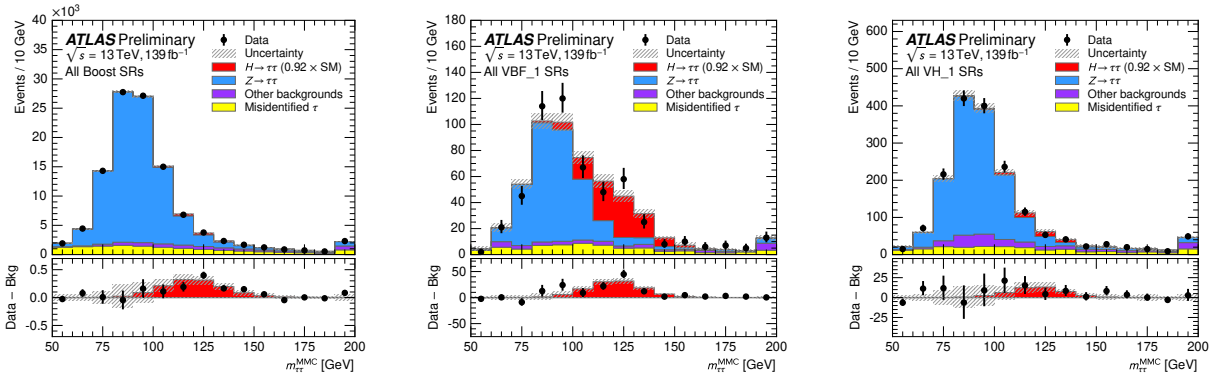

(a) boost (b) VBF_1 (c) VH_1

Figure 10: Distribution of the reconstructed di-τ invariant mass ($m_{\tau\tau}^{\text{MMC}}$) for all events in the (a) boost, (b) VBF_1 and (c) VH_1 signal regions. The bottom panel shows the differences between observed data events and expected background events (black points). The observed Higgs-boson signal, corresponding to $(\sigma \times B)/(\sigma \times B)_{\text{SM}} = 0.92$, is shown with a filled red histogram. Entries with values above the x-axis range are shown in the last bin of each distributions. The prediction for each sample is determined from the likelihood fit performed to measure the total $pp \to H \to \tau\tau$ cross-section.

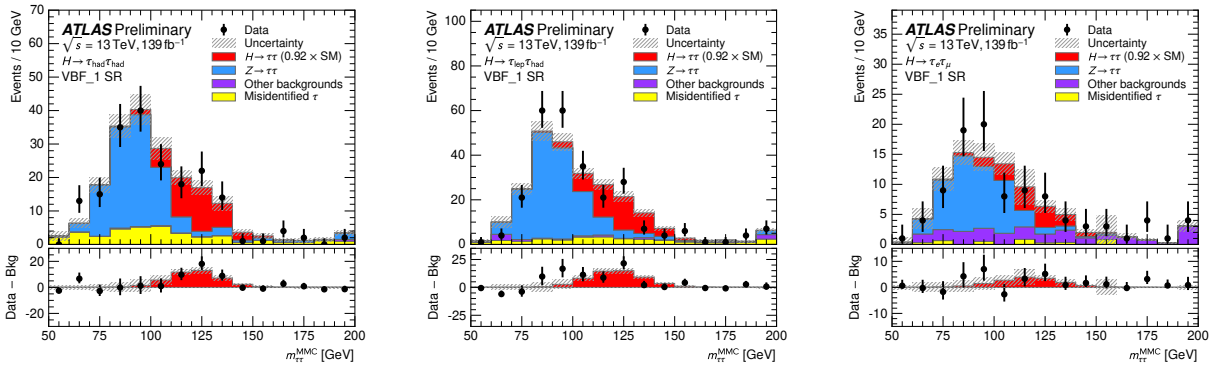

(a) $\tau_{\text{had}}\tau_{\text{had}}$ (b) $\tau_{\text{lep}}\tau_{\text{had}}$ (c) $\tau_e\tau_\mu$

Figure 11: Distribution of the reconstructed di-τ invariant mass ($m_{\tau\tau}^{\text{MMC}}$) for all events in the VBF_1 categories of (a) $\tau_{\text{had}}\tau_{\text{had}}$, (b) $\tau_{\text{lep}}\tau_{\text{had}}$ and (c) $\tau_e\tau_\mu$ signal regions. The bottom panel shows the differences between observed data events and expected background events (black points). The observed Higgs-boson signal, corresponding to $(\sigma \times B)/(\sigma \times B)_{\text{SM}} = 0.92$, is shown with a filled red histogram. Entries with values above the x-axis range are shown in the last bin of each distributions. The prediction for each sample is determined from the likelihood fit performed to measure the total $pp \rightarrow H \rightarrow \tau\tau$ cross-section.

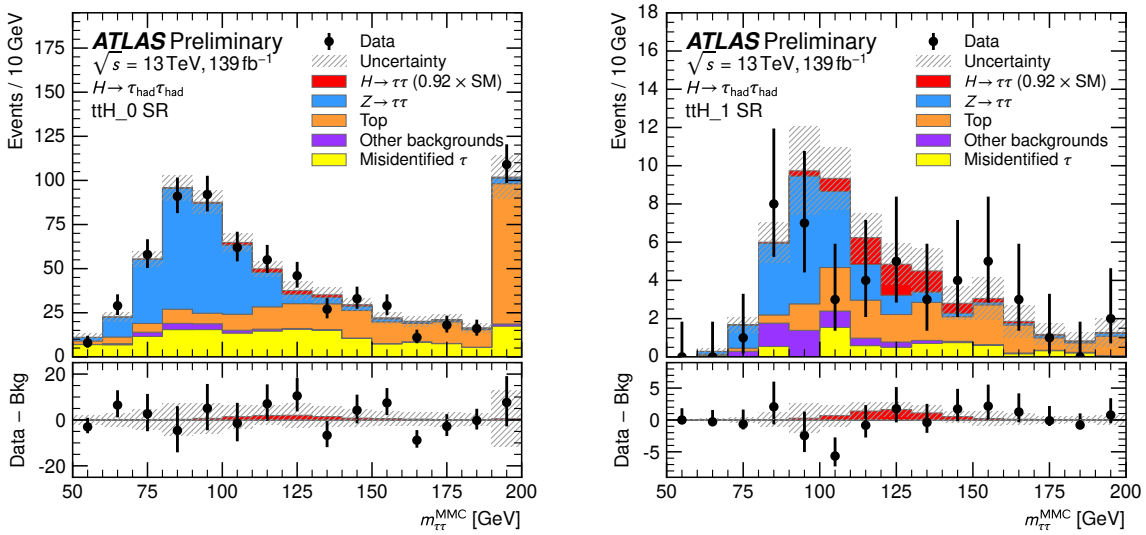

(a) ttH_0 (b) ttH_1

Figure 12: Distribution of the reconstructed di-τ invariant mass ($m_{\tau\tau}^{\text{MMC}}$) for all events in the (a) ttH_0 and (b)ttH_1 categories of the $\tau_{\text{had}}\tau_{\text{had}}$ channel. The bottom panel shows the differences between observed data events and expected background events (black points). The observed Higgs-boson signal, corresponding to $(\sigma \times B)/(\sigma \times B)_{\text{SM}} = 0.92$, is shown with a filled red histogram. Entries with values above the x-axis range are shown in the last bin of each distributions. The prediction for each sample is determined from the likelihood fit performed to measure the total $pp \rightarrow H \rightarrow \tau\tau$ cross-section.

Table 7: Observed event yields and predictions as computed by the fit in the VBF, V(had)H and tt(0ℓ)$H \to \tau_{\text{had}}\tau_{\text{had}}$ signal regions of the $\tau_{\text{had}}\tau_{\text{had}}$ channel. In the VBF and V(had)H categories, the top processes are estimated with the other backgrounds (diboson, $H \to WW^*$) by the fit. Uncertainties include statistical and systematic components.

	VBF $\tau_{\text{had}}\tau_{\text{had}}$		V(had)H $\tau_{\text{had}}\tau_{\text{had}}$		tt(0ℓ)$H \to \tau_{\text{had}}\tau_{\text{had}}$	
	VBF_0	VBF_1	VH_0	VH_1	ttH_0	ttH_1
$Z \to \tau\tau$	2058 ± 45	113.9 ± 9.4	4630 ± 75	539 ± 21	264 ± 22	19.5 ± 3.4
Fake	1037 ± 24	40.2 ± 2.7	1627 ± 37	111.7 ± 4.0	184 ± 11	6.59 ± 0.58
Top					246 ± 23	13.23 ± 5.34
Other backgrounds	57.2 ± 4.1	1.67 ± 0.11	209 ± 10	43.2 ± 2.3	8.8 ± 1.0	1.54 ± 0.10
ggF, $H \to \tau\tau$	38.3 ± 9.5	3.2 ± 1.8	72 ± 14	6.8 ± 1.7	2.0 ± 0.4	0.42 ± 0.08
VBF, $H \to \tau\tau$	72 ± 10	40.3 ± 5.1	8.1 ± 1.2	0.53 ± 0.12	0.226 ± 0.031	< 0.01
$WH, H \to \tau\tau$	1.00 ± 0.14	< 0.01	15.2 ± 2.1	9.9 ± 1.5	0.239 ± 0.033	0.034 ± 0.005
$ZH, H \to \tau\tau$	0.78 ± 0.11	< 0.01	12.4 ± 1.7	5.47 ± 0.80	0.69 ± 0.10	0.148 ± 0.021
$t\bar{t}H, H \to \tau\tau$	0.188 ± 0.026	< 0.01	0.52 ± 0.07	0.219 ± 0.031	7.0 ± 1.6	5.4 ± 1.4
Total background	3153 ± 46	155.8 ± 9.9	6466 ± 72	694 ± 22	711 ± 26	44.3 ± 5.7
Total signal	113 ± 15	43.5 ± 5.2	109 ± 16	23.0 ± 3.1	11.1 ± 1.9	6.5 ± 1.4
Total	3266 ± 45	199 ± 10	6574 ± 73	717 ± 23	722 ± 27	50.8 ± 5.8
Data	3318	197	6532	720	727	49

Table 8: Observed event yields and predictions as computed by the fit in the VBF and V(had)H signal regions of the $\tau_{\text{lep}}\tau_{\text{had}}$ channel. Uncertainties include statistical and systematic components.

	VBF $\tau_{\text{lep}}\tau_{\text{had}}$		V(had)H $\tau_{\text{lep}}\tau_{\text{had}}$	
	VBF_0	VBF_1	VH_0	VH_1
$Z \to \tau\tau$	2362 ± 55	163 ± 11	6719 ± 103	538 ± 20
Fake	613 ± 58	29.8 ± 3.1	1323 ± 96	80.6 ± 6.3
Top	104 ± 10	5.0 ± 1.2	236 ± 28	28.0 ± 3.9
Other backgrounds	139 ± 13	5.54 ± 0.99	397 ± 26	50.0 ± 1.9
ggF, $H \to \tau\tau$	71 ± 28	3.5 ± 1.2	88 ± 21	5.1 ± 2.2
VBF, $H \to \tau\tau$	84 ± 11	51.9 ± 6.5	9.3 ± 1.6	0.44 ± 0.16
$WH, H \to \tau\tau$	0.83 ± 0.12	0.0110 ± 0.0015	17.4 ± 2.4	8.1 ± 1.1
$ZH, H \to \tau\tau$	0.86 ± 0.0	< 0.01	13.4 ± 1.9	5.0 ± 0.8
$t\bar{t}H, H \to \tau\tau$	0.101 ± 0.014	< 0.01	0.35 ± 0.05	0.130 ± 0.018
Total background	3219 ± 59	203 ± 11	8675 ± 91	696 ± 21
Total signal	158 ± 31	55.4 ± 6.6	128.1 ± 22.8	18.8 ± 3.1
Total	3377 ± 53	258 ± 12	8803 ± 88	715 ± 21
Data	3402	267	8780	743

Table 9: Observed event yields and predictions as computed by the fit in the VBF and V(had)H signal regions of the $\tau_e\tau_\mu$ channel. Uncertainties include statistical and systematic components.

	VBF $\tau_e\tau_\mu$		V(had)H $\tau_e\tau_\mu$	
	VBF_0	VBF_1	VH_0	VH_1
$Z \to \tau\tau$	822 ± 27	49.5 ± 6.1	2430 ± 52	188 ± 12
Fake	89 ± 15	3.1 ± 2.3	214 ± 36	32.1 ± 9.3
Top	174 ± 14	9.8 ± 2.2	338 ± 25	35.5 ± 4.8
Other backgrounds	95.4 ± 5.3	11.9 ± 1.1	260 ± 13	27.7 ± 1.4
ggF, $H \to \tau\tau$	12.6 ± 3.2	1.04 ± 0.31	26 ± 5	1.8 ± 0.6
VBF, $H \to \tau\tau$	22.2 ± 3.0	14.3 ± 1.8	2.4 ± 0.4	0.133 ± 0.022
$WH, H \to \tau\tau$	0.207 ± 0.029	< 0.01	4.3 ± 0.7	2.4 ± 0.4
$ZH, H \to \tau\tau$	0.138 ± 0.019	< 0.01	3.6 ± 0.5	1.49 ± 0.29
$t\bar{t}H, H \to \tau\tau$	< 0.01	< 0.01	0.077 ± 0.011	0.0209 ± 0.0029
Total background	1181 ± 28	74 ± 6.8	3244 ± 49	283 ± 13
Total signal	35.3 ± 4.6	15.3 ± 1.8	36.6 ± 5.7	5.9 ± 0.9
Total	1216 ± 28	89.7 ± 6.8	3280 ± 49	289 ± 13
Data	1215	98	3277	286

Table 10: Observed event yields and predictions as computed by the fit in the Boost signal regions of the $\tau_{\text{had}}\tau_{\text{had}}$ channel. Uncertainties include statistical and systematic components.

	Boost $\tau_{\text{had}}\tau_{\text{had}}$					
$p_{\text{T}}(H)$	[100, 120]		[120, 200]		[200, 300]	[300, ∞[
$N_{\text{jets}}(p_{\text{T}} > 30\,\text{GeV})$	= 1	≥ 2	= 1	≥ 2	≥ 1	≥ 1
$Z \to \tau\tau$	5635 ± 99	2645 ± 60	11 859 ± 124	10 078 ± 118	7255 ± 88	974 ± 27
Fake	3389 ± 69	1734 ± 40	2302 ± 64	2077 ± 56	291 ± 21	54 ± 16
Other backgrounds	60.7 ± 2.3	74 ± 10	117 ± 18	250 ± 12	156.9 ± 8.6	53.1 ± 5.0
ggF, $H \to \tau\tau$	54.3 ± 9.7	23.2 ± 4.1	113 ± 21	110 ± 21	97 ± 17	30.2 ± 7.0
VBF, $H \to \tau\tau$	11.4 ± 1.7	5.8 ± 0.9	27.7 ± 4.2	24.5 ± 4.3	23.7 ± 3.5	7.3 ± 1.1
$WH, H \to \tau\tau$	2.13 ± 0.34	1.47 ± 0.21	3.8 ± 0.6	7.0 ± 1.0	4.6 ± 0.7	2.5 ± 0.4
$ZH, H \to \tau\tau$	1.37 ± 0.23	1.11 ± 0.20	2.7 ± 0.4	5.3 ± 0.7	3.7 ± 0.5	1.49 ± 0.21
$t\bar{t}H, H \to \tau\tau$	< 0.01	0.270 ± 0.038	< 0.01	1.01 ± 0.14	0.77 ± 0.11	0.35 ± 0.05
Total background	9084 ± 92	4453 ± 58	14 278 ± 112	12 405 ± 109	7702 ± 86	1080 ± 28
Total signal	69 ± 11	32.0 ± 4.7	147 ± 23	148 ± 23	130 ± 19	41.9 ± 7.3
Total	9153 ± 91	4485 ± 58	14 425 ± 111	12 553 ± 107	7832 ± 85	1122 ± 28
Data	9163	4503	14 389	12 585	7800	1124

Table 11: Observed event yields and predictions as computed by the fit in the Boost signal regions of the $\tau_{\text{lep}}\tau_{\text{had}}$ channel. Uncertainties include statistical and systematic components.

	Boost $\tau_{\text{lep}}\tau_{\text{had}}$					
$p_{\text{T}}(H)$	[100, 120]		[120, 200]		[200, 300]	[300, ∞[
$N_{\text{jets}}(p_{\text{T}} > 30\,\text{GeV})$	= 1	≥ 2	= 1	≥ 2	≥ 1	≥ 1
$Z \to \tau\tau$	5588 ± 87	3228 ± 61	10 920 ± 115	9536 ± 110	7188 ± 85	2415 ± 43
Fake	1132 ± 41	830 ± 30	1320 ± 52	1434 ± 55	539 ± 24	139.5 ± 9.3
Top	68.0 ± 8.8	115 ± 14	79.3 ± 8.7	313 ± 24	128.2 ± 9.2	52.9 ± 6.5
Other backgrounds	217 ± 31	175 ± 10	372 ± 34	446 ± 24	301 ± 16	164 ± 5.7
ggF, $H \to \tau\tau$	45 ± 12	45 ± 16	99 ± 20	124 ± 30	91 ± 24	33.7 ± 9.0
VBF, $H \to \tau\tau$	12.1 ± 1.9	7.2 ± 1.0	26.9 ± 4.0	23.5 ± 3.7	21.5 ± 3.2	8.6 ± 1.4
$WH, H \to \tau\tau$	1.73 ± 0.33	2.17 ± 0.41	3.49 ± 0.53	6.50 ± 0.92	4.41 ± 0.64	3.33 ± 0.48
$ZH, H \to \tau\tau$	1.17 ± 0.21	1.29 ± 0.20	2.35 ± 0.33	4.67 ± 0.65	3.02 ± 0.42	1.76 ± 0.24
$t\bar{t}H, H \to \tau\tau$	< 0.01	0.114 ± 0.016	< 0.01	0.55 ± 0.08	0.35 ± 0.05	0.222 ± 0.031
Total background	7005 ± 82	4349 ± 62	12 690 ± 108	11 729 ± 104	8155 ± 82	2772 ± 45
Total signal	60 ± 13	56 ± 16	132 ± 22	159 ± 31	121 ± 25	47.7 ± 9.3
Total	7065 ± 81	4405 ± 61	12 823 ± 106	11 888 ± 101	8276 ± 80	2819 ± 45
Data	7094	4374	12 779	11 886	8236	2848

Table 12: Observed event yields and predictions as computed by the fit in the Boost signal regions of the $\tau_e\tau_\mu$ channel. Uncertainties include statistical and systematic components.

	Boost $\tau_e\tau_\mu$					
$p_{\text{T}}(H)$	[100, 120]		[120, 200]		[200, 300]	[300, ∞[
$N_{\text{jets}}(p_{\text{T}} > 30\,\text{GeV})$	= 1	≥ 2	= 1	≥ 2	≥ 1	≥ 1
$Z \to \tau\tau$	2637 ± 56	1523 ± 38	3901 ± 63	3446 ± 61	1730 ± 35	465 ± 19
Fake	101 ± 23	85 ± 16	119 ± 30	180 ± 35	89 ± 19	35.6 ± 7.1
Top	108 ± 11	182 ± 18	160 ± 13	569 ± 41	247 ± 14	95.9 ± 9.4
Other backgrounds	117.8 ± 8.0	100.4 ± 9.1	273 ± 11	326 ± 14	291.2 ± 7.9	171.5 ± 5.2
ggF, $H \to \tau\tau$	16.6 ± 3.2	11.1 ± 2.0	34.9 ± 6.6	37.0 ± 7.1	25.6 ± 4.6	8.8 ± 2.2
VBF, $H \to \tau\tau$	3.45 ± 0.51	2.16 ± 0.32	8.8 ± 1.3	7.8 ± 1.2	6.2 ± 0.9	2.1 ± 0.4
$WH, H \to \tau\tau$	0.44 ± 0.06	0.57 ± 0.08	1.35 ± 0.25	2.2 ± 0.4	1.29 ± 0.18	0.87 ± 0.14
$ZH, H \to \tau\tau$	0.29 ± 0.04	0.33 ± 0.05	0.73 ± 0.10	1.57 ± 0.22	0.85 ± 0.12	0.41 ± 0.06
$t\bar{t}H, H \to \tau\tau$	< 0.01	0.029 ± 0.004	< 0.01	0.203 ± 0.028	0.079 ± 0.011	0.07 ± 0.01
Total background	2964 ± 52	1891 ± 37	4453 ± 60	4522 ± 59	2357 ± 37	768 ± 20
Total signal	20.8 ± 3.5	14.2 ± 2.2	45.8 ± 7.3	49.0 ± 7.6	34.1 ± 5.0	12.2 ± 2.3
Total	2984 ± 52	1905 ± 37	4499 ± 60	4571 ± 58	2391 ± 37	780 ± 20
Data	2973	1877	4458	4594	2325	743

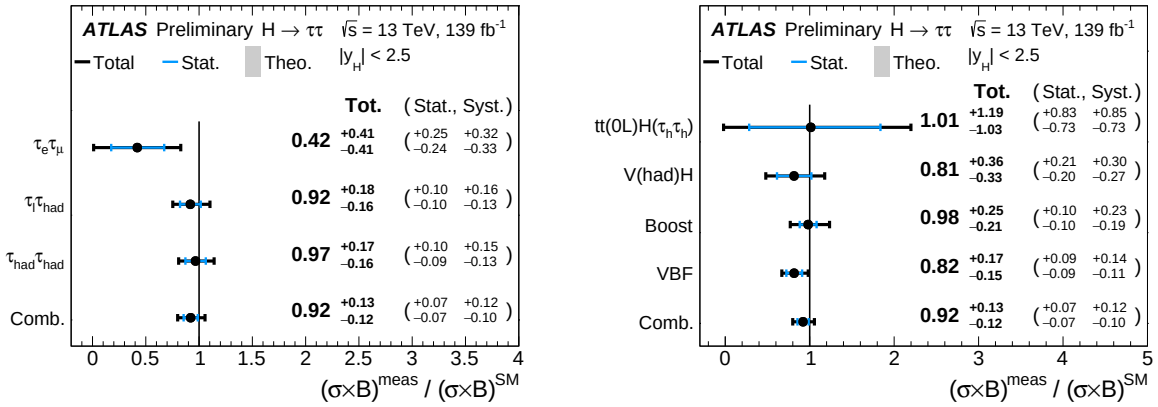

(a) (b)

Figure 13: The measured values for $\sigma_H \times B(H \rightarrow \tau\tau)$ relative to the SM expectations when only the data of (a) individual channels or (b) individual categories are used. The total $\pm 1\,\sigma$ uncertainty in the measurement is indicated by the black error bars, with the individual contribution from the statistical uncertainty in blue.

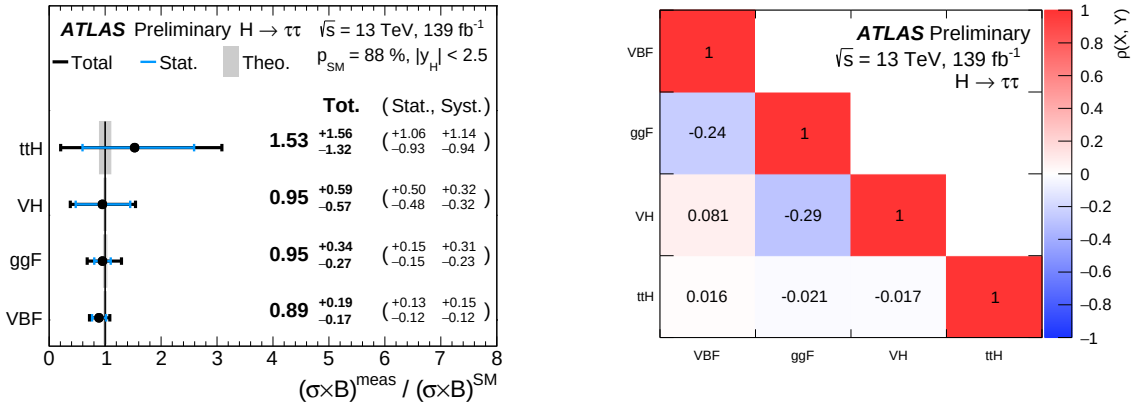

(a) (b)

Figure 14: (a) The measured values for $\sigma_H \times B(H \rightarrow \tau\tau)$ relative to the SM expectations in the four dominant production modes. The total $\pm 1\,\sigma$ uncertainty in the measurement is indicated by the black error bars, with the individual contribution from the statistical uncertainty in blue. (b) The measured correlations between each parameter of interest in the measurement of the cross-sections per production mode.

Table 13: Best-fit values and uncertainties for the total $pp \to H \to \tau\tau$ cross-section and the measurement in the four dominant production modes. All measurements include the branching ratio of $H \to \tau\tau$ and are performed with true Higgs boson rapidity $|y_H| < 2.5$. The SM predictions for each region, computed using the inclusive cross-section calculations and the simulated event samples are also shown. The contributions to the total uncertainty in the measurements from statistical (Stat. unc.) or systematic uncertainties (Syst. unc.) in the signal prediction (Th. sig.), background prediction (Th. bkg.), and in experimental performance (Exp.) are given separately.

Production Mode	SM prediction	Result	Stat. unc.	Syst. unc. [pb]		
	[pb]	[pb]	[pb]	Th. sig.	Th. bkg.	Exp.
$t\bar{t}H$	0.031 ± 0.003	0.048 ± 0.045	± 0.027	± 0.011	± 0.027	± 0.018
VH	0.118 ± 0.003	0.11 ± 0.04	± 0.02	± 0.02	± 0.01	± 0.02
ggF	2.8 ± 0.1	2.7 ± 0.9	± 0.4	± 0.6	± 0.1	± 0.5
VBF	0.22 ± 0.01	0.196 ± 0.040	± 0.026	± 0.024	± 0.005	± 0.016
$pp \to H$	3.15 ± 0.09	2.90 ± 0.40	± 0.22	± 0.26	± 0.06	± 0.22

Table 14: Best-fit values and uncertainties for the $H \to \tau\tau$ cross-sections, in the reduced *stage 1.2* STXS scheme described in the text. The EWK production mode includes vector-boson fusion and $qq \to V(\to qq)H$ processes. All measurements include the branching ratio of $H \to \tau\tau$ and are performed with true Higgs boson rapidity $|y_H| < 2.5$. The SM predictions for each region, computed using the inclusive cross-section calculations and the simulated event samples are also shown. The contributions to the total uncertainty in the measurements from statistical (Stat. unc.) or systematic uncertainties (Syst. unc.) in the signal prediction (Th. sig.), background prediction (Th. bkg.), and in experimental performance (Exp.) are given separately. The spades symbol (♠) indicates that the criteria on m_{jj} only apply to events with at least two reconstructed jets.

STXS bin				SM prediction	Result	Stat. unc.	Syst. unc. [pb]		
Process	m_{jj} [GeV]	$p_T(H)$ [GeV]	N_{jets}	[pb]	[pb]	[pb]	Th. sig.	Th. bkg.	Exp.
ggF + $gg \to Z(\to qq)H$	[0, 350]♠	[60, 120]	≥ 1	0.39 ± 0.06	0.17 ± 0.39	± 0.22	± 0.06	± 0.15	± 0.29
		[120, 200]	$= 1$	0.047 ± 0.011	0.018 ± 0.030	± 0.018	± 0.004	± 0.004	± 0.019
	[0, 350]	[120, 200]	≥ 2	0.059 ± 0.020	0.036 ± 0.039	± 0.027	± 0.009	± 0.009	± 0.025
		[200, 300]	≥ 0	0.030 ± 0.009	0.031 ± 0.011	± 0.009	± 0.003	± 0.001	± 0.006
		[300, ∞[	≥ 0	0.008 ± 0.003	0.009 ± 0.004	± 0.003	± 0.001	± 0.000	± 0.001
	[350, ∞[	[0, 200]	≥ 2	0.055 ± 0.013	0.14 ± 0.11	± 0.05	± 0.06	± 0.01	± 0.07
EWK	[60, 120]		≥ 2	0.033 ± 0.001	0.031 ± 0.020	± 0.017	± 0.003	± 0.001	± 0.010
	[350, ∞[		≥ 2	0.090 ± 0.002	0.071 ± 0.017	± 0.014	± 0.010	± 0.002	± 0.006
$t\bar{t}H$				0.031 ± 0.003	0.047 ± 0.046	± 0.032	± 0.011	± 0.027	± 0.018

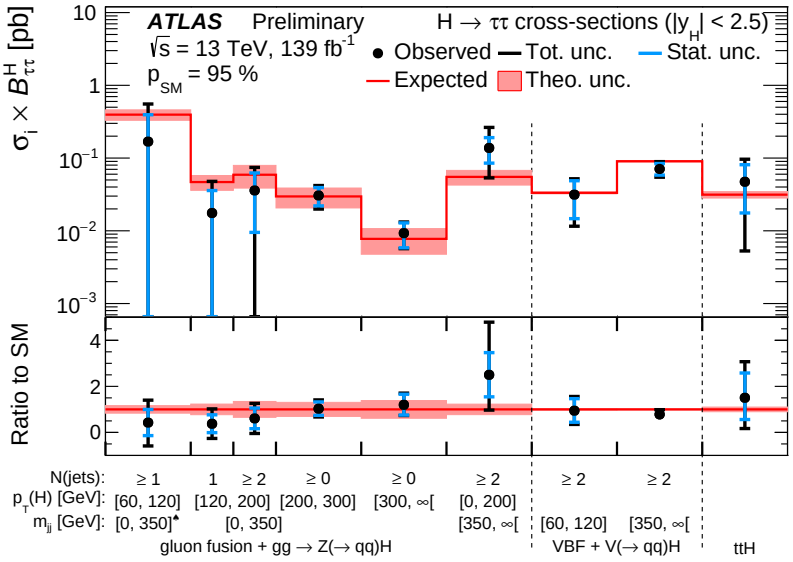

(a)

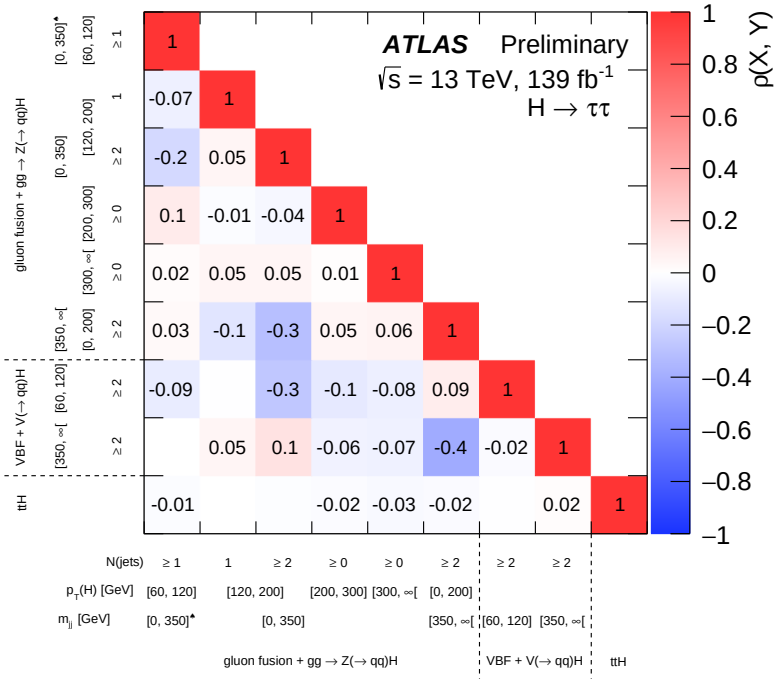

(b)

Figure 15: (a) The measured values for $\sigma_H \times B(H \rightarrow \tau\tau)$ relative to the SM expectations in the nine fiducial volumes defined in the STXS measurement. Also shown is the result from the combined fit. The total $\pm 1\,\sigma$ uncertainty in the measurement is indicated by the black error bars, with the individual contribution from the statistical uncertainty in blue. (b) The measured correlations between each pair parameter of interest in the STXS measurement. The spades symbol (♠) indicates that the criteria on m_{jj} only apply to events with at least two reconstructed jets.

9 Conclusion

Measurements of the Standard Model Higgs boson decaying into a pair of τ leptons are presented. The measurements use data collected by the ATLAS experiment in proton-proton collisions from Run 2 of the LHC. The data correspond to an integrated luminosity of 139 fb^{-1}.

All measurements include the branching ratio of $H \to \tau\tau$ and are performed with true Higgs boson rapidity $|y_H| < 2.5$. The total cross-section in the $H \to \tau\tau$ decay channel is measured to be 2.90 ± 0.21 (stat) $^{+0.37}_{-0.32}$(syst) pb, in excellent agreement with the SM predictions. The observed (expected) precision on the $pp \to H \to \tau\tau$ cross-section determination improved from $^{+28}_{-25}$ % ($^{+27}_{-24}$ %) in the measurement performed in Ref. [22] to 12.8% (12.5%) in this work. In particular the impact of the systematic uncertainties was reduced by approximately a factor two from 21.5% to 11.1%.

Total cross-sections are determined separately for the four dominant production modes: 2.7 ± 0.4 (stat) $^{+0.9}_{-0.6}$ (syst) pb for the gluon-gluon fusion, $0.196\,^{+0.028}_{-0.027}$ (stat) $^{+0.032}_{-0.025}$ (syst) pb for the vector-boson fusion, 0.11 ± 0.06 (stat) $\pm$ 0.04 (syst) pb for the production associated with a vector boson and $0.048\,^{+0.033}_{-0.029}$ (stat) $^{+0.036}_{-0.029}$ (syst) pb for the production associated with a pair of top quarks.

Differential measurements using the simplified template cross-section framework are also performed. Cross-sections of the production of a Higgs boson decaying into τ leptons are measured as a function of the Higgs boson transverse momentum, the number of jets produced in association with the Higgs boson and the invariant mass of the two leading jets when applicable. The measurements reach a precision of 24% for the EW production with two jets of invariant mass greater than 350 GeV. The ggF production is measured with a precision of 36% and 40% when the Higgs boson transverse momentum is between 200 and 300 GeV and above 300 GeV respectively. All measurements are in agreement with the Standard Model predictions.

Appendix

Figs. 16 to 21 show all distributions that enter the likelihood fit with the best-fit parameters of the 1 POI setup.

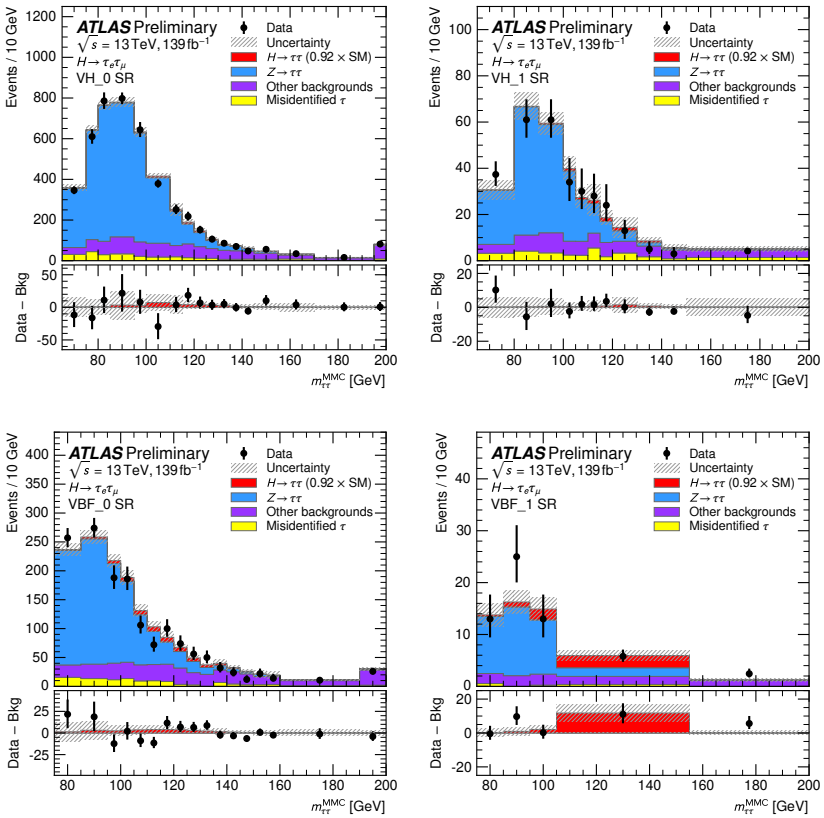

Figure 16: Distribution of the reconstructed di-τ invariant mass ($m_{\tau\tau}^{\mathrm{MMC}}$) for all events in the V(had)H and VBF categories of the $\tau_e\tau_{mu}$ channel. The bottom panel shows the differences between observed data events and expected background events (black points). The observed Higgs-boson signal, corresponding to $(\sigma \times B)/(\sigma \times B)_{\mathrm{SM}} = 0.92$, is shown with a filled red histogram. Entries with values above the x-axis range are shown in the last bin of each distributions. The prediction for each sample is determined from the likelihood fit performed to measure the total $pp \rightarrow H \rightarrow \tau\tau$ cross-section.

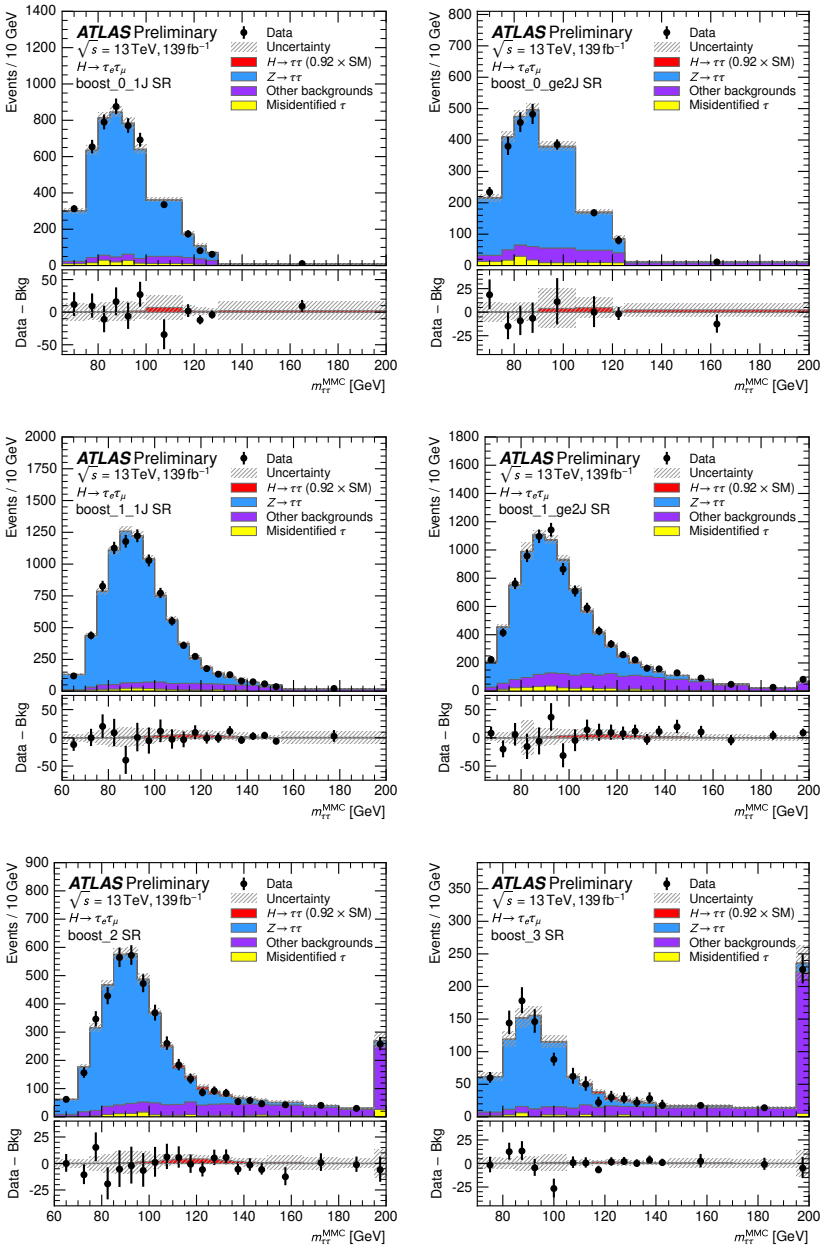

Figure 17: Distribution of the reconstructed di-τ invariant mass ($m_{\tau\tau}^{\mathrm{MMC}}$) for all events in the boost categories of the $\tau_e\tau_\mu$ channel. The bottom panel shows the differences between observed data events and expected background events (black points). The observed Higgs-boson signal, corresponding to $(\sigma \times B)/(\sigma \times B)_{\mathrm{SM}} = 0.92$, is shown with a filled red histogram. Entries with values above the x-axis range are shown in the last bin of each distributions. The prediction for each sample is determined from the likelihood fit performed to measure the total $pp \rightarrow H \rightarrow \tau\tau$ cross-section.

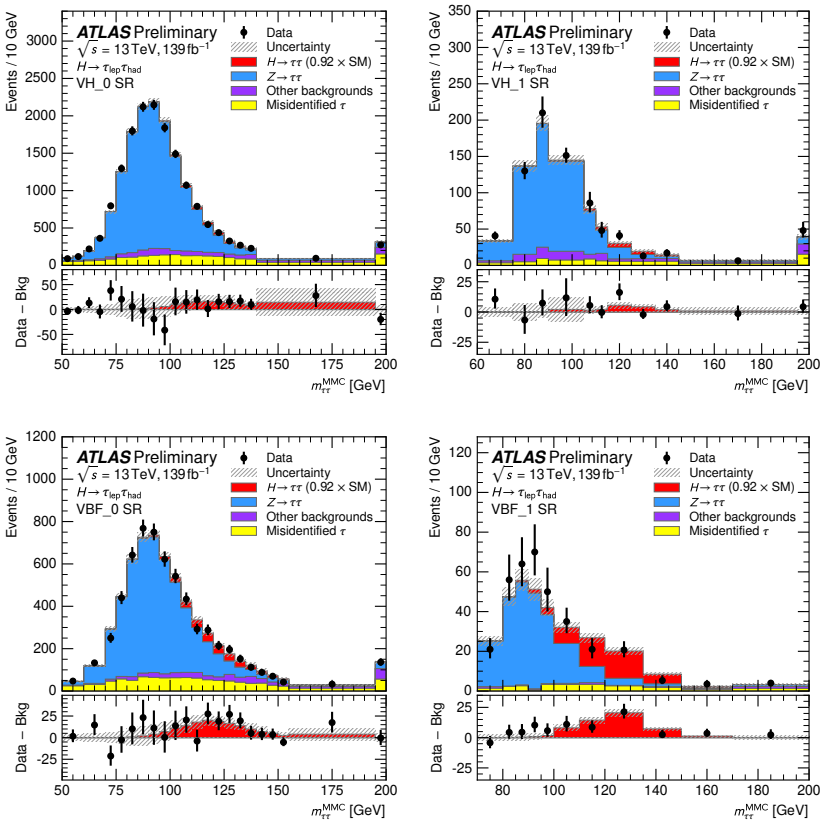

Figure 18: Distribution of the reconstructed di-τ invariant mass ($m_{\tau\tau}^{\mathrm{MMC}}$) for all events in the V(had)H and VBF categories of the $\tau_{\mathrm{lep}}\tau_{\mathrm{had}}$ channel. The bottom panel shows the differences between observed data events and expected background events (black points). The observed Higgs-boson signal, corresponding to $(\sigma \times B)/(\sigma \times B)_{\mathrm{SM}} = 0.92$, is shown with a filled red histogram. Entries with values above the x-axis range are shown in the last bin of each distributions. The prediction for each sample is determined from the likelihood fit performed to measure the total $pp \rightarrow H \rightarrow \tau\tau$ cross-section.

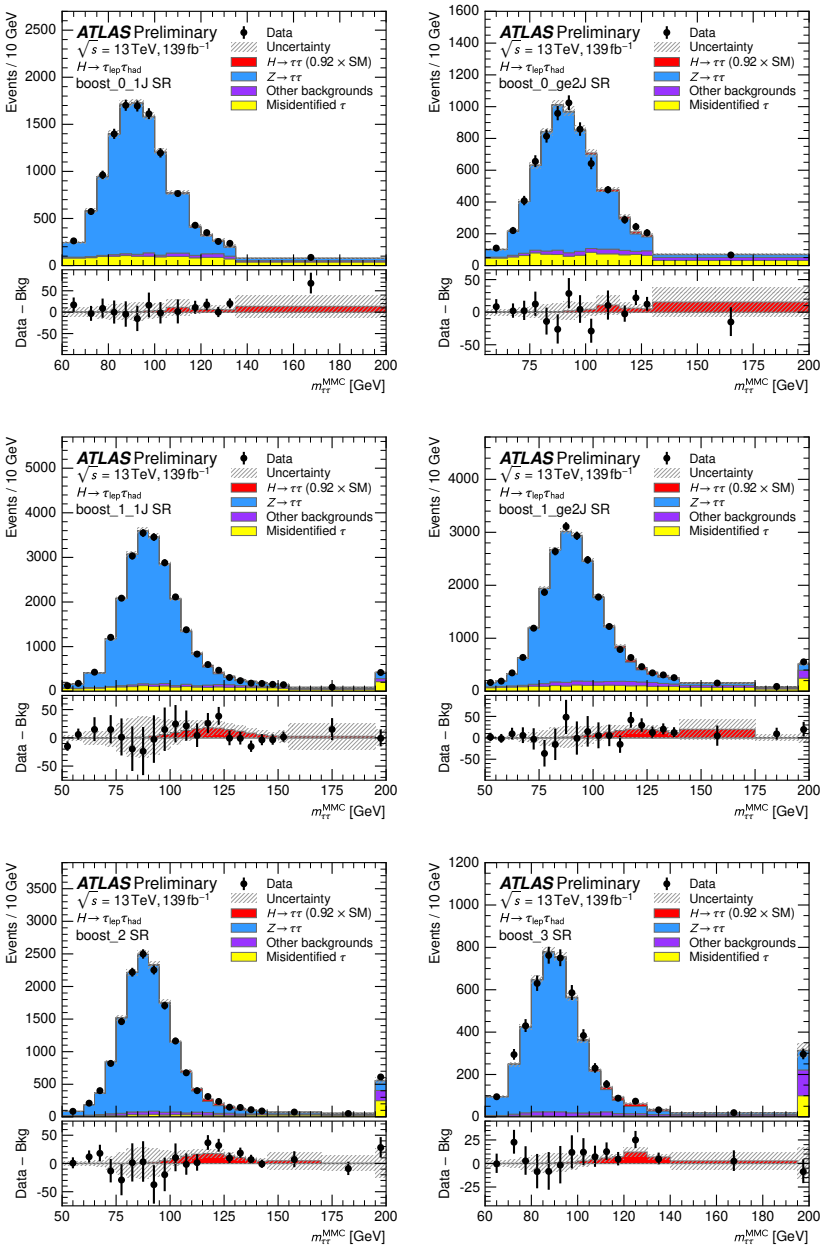

Figure 19: Distribution of the reconstructed di-τ invariant mass ($m_{\tau\tau}^{\mathrm{MMC}}$) for all events in the boost categories of the $\tau_{\mathrm{lep}}\tau_{\mathrm{had}}$ channel. The bottom panel shows the differences between observed data events and expected background events (black points). The observed Higgs-boson signal, corresponding to $(\sigma \times B)/(\sigma \times B)_{\mathrm{SM}} = 0.92$, is shown with a filled red histogram. Entries with values above the x-axis range are shown in the last bin of each distributions. The prediction for each sample is determined from the likelihood fit performed to measure the total $pp \rightarrow H \rightarrow \tau\tau$ cross-section.

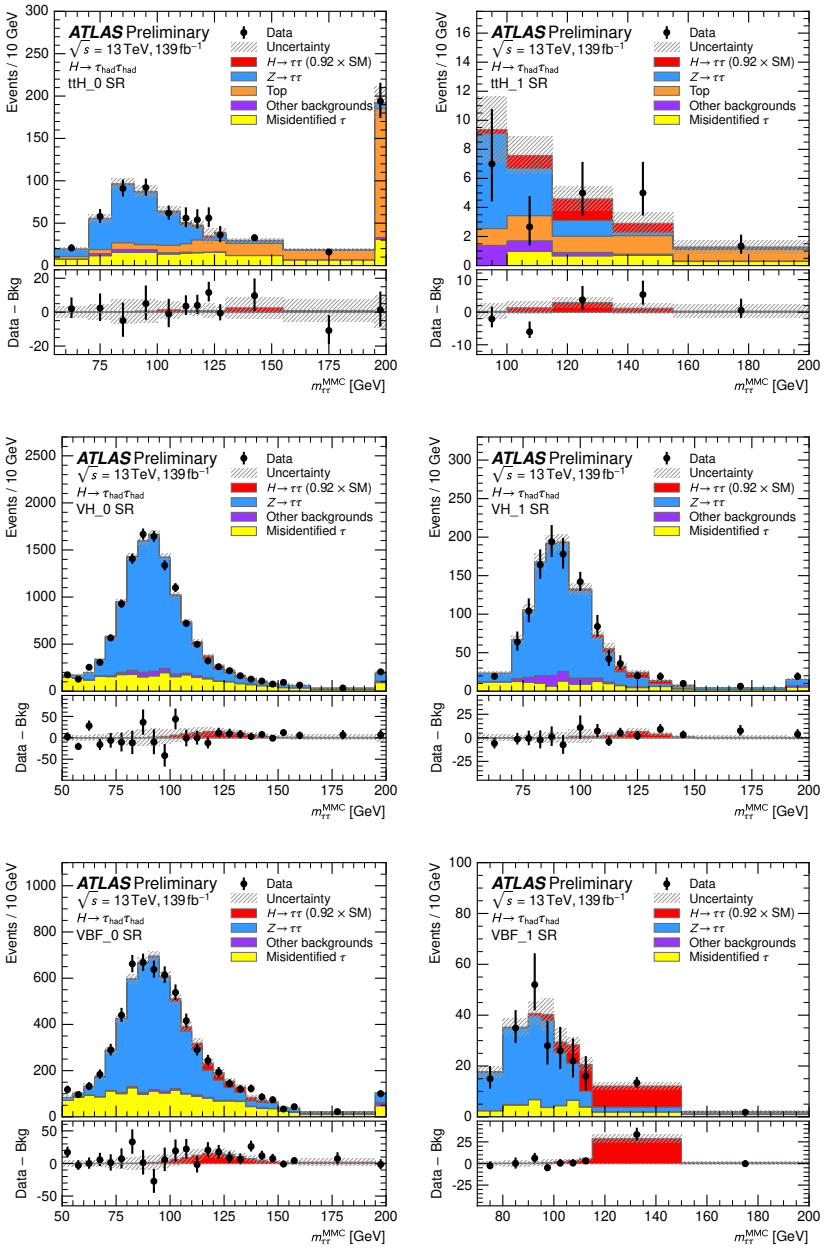

Figure 20: Distribution of the reconstructed di-τ invariant mass ($m_{\tau\tau}^{\mathrm{MMC}}$) for all events in the ttH, V(had)H and VBF categories of the $\tau_{\mathrm{had}}\tau_{\mathrm{had}}$ channel. The bottom panel shows the differences between observed data events and expected background events (black points). The observed Higgs-boson signal, corresponding to $(\sigma \times B)/(\sigma \times B)_{\mathrm{SM}} = 0.92$, is shown with a filled red histogram. Entries with values above the x-axis range are shown in the last bin of each distributions. The prediction for each sample is determined from the likelihood fit performed to measure the total $pp \rightarrow H \rightarrow \tau\tau$ cross-section.

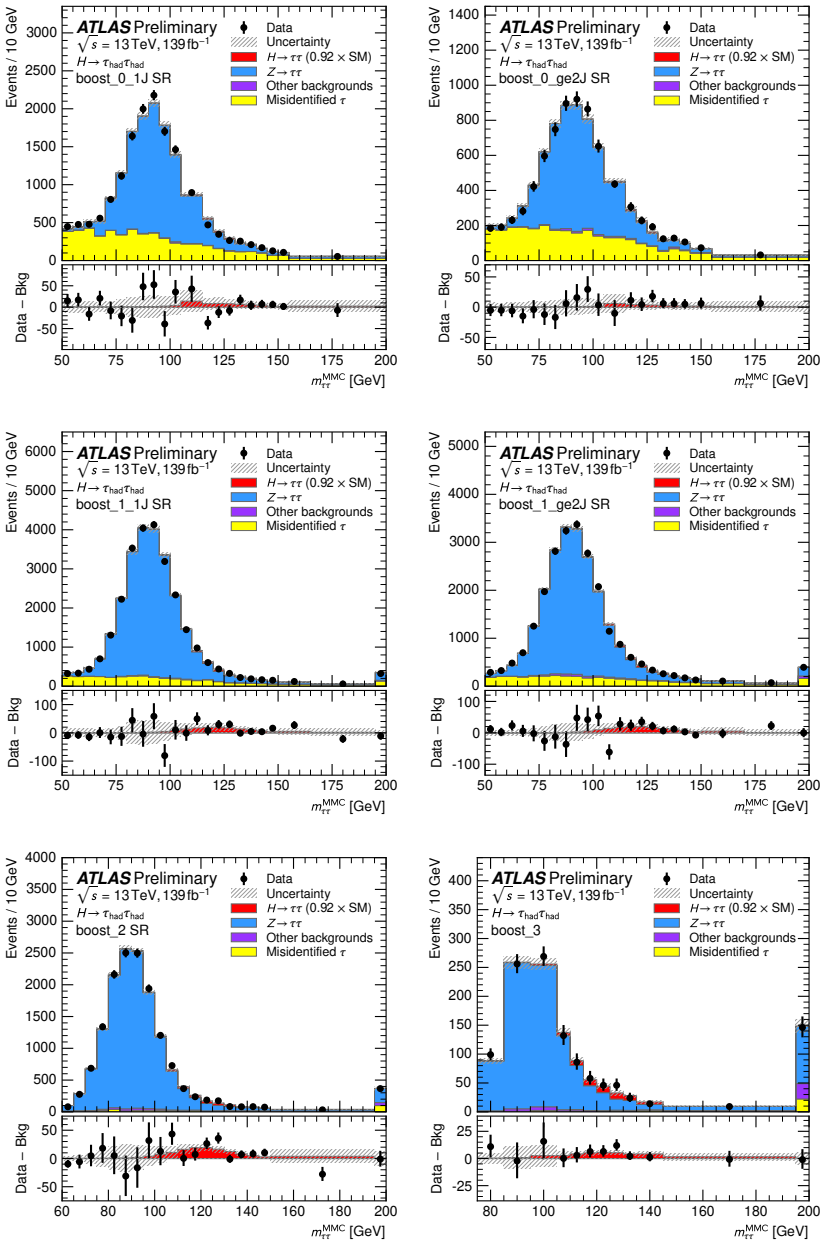

Figure 21: Distribution of the reconstructed di-τ invariant mass ($m_{\tau\tau}^{\mathrm{MMC}}$) for all events in the boost categories of the $\tau_{\mathrm{had}}\tau_{\mathrm{had}}$ channel. The bottom panel shows the differences between observed data events and expected background events (black points). The observed Higgs-boson signal, corresponding to $(\sigma \times B)/(\sigma \times B)_{\mathrm{SM}} = 0.92$, is shown with a filled red histogram. Entries with values above the x-axis range are shown in the last bin of each distributions. The prediction for each sample is determined from the likelihood fit performed to measure the total $pp \rightarrow H \rightarrow \tau\tau$ cross-section.

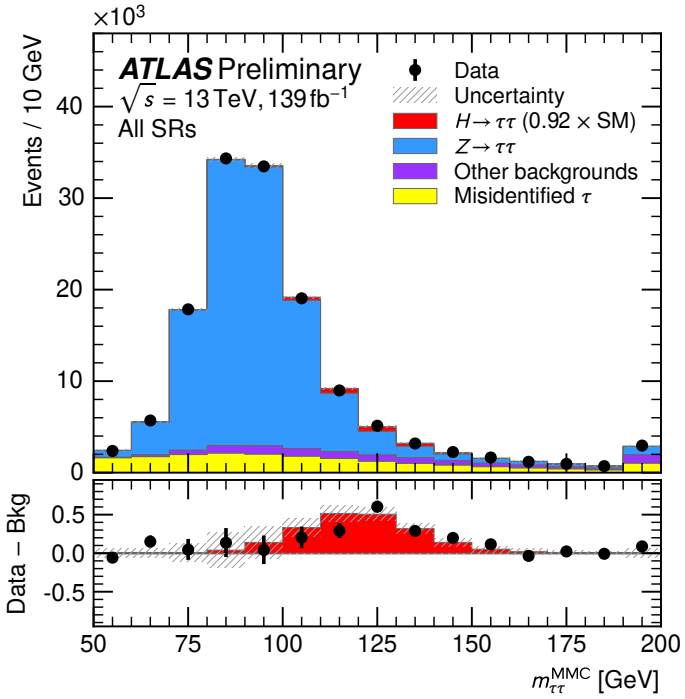

Figure 22: Distribution of the reconstructed di-τ invariant mass ($m_{\tau\tau}^{\text{MMC}}$) for all events in the signal regions. The bottom panel shows the differences between observed data events and expected background events (black points). The observed Higgs-boson signal, corresponding to $(\sigma \times B)/(\sigma \times B)_{\text{SM}} = 0.92$, is shown with a filled red histogram. Entries with values above the x-axis range are shown in the last bin of each distributions. The prediction for each sample is determined from the likelihood fit performed to measure the total $pp \rightarrow H \rightarrow \tau\tau$ cross-section.

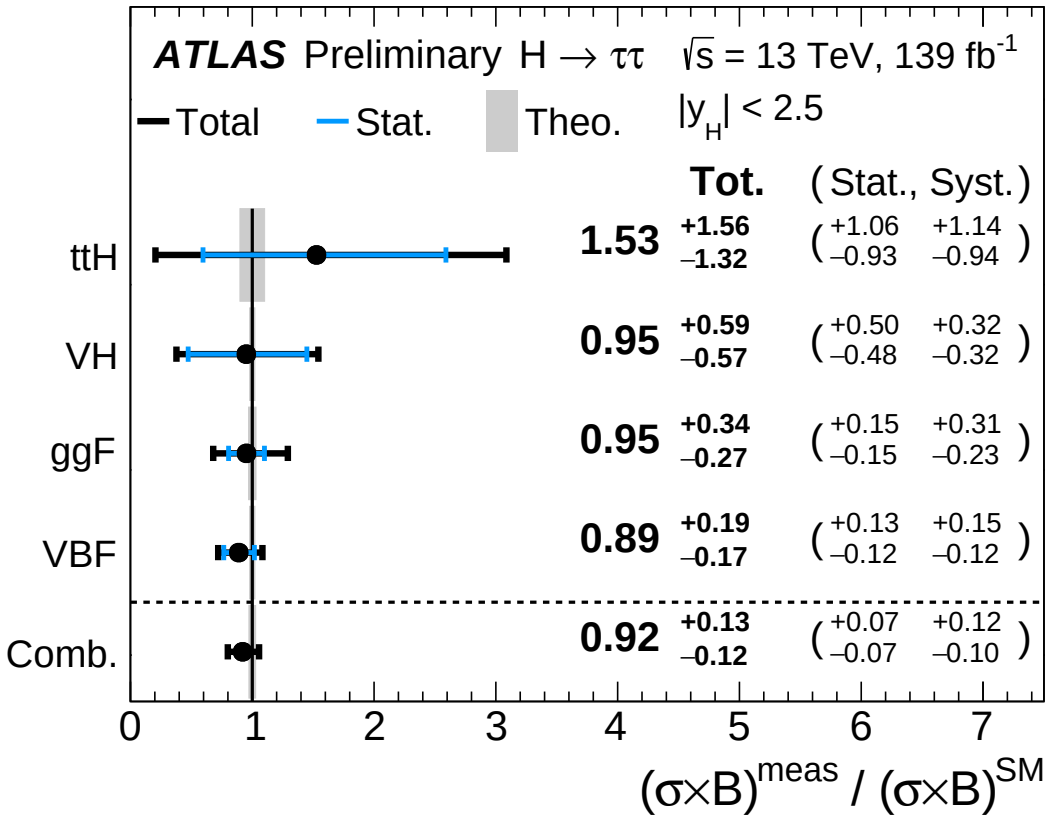

Figure 23: The measured values for $\sigma_H \times B(H \rightarrow \tau\tau)$ relative to the SM expectations in the *Cross-sections per production modes* and the *Total Cross-section* measurements. The total $\pm 1\sigma$ uncertainty in the measurement is indicated by the black error bars, with the individual contribution from the statistical uncertainty in blue.

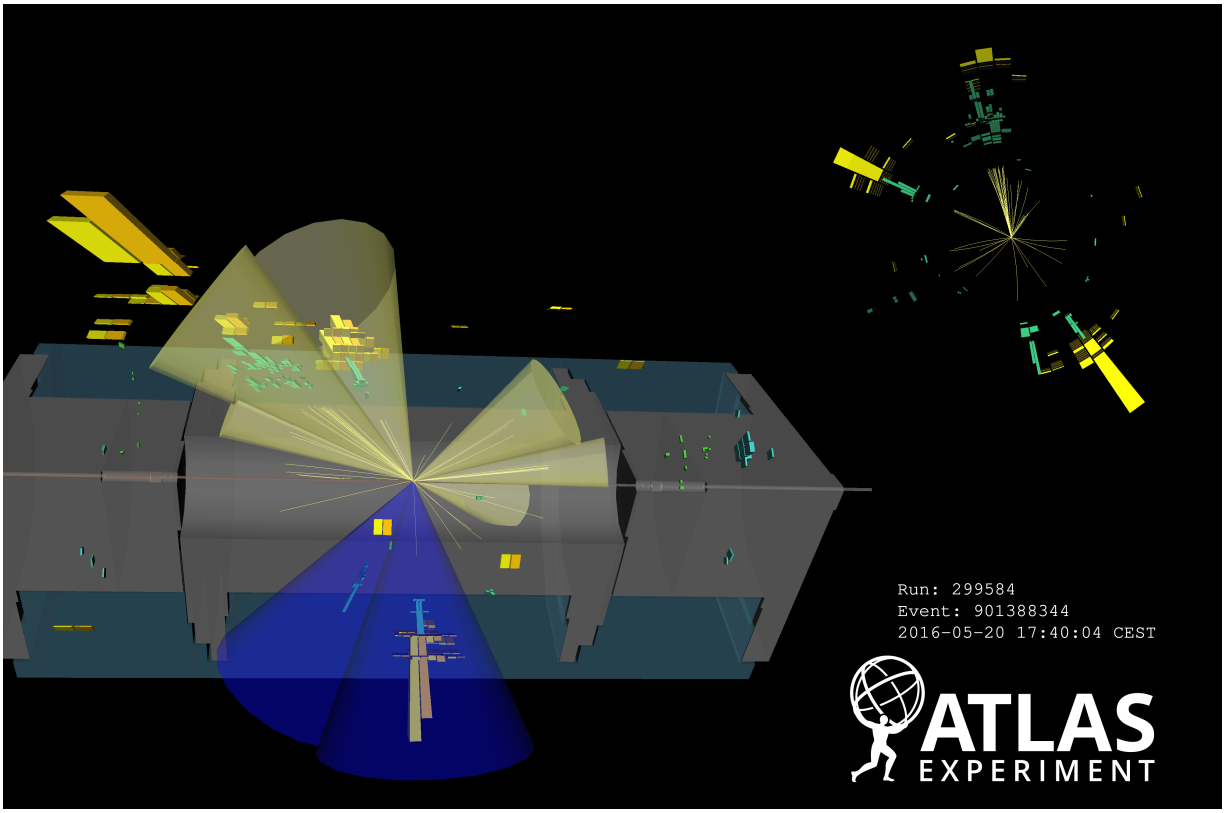

Figure 24: Event display of a $t\bar{t}H, H \rightarrow \tau_{\text{had}}\tau_{\text{had}}$ candidate in the ttH_1 signal region. The hadronically decaying tau leptons (blue cones) have p_{T} = 250.8 and 40.5 GeV, the Higgs boson candidate mass is 140.7 GeV and its transverse momentum is 493.6 GeV. Six jets (yellow cones) are found with p_{T} = 310.9, 183.3, 31.6, 31.5, 24.4 and 23.7 GeV, respectively, and the third jet is b-tagged. The missing transverse momentum has a value of 210.9 GeV.

References

[1] F. Englert and R. Brout, *Broken Symmetry and the Mass of Gauge Vector Mesons*, Phys. Rev. Lett. **13** (1964) 321 (cit. on p. 2).

[2] P. W. Higgs, *Broken symmetries, massless particles and gauge fields*, Phys. Lett. **12** (1964) 132 (cit. on p. 2).

[3] P. W. Higgs, *Broken Symmetries and the Masses of Gauge Bosons*, Phys. Rev. Lett. **13** (1964) 508 (cit. on p. 2).

[4] G. Guralnik, C. Hagen and T. Kibble, *Global Conservation Laws and Massless Particles*, Phys. Rev. Lett. **13** (1964) 585 (cit. on p. 2).

[5] P. W. Higgs, *Spontaneous Symmetry Breakdown without Massless Bosons*, Phys. Rev. **145** (1966) 1156 (cit. on p. 2).

[6] T. Kibble, *Symmetry Breaking in Non-Abelian Gauge Theories*, Phys. Rev. **155** (1967) 1554 (cit. on p. 2).

[7] ATLAS Collaboration, *Observation of a new particle in the search for the Standard Model Higgs boson with the ATLAS detector at the LHC*, Phys. Lett. B **716** (2012) 1, arXiv: 1207.7214 [hep-ex] (cit. on p. 2).

[8] CMS Collaboration, *Observation of a new boson at a mass of 125 GeV with the CMS experiment at the LHC*, Phys. Lett. B **716** (2012) 30, arXiv: 1207.7235 [hep-ex] (cit. on p. 2).

[9] L. Evans and P. Bryant, *LHC Machine*, JINST **3** (2008) S08001 (cit. on p. 2).

[10] ATLAS and CMS Collaborations, *Combined Measurement of the Higgs Boson Mass in pp Collisions at $\sqrt{s} = 7$ and 8 TeV with the ATLAS and CMS Experiments*, Phys. Rev. Lett. **114** (2015) 191803, arXiv: 1503.07589 [hep-ex] (cit. on p. 2).

[11] ATLAS Collaboration, *Measurements of Higgs boson properties in the diphoton decay channel with $36\,fb^{-1}$ of pp collision data at $\sqrt{s} = 13$ TeV with the ATLAS detector*, Phys. Rev. D **98** (2018) 052005, arXiv: 1802.04146 [hep-ex] (cit. on p. 2).

[12] ATLAS Collaboration, *Measurement of the Higgs boson coupling properties in the $H \to ZZ^* \to 4\ell$ decay channel at $\sqrt{s} = 13$ TeV with the ATLAS detector*, JHEP **03** (2018) 095, arXiv: 1712.02304 [hep-ex] (cit. on p. 2).

[13] ATLAS Collaboration, *Measurement of inclusive and differential cross sections in the $H \to ZZ^* \to 4\ell$ decay channel in pp collisions at $\sqrt{s} = 13$ TeV with the ATLAS detector*, JHEP **10** (2017) 132, arXiv: 1708.02810 [hep-ex] (cit. on p. 2).

[14] ATLAS Collaboration, *Measurement of the Higgs boson mass in the $H \to ZZ^* \to 4\ell$ and $H \to \gamma\gamma$ channels with $\sqrt{s} = 13$ TeV pp collisions using the ATLAS detector*, Phys. Lett. B **784** (2018) 345, arXiv: 1806.00242 [hep-ex] (cit. on p. 2).

[15] ATLAS Collaboration, *Combined measurement of differential and total cross sections in the $H \to \gamma\gamma$ and the $H \to ZZ^* \to 4\ell$ decay channels at $\sqrt{s} = 13$ TeV with the ATLAS detector*, Phys. Lett. B **786** (2018) 114, arXiv: 1805.10197 [hep-ex] (cit. on p. 2).

[16] ATLAS Collaboration, *Measurements of gluon-gluon fusion and vector-boson fusion Higgs boson production cross-sections in the $H \to WW^* \to e\nu\mu\nu$ decay channel in pp collisions at $\sqrt{s} = 13$ TeV with the ATLAS detector*, Phys. Lett. B **789** (2019) 508, arXiv: 1808.09054 [hep-ex] (cit. on p. 2).

[17] CMS Collaboration, *Measurement of inclusive and differential Higgs boson production cross sections in the diphoton decay channel in proton–proton collisions at* $\sqrt{s} = 13$ *TeV*, JHEP **01** (2019) 183, arXiv: 1807.03825 [hep-ex] (cit. on p. 2).

[18] CMS Collaboration, *Measurements of Higgs boson properties in the diphoton decay channel in proton–proton collisions at* $\sqrt{s} = 13$ *TeV*, JHEP **11** (2018) 185, arXiv: 1804.02716 [hep-ex] (cit. on p. 2).

[19] CMS Collaboration, *Measurements of properties of the Higgs boson decaying into the four-lepton final state in pp collisions at* $\sqrt{s} = 13$ *TeV*, JHEP **11** (2017) 047, arXiv: 1706.09936 [hep-ex] (cit. on p. 2).

[20] CMS Collaboration, *Measurements of properties of the Higgs boson decaying to a W boson pair in pp collisions at* $\sqrt{s} = 13$ *TeV*, Phys. Lett. B **791** (2019) 96, arXiv: 1806.05246 [hep-ex] (cit. on p. 2).

[21] ATLAS and CMS Collaborations, *Measurements of the Higgs boson production and decay rates and constraints on its couplings from a combined ATLAS and CMS analysis of the LHC pp collision data at* $\sqrt{s} = 7$ *and* 8 *TeV*, JHEP **08** (2016) 045, arXiv: 1606.02266 [hep-ex] (cit. on p. 2).

[22] ATLAS Collaboration, *Cross-section measurements of the Higgs boson decaying into a pair of* τ*-leptons in proton–proton collisions at* $\sqrt{s} = 13$ *TeV with the ATLAS detector*, Phys. Rev. D **99** (2019) 072001, arXiv: 1811.08856 [hep-ex] (cit. on pp. 2, 4, 10, 41).

[23] CMS Collaboration, *Observation of the Higgs boson decay to a pair of* τ *leptons*, Phys. Lett. B **779** (2018) 283, arXiv: 1708.00373 [hep-ex] (cit. on p. 2).

[24] ATLAS Collaboration, *Observation of Higgs boson production in association with a top quark pair at the LHC with the ATLAS detector*, Phys. Lett. B **784** (2018) 173, arXiv: 1806.00425 [hep-ex] (cit. on p. 2).

[25] CMS Collaboration, *Observation of* $t\bar{t}H$ *Production*, Phys. Rev. Lett. **120** (2018) 231801, arXiv: 1804.02610 [hep-ex] (cit. on p. 2).

[26] A. Djouadi, J. Kalinowski and M. Spira, *HDECAY: A program for Higgs boson decays in the Standard Model and its supersymmetric extension*, Comput. Phys. Commun. **108** (1998) 56, arXiv: hep-ph/9704448 (cit. on pp. 2, 5).

[27] D. de Florian et al., *Handbook of LHC Higgs Cross Sections: 4. Deciphering the Nature of the Higgs Sector*, (2016), arXiv: 1610.07922 [hep-ph] (cit. on pp. 2, 3, 5, 28).

[28] ATLAS Collaboration, *Evidence for the Higgs-boson Yukawa coupling to tau leptons with the ATLAS detector*, JHEP **04** (2015) 117, arXiv: 1501.04943 [hep-ex] (cit. on p. 2).

[29] CMS Collaboration, *Evidence for the* 125 *GeV Higgs boson decaying to a pair of* τ *leptons*, JHEP **05** (2014) 104, arXiv: 1401.5041 [hep-ex] (cit. on p. 2).

[30] ATLAS Collaboration, *Test of CP invariance in vector-boson fusion production of the Higgs boson in the* $H \to \tau\tau$ *channel in proton–proton collisions at* $\sqrt{s} = 13$ *TeV with the ATLAS detector*, Phys. Lett. B **805** (2020) 135426, arXiv: 2002.05315 [hep-ex] (cit. on p. 2).

[31] CMS Collaboration, *Search for the associated production of the Higgs boson and a vector boson in proton–proton collisions at* $\sqrt{s} = 13$ *TeV via Higgs boson decays to* τ *leptons*, JHEP **06** (2019) 093, arXiv: 1809.03590 [hep-ex] (cit. on p. 2).

[32] CMS Collaboration, *Measurement of the inclusive and differential Higgs boson production cross sections in the decay mode to a pair of τ leptons in pp collisions at $\sqrt{s}$ = 13 TeV*, (2021), arXiv: 2107.11486 [hep-ex] (cit. on p. 2).

[33] N. Berger et al., *Simplified Template Cross Sections - Stage 1.1*, 2019, arXiv: 1906.02754 [hep-ph] (cit. on p. 2).

[34] ATLAS Collaboration, *Search for the associated production of the Higgs boson with a top quark pair in multilepton final states with the ATLAS detector*, Phys. Lett. B **749** (2015) 519, arXiv: 1506.05988 [hep-ex] (cit. on pp. 3, 13).

[35] ATLAS Collaboration, *Search for the standard model Higgs boson produced in association with a vector boson and decaying into a tau pair in pp collisions at $\sqrt{s}$ = 8 TeV with the ATLAS detector*, Phys. Rev. D **93** (2016) 092005, arXiv: 1511.08352 [hep-ex] (cit. on p. 3).

[36] ATLAS Collaboration, *Modelling $Z \to \tau\tau$ processes in ATLAS with τ-embedded $Z \to \mu\mu$ data*, JINST **10** (2015) P09018, arXiv: 1506.05623 [hep-ex] (cit. on pp. 3, 20).

[37] CMS Collaboration, *An embedding technique to determine $\tau\tau$ backgrounds in proton–proton collision data*, JINST **14** (2019) P06032, arXiv: 1903.01216 [hep-ex] (cit. on pp. 3, 20).

[38] ATLAS Collaboration, *The ATLAS Experiment at the CERN Large Hadron Collider*, JINST **3** (2008) S08003 (cit. on p. 3).

[39] ATLAS Collaboration, *ATLAS Insertable B-Layer: Technical Design Report*, ATLAS-TDR-19; CERN-LHCC-2010-013, 2010, URL: https://cds.cern.ch/record/1291633 (cit. on p. 3), Addendum: ATLAS-TDR-19-ADD-1; CERN-LHCC-2012-009, 2012, URL: https://cds.cern.ch/record/1451888.

[40] B. Abbott et al., *Production and integration of the ATLAS Insertable B-Layer*, JINST **13** (2018) T05008, arXiv: 1803.00844 [physics.ins-det] (cit. on p. 3).

[41] ATLAS Collaboration, *Performance of the ATLAS trigger system in 2015*, Eur. Phys. J. C **77** (2017) 317, arXiv: 1611.09661 [hep-ex] (cit. on p. 4).

[42] ATLAS Collaboration, *The ATLAS Collaboration Software and Firmware*, ATL-SOFT-PUB-2021-001, 2021, URL: https://cds.cern.ch/record/2767187 (cit. on p. 4).

[43] ATLAS Collaboration, *Performance of electron and photon triggers in ATLAS during LHC Run 2*, Eur. Phys. J. C **80** (2020) 47, arXiv: 1909.00761 [hep-ex] (cit. on pp. 4, 8).

[44] ATLAS Collaboration, *Performance of the ATLAS muon triggers in Run 2*, JINST **15** (2020) P09015, arXiv: 2004.13447 [hep-ex] (cit. on pp. 4, 8).

[45] ATLAS Collaboration, *The ATLAS Inner Detector Trigger performance in pp collisions at 13 TeV during LHC Run 2*, Submitted to Eur. Phys. J. C (2021), arXiv: 2107.02485 [hep-ex] (cit. on p. 4).

[46] ATLAS Collaboration, *Performance of the ATLAS Level-1 topological trigger in Run 2*, Submitted to Eur. Phys. J. C (2021), arXiv: 2105.01416 [hep-ex] (cit. on p. 4).

[47] ATLAS Collaboration, *ATLAS data quality operations and performance for 2015–2018 data-taking*, JINST **15** (2020) P04003, arXiv: 1911.04632 [physics.ins-det] (cit. on p. 4).

[48] ATLAS Collaboration,
Luminosity determination in pp collisions at $\sqrt{s} = 8$ TeV using the ATLAS detector at the LHC,
Eur. Phys. J. C **76** (2016) 653, arXiv: 1608.03953 [hep-ex] (cit. on p. 4).

[49] G. Avoni et al., *The new LUCID-2 detector for luminosity measurement and monitoring in ATLAS*,
JINST **13** (2018) P07017 (cit. on p. 4).

[50] ATLAS Collaboration, *The ATLAS Simulation Infrastructure*, Eur. Phys. J. C **70** (2010) 823,
arXiv: 1005.4568 [physics.ins-det] (cit. on p. 4).

[51] S. Agostinelli et al., *GEANT4: a simulation toolkit*, Nucl. Instrum. Meth. A **506** (2003) 250
(cit. on p. 4).

[52] T. Sjöstrand, S. Mrenna and P. Z. Skands, *A brief introduction to PYTHIA 8.1*,
Comput. Phys. Commun. **178** (2008) 852, arXiv: 0710.3820 [hep-ph] (cit. on p. 5).

[53] ATLAS Collaboration, *The Pythia 8 A3 tune description of ATLAS minimum bias and inelastic measurements incorporating the Donnachie–Landshoff diffractive model*,
ATL-PHYS-PUB-2016-017, 2016, URL: https://cds.cern.ch/record/2206965
(cit. on p. 5).

[54] R. D. Ball et al., *Parton distributions with LHC data*, Nucl. Phys. B **867** (2013) 244,
arXiv: 1207.1303 [hep-ph] (cit. on p. 5).

[55] P. Ilten, *Tau Decays in Pythia 8*, Nuclear Physics B - Proceedings Supplements **253-255** (2014) 77,
The Twelfth International Workshop on Tau-Lepton Physics (TAU2012) (cit. on p. 5).

[56] P. Golonka et al.,
The tauola-photos-F environment for the TAUOLA and PHOTOS packages, release II,
Computer Physics Communications **174** (2006) 818 (cit. on p. 5).

[57] J. Butterworth et al., *PDF4LHC recommendations for LHC Run II*, J. Phys. G **43** (2016) 023001,
arXiv: 1510.03865 [hep-ph] (cit. on p. 5).

[58] R. D. Ball et al., *Parton distributions for the LHC run II*, JHEP **04** (2015) 040,
arXiv: 1410.8849 [hep-ph] (cit. on pp. 5, 6).

[59] H.-L. Lai et al., *New parton distributions for collider physics*, Phys. Rev. D **82** (2010) 074024,
arXiv: 1007.2241 [hep-ph] (cit. on p. 5).

[60] T. Sjöstrand et al., *An introduction to PYTHIA 8.2*, Comput. Phys. Commun. **191** (2015) 159,
arXiv: 1410.3012 [hep-ph] (cit. on pp. 5, 6).

[61] ATLAS Collaboration, *Measurement of the Z/γ^* boson transverse momentum distribution in pp collisions at $\sqrt{s} = 7$ TeV with the ATLAS detector*, JHEP **09** (2014) 145,
arXiv: 1406.3660 [hep-ex] (cit. on p. 5).

[62] ATLAS Collaboration, *ATLAS Pythia 8 tunes to 7 TeV data*, ATL-PHYS-PUB-2014-021, 2014,
URL: https://cds.cern.ch/record/1966419 (cit. on pp. 5, 6).

[63] S. Frixione, P. Nason and G. Ridolfi,
A positive-weight next-to-leading-order Monte Carlo for heavy flavour hadroproduction,
JHEP **09** (2007) 126, arXiv: 0707.3088 [hep-ph] (cit. on pp. 5, 6).

[64] P. Nason, *A new method for combining NLO QCD with shower Monte Carlo algorithms*,
JHEP **11** (2004) 040, arXiv: hep-ph/0409146 (cit. on pp. 5, 6).

[65] S. Frixione, P. Nason and C. Oleari,
Matching NLO QCD computations with parton shower simulations: the POWHEG method,
JHEP **11** (2007) 070, arXiv: 0709.2092 [hep-ph] (cit. on pp. 5, 6).

[66] S. Alioli, P. Nason, C. Oleari and E. Re, *A general framework for implementing NLO calculations in shower Monte Carlo programs: the POWHEG BOX*, JHEP **06** (2010) 043,
arXiv: 1002.2581 [hep-ph] (cit. on pp. 5, 6).

[67] H. B. Hartanto, B. Jäger, L. Reina and D. Wackeroth,
Higgs boson production in association with top quarks in the POWHEG BOX,
Phys. Rev. D **91** (2015) 094003, arXiv: 1501.04498 [hep-ph] (cit. on p. 5).

[68] K. Hamilton, P. Nason and G. Zanderighi, *MINLO: Multi-Scale Improved NLO*,
JHEP **10** (2012) 155, arXiv: 1206.3572 [hep-ph] (cit. on p. 5).

[69] J. M. Campbell et al., *NLO Higgs Boson Production Plus One and Two Jets Using the POWHEG BOX, MadGraph4 and MCFM*, JHEP **07** (2012) 092, arXiv: 1202.5475 [hep-ph] (cit. on p. 5).

[70] K. Hamilton, P. Nason, C. Oleari and G. Zanderighi, *Merging H/W/Z + 0 and 1 jet at NLO with no merging scale: a path to parton shower + NNLO matching*, JHEP **05** (2013) 082,
arXiv: 1212.4504 [hep-ph] (cit. on p. 5).

[71] S. Catani and M. Grazzini, *An NNLO subtraction formalism in hadron collisions and its application to Higgs boson production at the LHC*, Phys. Rev. Lett. **98** (2007) 222002,
arXiv: hep-ph/0703012 [hep-ph] (cit. on p. 5).

[72] C. Anastasiou et al.,
High precision determination of the gluon fusion Higgs boson cross-section at the LHC,
JHEP **05** (2016) 058, arXiv: 1602.00695 [hep-ph] (cit. on p. 5).

[73] C. Anastasiou, C. Duhr, F. Dulat, F. Herzog and B. Mistlberger,
Higgs Boson Gluon-Fusion Production in QCD at Three Loops,
Phys. Rev. Lett. **114** (2015) 212001, arXiv: 1503.06056 [hep-ph] (cit. on p. 5).

[74] F. Dulat, A. Lazopoulos and B. Mistlberger, *iHixs 2 – Inclusive Higgs cross sections*,
Comput. Phys. Commun. **233** (2018) 243, arXiv: 1802.00827 [hep-ph] (cit. on p. 5).

[75] R. V. Harlander and K. J. Ozeren,
Finite top mass effects for hadronic Higgs production at next-to-next-to-leading order,
JHEP **11** (2009) 088, arXiv: 0909.3420 [hep-ph] (cit. on p. 5).

[76] R. V. Harlander and K. J. Ozeren,
Top mass effects in Higgs production at next-to-next-to-leading order QCD: Virtual corrections,
Phys. Lett. B **679** (2009) 467, arXiv: 0907.2997 [hep-ph] (cit. on p. 5).

[77] R. V. Harlander, H. Mantler, S. Marzani and K. J. Ozeren,
Higgs production in gluon fusion at next-to-next-to-leading order QCD for finite top mass,
Eur. Phys. J. C **66** (2010) 359, arXiv: 0912.2104 [hep-ph] (cit. on p. 5).

[78] A. Pak, M. Rogal and M. Steinhauser,
Finite top quark mass effects in NNLO Higgs boson production at LHC, JHEP **02** (2010) 025,
arXiv: 0911.4662 [hep-ph] (cit. on p. 5).

[79] S. Actis, G. Passarino, C. Sturm and S. Uccirati,
NLO electroweak corrections to Higgs boson production at hadron colliders,
Phys. Lett. B **670** (2008) 12, arXiv: 0809.1301 [hep-ph] (cit. on p. 5).

[80] S. Actis, G. Passarino, C. Sturm and S. Uccirati,
NNLO computational techniques: The cases $H \to \gamma\gamma$ and $H \to gg$, Nucl. Phys. B **811** (2009) 182,
arXiv: 0809.3667 [hep-ph] (cit. on p. 5).

[81] M. Bonetti, K. Melnikov and L. Tancredi, *Higher order corrections to mixed QCD-EW contributions to Higgs boson production in gluon fusion*, Phys. Rev. D **97** (2018) 056017,
arXiv: 1801.10403 [hep-ph] (cit. on p. 5), Erratum: Phys. Rev. D **97** (2018) 099906.

[82] M. Ciccolini, A. Denner and S. Dittmaier, *Strong and Electroweak Corrections to the Production of Higgs + 2 Jets via Weak Interactions at the Large Hadron Collider*,
Phys. Rev. Lett. **99** (2007) 161803, arXiv: 0707.0381 [hep-ph] (cit. on p. 5).

[83] M. Ciccolini, A. Denner and S. Dittmaier,
Electroweak and QCD corrections to Higgs production via vector-boson fusion at the CERN LHC,
Phys. Rev. D **77** (2008) 013002, arXiv: 0710.4749 [hep-ph] (cit. on p. 5).

[84] P. Bolzoni, F. Maltoni, S.-O. Moch and M. Zaro,
Higgs Boson Production via Vector-Boson Fusion at Next-to-Next-to-Leading Order in QCD,
Phys. Rev. Lett. **105** (2010) 011801, arXiv: 1003.4451 [hep-ph] (cit. on p. 5).

[85] M. L. Ciccolini, S. Dittmaier and M. Krämer,
Electroweak radiative corrections to associated WH and ZH production at hadron colliders,
Phys. Rev. D **68** (2003) 073003, arXiv: hep-ph/0306234 [hep-ph] (cit. on p. 5).

[86] O. Brein, A. Djouadi and R. Harlander,
NNLO QCD corrections to the Higgs-strahlung processes at hadron colliders,
Phys. Lett. B **579** (2004) 149, arXiv: hep-ph/0307206 (cit. on p. 5).

[87] O. Brein, R. Harlander, M. Wiesemann and T. Zirke,
Top-Quark Mediated Effects in Hadronic Higgs-Strahlung, Eur. Phys. J. C **72** (2012) 1868,
arXiv: 1111.0761 [hep-ph] (cit. on p. 5).

[88] L. Altenkamp, S. Dittmaier, R. V. Harlander, H. Rzehak and T. J. E. Zirke,
Gluon-induced Higgs-strahlung at next-to-leading order QCD, JHEP **02** (2013) 078,
arXiv: 1211.5015 [hep-ph] (cit. on p. 5).

[89] A. Denner, S. Dittmaier, S. Kallweit and A. Mück, *HAWK 2.0: A Monte Carlo program for Higgs production in vector-boson fusion and Higgs strahlung at hadron colliders*,
Comput. Phys. Commun. **195** (2015) 161, arXiv: 1412.5390 [hep-ph] (cit. on p. 5).

[90] O. Brein, R. V. Harlander and T. J. E. Zirke, *vh@nnlo – Higgs Strahlung at hadron colliders*,
Comput. Phys. Commun. **184** (2013) 998, arXiv: 1210.5347 [hep-ph] (cit. on p. 5).

[91] R. V. Harlander, A. Kulesza, V. Theeuwes and T. Zirke,
Soft gluon resummation for gluon-induced Higgs Strahlung, JHEP **11** (2014) 082,
arXiv: 1410.0217 [hep-ph] (cit. on p. 5).

[92] D. J. Lange, *The EvtGen particle decay simulation package*,
Nucl. Instrum. Meth. A **462** (2001) 152 (cit. on p. 5).

[93] W. Beenakker, S. Dittmaier, M. Krämer, B. Plumper, M. Spira et al.,
NLO QCD corrections to $t\bar{t}H$ production in hadron collisions, Nucl. Phys. **B653** (2003) 151,
arXiv: hep-ph/0211352 [hep-ph] (cit. on p. 5).

[94] S. Dawson, C. Jackson, L. Orr, L. Reina and D. Wackeroth,
Associated Higgs production with top quarks at the large hadron collider: NLO QCD corrections,
Phys. Rev. **D68** (2003) 034022, arXiv: hep-ph/0305087 [hep-ph] (cit. on p. 5).

[95] Y. Zhang, W.-G. Ma, R.-Y. Zhang, C. Chen and L. Guo,
QCD NLO and EW NLO corrections to $t\bar{t}H$ production with top quark decays at hadron collider,
Phys. Lett. **B738** (2014) 1, arXiv: 1407.1110 [hep-ph] (cit. on p. 5).

[96] S. Frixione, V. Hirschi, D. Pagani, H. S. Shao and M. Zaro,
Weak corrections to Higgs hadroproduction in association with a top-quark pair,
JHEP **09** (2014) 065, arXiv: 1407.0823 [hep-ph] (cit. on p. 5).

[97] J. Alwall et al., *The automated computation of tree-level and next-to-leading order differential cross sections, and their matching to parton shower simulations*, JHEP **07** (2014) 079,
arXiv: 1405.0301 [hep-ph] (cit. on p. 5).

[98] F. Demartin, F. Maltoni, K. Mawatari and M. Zaro,
Higgs production in association with a single top quark at the LHC, Eur. Phys. J. C **75** (2015) 267,
arXiv: 1504.00611 [hep-ph] (cit. on p. 5).

[99] F. Demartin, B. Maier, F. Maltoni, K. Mawatari and M. Zaro,
tWH associated production at the LHC, Eur. Phys. J. C **77** (2017) 34,
arXiv: 1607.05862 [hep-ph] (cit. on p. 5).

[100] M. Spira, *QCD Effects in Higgs physics*, Fortsch. Phys. **46** (1998) 203, arXiv: hep-ph/9705337 (cit. on p. 5).

[101] A. Djouadi, M. M. Mühlleitner and M. Spira,
Decays of supersymmetric particles: The Program SUSY-HIT (SUspect-SdecaY-Hdecay-InTerface),
Acta Phys. Polon. B **38** (2007) 635, arXiv: hep-ph/0609292 (cit. on p. 5).

[102] A. Bredenstein, A. Denner, S. Dittmaier and M. M. Weber, *Radiative corrections to the semileptonic and hadronic Higgs-boson decays $H \to WW/ZZ \to 4$ fermions*,
JHEP **02** (2007) 080, arXiv: hep-ph/0611234 (cit. on p. 5).

[103] A. Bredenstein, A. Denner, S. Dittmaier and M. M. Weber,
Precise predictions for the Higgs-boson decay $H \to WW/ZZ \to 4$ leptons,
Phys. Rev. D **74** (2006) 013004, arXiv: hep-ph/0604011 [hep-ph] (cit. on p. 5).

[104] A. Bredenstein, A. Denner, S. Dittmaier and M. M. Weber,
Precision calculations for the Higgs-boson decay $H \to ZZ/WW \to 4$ leptons,
Nucl. Phys. Proc. Suppl. **160** (2006) 131, arXiv: hep-ph/0607060 [hep-ph] (cit. on p. 5).

[105] E. Bothmann et al., *Event generation with Sherpa 2.2*, SciPost Phys. **7** (2019) 034,
arXiv: 1905.09127 [hep-ph] (cit. on p. 6).

[106] T. Gleisberg and S. Höche, *Comix, a new matrix element generator*, JHEP **12** (2008) 039,
arXiv: 0808.3674 [hep-ph] (cit. on p. 6).

[107] F. Buccioni et al., *OpenLoops 2*, Eur. Phys. J. C **79** (2019) 866, arXiv: 1907.13071 [hep-ph] (cit. on p. 6).

[108] F. Cascioli, P. Maierhöfer and S. Pozzorini, *Scattering Amplitudes with Open Loops*,
Phys. Rev. Lett. **108** (2012) 111601, arXiv: 1111.5206 [hep-ph] (cit. on p. 6).

[109] A. Denner, S. Dittmaier and L. Hofer,
Collier: A fortran-based complex one-loop library in extended regularizations,
Comput. Phys. Commun. **212** (2017) 220, arXiv: 1604.06792 [hep-ph] (cit. on p. 6).

[110] S. Schumann and F. Krauss,
A parton shower algorithm based on Catani–Seymour dipole factorisation, JHEP **03** (2008) 038,
arXiv: 0709.1027 [hep-ph] (cit. on p. 6).

[111] S. Höche, F. Krauss, M. Schönherr and F. Siegert,
A critical appraisal of NLO+PS matching methods, JHEP **09** (2012) 049,
arXiv: 1111.1220 [hep-ph] (cit. on p. 6).

[112] S. Höche, F. Krauss, M. Schönherr and F. Siegert,
QCD matrix elements + parton showers. The NLO case, JHEP **04** (2013) 027,
arXiv: 1207.5030 [hep-ph] (cit. on p. 6).

[113] S. Catani, F. Krauss, R. Kuhn and B. R. Webber, *QCD Matrix Elements + Parton Showers*,
JHEP **11** (2001) 063, arXiv: hep-ph/0109231 (cit. on p. 6).

[114] S. Höche, F. Krauss, S. Schumann and F. Siegert, *QCD matrix elements and truncated showers*,
JHEP **05** (2009) 053, arXiv: 0903.1219 [hep-ph] (cit. on p. 6).

[115] C. Anastasiou, L. J. Dixon, K. Melnikov and F. Petriello, *High precision QCD at hadron colliders: Electroweak gauge boson rapidity distributions at next-to-next-to leading order*,
Phys. Rev. D **69** (2004) 094008, arXiv: hep-ph/0312266 (cit. on p. 6).

[116] ATLAS Collaboration, *Studies on top-quark Monte Carlo modelling for Top2016*,
ATL-PHYS-PUB-2016-020, 2016, URL: https://cds.cern.ch/record/2216168
(cit. on p. 6).

[117] M. Beneke, P. Falgari, S. Klein and C. Schwinn,
Hadronic top-quark pair production with NNLL threshold resummation,
Nucl. Phys. B **855** (2012) 695, arXiv: 1109.1536 [hep-ph] (cit. on p. 6).

[118] M. Cacciari, M. Czakon, M. Mangano, A. Mitov and P. Nason, *Top-pair production at hadron colliders with next-to-next-to-leading logarithmic soft-gluon resummation*,
Phys. Lett. B **710** (2012) 612, arXiv: 1111.5869 [hep-ph] (cit. on p. 6).

[119] P. Bärnreuther, M. Czakon and A. Mitov, *Percent-Level-Precision Physics at the Tevatron: Next-to-Next-to-Leading Order QCD Corrections to $q\bar{q} \to t\bar{t} + X$*,
Phys. Rev. Lett. **109** (2012) 132001, arXiv: 1204.5201 [hep-ph] (cit. on p. 6).

[120] M. Czakon and A. Mitov,
NNLO corrections to top-pair production at hadron colliders: the all-fermionic scattering channels,
JHEP **12** (2012) 054, arXiv: 1207.0236 [hep-ph] (cit. on p. 6).

[121] M. Czakon and A. Mitov,
NNLO corrections to top pair production at hadron colliders: the quark-gluon reaction,
JHEP **01** (2013) 080, arXiv: 1210.6832 [hep-ph] (cit. on p. 6).

[122] M. Czakon, P. Fiedler and A. Mitov,
Total Top-Quark Pair-Production Cross Section at Hadron Colliders Through $O(\alpha_S^4)$,
Phys. Rev. Lett. **110** (2013) 252004, arXiv: 1303.6254 [hep-ph] (cit. on p. 6).

[123] M. Czakon and A. Mitov,
Top++: A program for the calculation of the top-pair cross-section at hadron colliders,
Comput. Phys. Commun. **185** (2014) 2930, arXiv: 1112.5675 [hep-ph] (cit. on p. 6).

[124] M. Aliev et al., *HATHOR – HAdronic Top and Heavy quarks crOss section calculatoR*,
Comput. Phys. Commun. **182** (2011) 1034, arXiv: 1007.1327 [hep-ph] (cit. on p. 6).

[125] P. Kant et al., *HatHor for single top-quark production: Updated predictions and uncertainty estimates for single top-quark production in hadronic collisions*,
Comput. Phys. Commun. **191** (2015) 74, arXiv: 1406.4403 [hep-ph] (cit. on p. 6).

[126] F. Cascioli et al., *Precise Higgs-background predictions: Merging NLO QCD and squared quark-loop corrections to four-lepton + 0,1 jet production*, Journal of High Energy Physics **2014** (2013) (cit. on p. 6).

[127] ATLAS Collaboration, *Reconstruction of primary vertices at the ATLAS experiment in Run 1 proton–proton collisions at the LHC*, Eur. Phys. J. C **77** (2017) 332, arXiv: 1611.10235 [hep-ex] (cit. on p. 7).

[128] ATLAS Collaboration, *Electron and photon performance measurements with the ATLAS detector using the 2015–2017 LHC proton–proton collision data*, JINST **14** (2019) P12006, arXiv: 1908.00005 [hep-ex] (cit. on p. 7).

[129] ATLAS Collaboration, *2015 start-up trigger menu and initial performance assessment of the ATLAS trigger using Run-2 data*, ATL-DAQ-PUB-2016-001, 2016, URL: https://cds.cern.ch/record/2136007 (cit. on p. 8).

[130] ATLAS Collaboration, *Trigger Menu in 2016*, ATL-DAQ-PUB-2017-001, 2017, URL: https://cds.cern.ch/record/2242069 (cit. on p. 8).

[131] ATLAS Collaboration, *Trigger Menu in 2017*, ATL-DAQ-PUB-2018-002, 2018, URL: https://cds.cern.ch/record/2625986 (cit. on p. 8).

[132] ATLAS Collaboration, *Trigger Menu in 2018*, ATL-DAQ-PUB-2019-001, 2019, URL: https://cds.cern.ch/record/2693402 (cit. on p. 8).

[133] ATLAS Collaboration, *Muon reconstruction and identification efficiency in ATLAS using the full Run 2 pp collision data set at* $\sqrt{s} = 13$ *TeV*, (2020), arXiv: 2012.00578 [hep-ex] (cit. on p. 8).

[134] M. Cacciari, G. P. Salam and G. Soyez, *The anti-k_t jet clustering algorithm*, JHEP **04** (2008) 063, arXiv: 0802.1189 [hep-ph] (cit. on p. 8).

[135] ATLAS Collaboration, *Topological cell clustering in the ATLAS calorimeters and its performance in LHC Run 1*, Eur. Phys. J. C **77** (2017) 490, arXiv: 1603.02934 [hep-ex] (cit. on p. 8).

[136] ATLAS Collaboration, *Measurement of the tau lepton reconstruction and identification performance in the ATLAS experiment using pp collisions at* $\sqrt{s} = 13$ *TeV*, ATLAS-CONF-2017-029, 2017, URL: https://cds.cern.ch/record/2261772 (cit. on pp. 8, 27).

[137] ATLAS Collaboration, *Reconstruction of hadronic decay products of tau leptons with the ATLAS experiment*, Eur. Phys. J. C **76** (2016) 295, arXiv: 1512.05955 [hep-ex] (cit. on pp. 8, 10).

[138] ATLAS Collaboration, *Identification of hadronic tau lepton decays using neural networks in the ATLAS experiment*, ATL-PHYS-PUB-2019-033, 2019, URL: https://cds.cern.ch/record/2688062 (cit. on p. 9).

[139] ATLAS Collaboration, *Jet reconstruction and performance using particle flow with the ATLAS Detector*, Eur. Phys. J. C **77** (2017) 466, arXiv: 1703.10485 [hep-ex] (cit. on p. 9).

[140] ATLAS Collaboration, *Selection of jets produced in* 13 *TeV proton–proton collisions with the ATLAS detector*, ATLAS-CONF-2015-029, 2015, URL: https://cds.cern.ch/record/2037702 (cit. on p. 9).

[141] ATLAS Collaboration, *Performance of pile-up mitigation techniques for jets in pp collisions at $\sqrt{s}$ = 8 TeV using the ATLAS detector*, Eur. Phys. J. C **76** (2016) 581, arXiv: 1510.03823 [hep-ex] (cit. on p. 9).

[142] ATLAS Collaboration, *Identification and rejection of pile-up jets at high pseudorapidity with the ATLAS detector*, Eur. Phys. J. C **77** (2017) 580, arXiv: 1705.02211 [hep-ex] (cit. on p. 9), Erratum: Eur. Phys. J. C **77** (2017) 712.

[143] ATLAS Collaboration, *ATLAS b-jet identification performance and efficiency measurement with $t\bar{t}$ events in pp collisions at $\sqrt{s}$ = 13 TeV*, Eur. Phys. J. C **79** (2019) 970, arXiv: 1907.05120 [hep-ex] (cit. on p. 9).

[144] ATLAS Collaboration, *Optimisation and performance studies of the ATLAS b-tagging algorithms for the 2017-18 LHC run*, ATL-PHYS-PUB-2017-013, 2017, URL: https://cds.cern.ch/record/2273281 (cit. on p. 9).

[145] ATLAS Collaboration, *Performance of missing transverse momentum reconstruction with the ATLAS detector using proton–proton collisions at $\sqrt{s}$ = 13 TeV*, Eur. Phys. J. C **78** (2018) 903, arXiv: 1802.08168 [hep-ex] (cit. on pp. 10, 27).

[146] A. Elagin, P. Murat, A. Pranko and A. Safonov, *A new mass reconstruction technique for resonances decaying to di-τ*, Nucl. Instrum. Meth. **A 654** (2011) 481, arXiv: 1012.4686 [hep-ex] (cit. on p. 10).

[147] R. Ellis, I. Hinchliffe, M. Soldate and J. van der Bij, *Higgs decay to $\tau^+\tau^-$: A possible signature of intermediate mass Higgs bosons at high energy hadron colliders*, Nucl. Phys. B **297** (1988) 221 (cit. on p. 10).

[148] ATLAS Collaboration, *Formulae for Estimating Significance*, ATL-PHYS-PUB-2020-025, 2020, URL: https://cds.cern.ch/record/2736148 (cit. on p. 13).

[149] ATLAS Collaboration, *Measurements of the production cross section of a Z boson in association with jets in pp collisions at $\sqrt{s}$ = 13 TeV with the ATLAS detector*, Eur. Phys. J. C **77** (2017) 361, arXiv: 1702.05725 [hep-ex] (cit. on p. 21).

[150] ATLAS Collaboration, *Measurement of the cross-section for electroweak production of dijets in association with a Z boson in pp collisions at $\sqrt{s}$ = 13 TeV with the ATLAS detector*, Phys. Lett. B **775** (2017) 206, arXiv: 1709.10264 [hep-ex] (cit. on p. 21).

[151] ATLAS Collaboration, *Estimation of non-prompt and fake lepton backgrounds in final states with top quarks produced in proton–proton collisions at $\sqrt{s}$ = 8 TeV with the ATLAS Detector*, ATLAS-CONF-2014-058, 2014, URL: https://cds.cern.ch/record/1951336 (cit. on p. 23).

[152] ATLAS Collaboration, *Measurements of Higgs boson production and couplings in the four-lepton channel in pp collisions at center-of-mass energies of 7 and 8 TeV with the ATLAS detector*, Phys. Rev. D **91** (2015) 012006, arXiv: 1408.5191 [hep-ex] (cit. on p. 23).

[153] ATLAS Collaboration, *Jet energy scale and resolution measured in proton–proton collisions at $\sqrt{s}$ = 13 TeV with the ATLAS detector*, (2020), arXiv: 2007.02645 [hep-ex] (cit. on p. 27).

[154] ATLAS Collaboration, *Luminosity determination in pp collisions at $\sqrt{s}$ = 13 TeV using the ATLAS detector at the LHC*, ATLAS-CONF-2019-021, 2019, URL: https://cds.cern.ch/record/2677054 (cit. on p. 27).

[155] G. Avoni et al., *The new LUCID-2 detector for luminosity measurement and monitoring in ATLAS*, JINST **13** (2018) P07017 (cit. on p. 27).

[156] E. Bothmann, M. Schönherr and S. Schumann,
Reweighting QCD matrix-element and parton-shower calculations, Eur. Phys. J. C **76** (2016) 590, arXiv: 1606.08753 [hep-ph] (cit. on p. 27).

[157] ATLAS Collaboration,
Studies on top-quark Monte Carlo modelling with Sherpa and MG5_aMC@NLO, ATL-PHYS-PUB-2017-007, 2017, URL: https://cds.cern.ch/record/2261938 (cit. on p. 28).

[158] M. Bähr et al., *Herwig++ physics and manual*, Eur. Phys. J. C **58** (2008) 639, arXiv: 0803.0883 [hep-ph] (cit. on p. 28).

[159] J. Bellm et al., *Herwig 7.0/Herwig++ 3.0 release note*, Eur. Phys. J. C **76** (2016) 196, arXiv: 1512.01178 [hep-ph] (cit. on p. 28).

[160] L. Harland-Lang, A. Martin, P. Motylinski and R. Thorne,
Parton distributions in the LHC era: MMHT 2014 PDFs, Eur. Phys. J. C **75** (2015) 204, arXiv: 1412.3989 [hep-ph] (cit. on p. 28).

[161] S. Dulat et al.,
New parton distribution functions from a global analysis of quantum chromodynamics, Phys. Rev. D **93** (2016) 033006, arXiv: 1506.07443 [hep-ph] (cit. on p. 28).

[162] J. Bendavid et al.,
Les Houches 2017: Physics at TeV Colliders Standard Model Working Group Report, 2018, arXiv: 1803.07977 [hep-ph] (cit. on p. 28).

[163] I. W. Stewart and F. J. Tackmann, *Theory uncertainties for Higgs and other searches using jet bins*, Phys. Rev. D **85** (2012) 034011, arXiv: 1107.2117 [hep-ph] (cit. on p. 28).

[164] S. Gangal and F. J. Tackmann,
Next-to-leading-order uncertainties in Higgs+2 jets from gluon fusion, Phys. Rev. D **87** (2013) 093008, arXiv: 1302.5437 [hep-ph] (cit. on p. 28).

[165] R. Frederix and S. Frixione, *Merging meets matching in MC@NLO*, JHEP **12** (2012) 061, arXiv: 1209.6215 [hep-ph] (cit. on p. 29).